ON-CHIP QUANTUM AND NONLINEAR OPTICS: FROM SQUEEZING TO SPECTROSCOPY

A Dissertation

Presented to the Faculty of the Graduate School

of Cornell University

in Partial Fulfillment of the Requirements for the Degree of

Doctor of Philosophy

by

Avik Dutt

August 2017

ON-CHIP QUANTUM AND NONLINEAR OPTICS: FROM SQUEEZING TO SPECTROSCOPY

Avik Dutt, Ph.D.

Cornell University 2017

Quantum and nonlinear optics has garnered a lot of interest in the last few decades due to its applications in a plethora of fields such as sensing, spectroscopy, frequency metrology and quantum information processing. Optical microresonators have compactified the realization of several nonlinear phenomena since their inception, besides enabling fundamentally new paradigms in light-matter interaction. Planar microcavities such as ring resonators are particularly interesting for their ease of fabrication in a massively parallel fashion and their small mode volumes. Additionally, advances in fabrication techniques have enabled ultra-low losses and ultra-high quality factors in these planar CMOS compatible materials such as silica and silicon nitride.

In this dissertation, we harness the ultra-low loss of silicon nitride microrings along with its high third-order Kerr nonlinearity for two applications previously unexplored in this platform: bright squeezed light generation and dual comb spectroscopy. We begin by examining the background in each of these fields before detailing our approach to realizing a compact, robust and scalable alternative to the existing state-of-the-art.

The first part of this dissertation investigates squeezed light, a quantum state of light that is promising for quantum enhanced sensing and quantum computation or communication in the continuous variable regime. Nearly all previous chip-based sources of squeezing have been rather large (of the order of many wavelengths

in height and width), and work based on the second-order nonlinearity, which is found only in restrictive crystals lacking inversion symmetry. Here we report the first realization of squeezing using an integrated parametric oscillator above threshold based on the ubiquitous third-order nonlinearity. The on-chip microrings enable the generation of broadband continuous wave squeezing in contrast to the narrowband squeezing produced by their macroscopic counterparts, and this broad bandwidth is essential for high-bit-rate quantum communications. Furthermore, we show continuous electrical tuning of the degree of squeezing using integrated platinum microheaters incorporated above coupled microring resonators. We conclude our exploration of quantum photonics in silicon nitride with a path towards deterministic entanglement generation.

In the second part of this dissertation, we look into a classical application of the same platform: dual comb spectroscopy (DCS). This technique builds upon an actively pursued aspect of silicon nitride rings – that of frequency comb generation. Again, using the third-order Kerr nonlinearity, a series of narrow, equidistant lines can be generated in the frequency domain, to form a spectrum that is called a frequency comb. Two such combs with slightly different line spacings can be used for dual comb spectroscopy, which is an emerging technique for fast acquisition of broadband optical spectra. Since DCS does not involve any moving mechanical parts that are used in conventional spectrometers, it is much more robust. We generate, for the first time, two frequency combs on the same chip using a single laser, and use it for broadband spectroscopy of dichloromethane. We demonstrate simultaneous soliton modelocking of both combs and observe long mutual coherence times of 100 µs. Our results pave the way for an on-chip, fully integrated dual comb spectrometer.

BIOGRAPHICAL SKETCH

Avik was born in Kolkata (then Calcutta), West Bengal, India to his parents Mita and Rabindra Lall Dutt on that particular date in autumn when day and night are of equal length. Being the youngest of his generation, he was brought up in his ancestral home by his brothers, two uncles, one aunt and his grandmother, in addition to his parents. After completing his school education in St. Joseph's College, Bowbazar, Avik went to pursue his Bachelor of Technology in the Indian Institute of Technology, Kharagpur, majoring in Electronics and Electrical Communication Engineering, which is admittedly a rather long name for a department. The choice of this department was despite his natural disposition towards physics, which he did end up securing a minor in, during his undergraduate years. During his school and college years, he got the chance to explore several activities other than academics, including playing cricket with his brothers, and partaking in debates, elocutions, trivia competitions and music events with his friends. Perhaps the biggest influence his middle and high school had was on his writing style, much of which is apparent in this dissertation. He also managed to luckily land with Prof. Sayan Kar from the physics department, who guided Avik through his first ever research project – on quantum tunneling through smooth double barriers. For his undergraduate thesis, Avik moved towards a more applied field, albeit still numerical: he worked on capillary optical fibers for attaining large mode areas and for designing tunable couplers, working with Prof. Shailendra Varshney. He oscillated between pursuing condensed matter physics or researching gravitational waves for graduate school. However, a short tryst with photonic crystals during the summer he spent in Prof. Povinelli's lab in USC sealed the deal. He decided to continue in the field of optics, working towards his Ph.D. in the nanophotonics group of Prof. Michal Lipson at Cornell University. During the sabbatical year

that Prof. Paulo Nussenzveig spent in this nanophotonics group, Avik shifted from his initial project on spectroscopic biosensing using optofluidics to one on quantum optics in silicon nitride. The project came full circle when, several years later, the nonlinear properties of this material generated a light source which he used for spectroscopy, although in a radically different form than what was envisaged in the initial spectroscopy project. Having meandered his way through quantum and nonlinear optics in silicon nitride chips, Avik is looking forward to exploring topological photonics and dynamic nanophotonic structures for his postdoctoral research at Stanford.

Dedicated to my family, for their unconditional trust, love and support.

तमसो मा ज्तोतिर्गमय ॥

("From darkness to light")

ACKNOWLEDGEMENTS

This dissertation would not be complete without expressing my gratitude to a large number of supervisors, peers, colleagues, friends and family members that have been essential in my pursuit of the Ph.D.

First and foremost, I would like to thank my advisor, Prof. Michal Lipson. Her scientific insights, immense encouragement, and breadth of ideas have made working with her an enjoyable experience. Every time an experiment did not work, her constant words of encouragement have inspired me to go further. She has been a mentor in the professional and personal spheres, and I thank her for that. Michal, along with other members of the committee, emphasized the need for an intuitive explanation behind the results of extended mathematical calculations very early in graduate school. I am amazed by Michal's ability to stay on top of emails and work at all hours, and her availability to hold meetings in person or Skype in the midst of her frequent travels. The group she has built at Cornell, which continues to Columbia, has been instrumental in the successful completion of research goals, and has been a family away from home.

Prof. Paulo Nussenzveig has been more of my advisor at times than Michal herself on the quantum optics project, and I am deeply indebted to him for his constant guidance. We started the quantum optics experiment in 2012, and that year which Paulo spent at Cornell was one of great learning. I am glad we continued to work closely even after his move back to Brazil. The ability to discuss every aspect of the work in great detail is something that I will surely miss. Conversations with him often ran well into the night, thanks to the difference in time zones between Brazil and New York. He also introduced me to his group at Saõ Paulo, specifically Prof. Marcelo Martinelli, Prof. Alessandro Villar and Renato Domenguetti, who have have helped me with several aspects of the quantum optics

experiment, especially with respect to free space cavities. I enjoyed working with Renato during his year-long stint at Cornell, and I look forward to him and others in Saõ Paulo advancing the quantum optics projects on chip.

The work on nonlinear optics wouldn't have been possible without the guidance of Prof. Alex Gaeta and his group, and I express my gratitude to him for that. His intuition as well as rigor, that I learnt from his nonlinear optics course and through the many discussions we have had, has been a guiding light during the work leading to this dissertation. Prof. Farhan Rana has been a great member of the committee, and has provided me with a different perspective about my work and the way to approach a PhD in general. I enjoyed learning from his courses, especially the one on quantum optics, which was well-timed for me to carry out my research in the field. I would like to thank him for the depth in which he taught us during the course. Dr. Nathalie Picqué provided very helpful insight into dual combs, whether it be the technical details or the broader overview of various spectroscopy configurations. Prof. Reuven Ophir's discussions with us on cosmology, quantum optics and thermal emission has been very intellectually stimulating.

A large number of colleagues and friends, both in Michal's group, as well as outside, have provided the constant support that is needed to get through the many hours of failure that research inevitably demands, ultimately culminating in success when every aspect of the experiment starts to behave in harmony. Starting with Dr. Jacob Levy, who laid the foundation for the silicon nitride platform, I must thank Dr. Kevin Luke, Dr. Steven Miller and William (Xingchen) Ji for their tireless efforts in perfecting the nitride chips to achieve ever-increasing Q's and later endowing them with microheaters. Dr. Sasikanth Manipatruni and Dr. Vivek Venkataraman performed initial experiments towards detecting squeezed light ge-

nerated in nitride in the late 2000s. In this regard, I would like to acknowledge them for the ideas and discussions towards the beginning of my experiments. Dr. Alessandro Farsi, Dr. Sven Ramelow, Aseema Mohanty, Dr. Felippse Barbosa, Dr. Stephane Clemmen and Chaitali Joshi have been fellow companions on quantum optics discussions and I have learnt a great deal in the process. Most of the members of the group, including me, are indebted to Dr. Lucas Gabrielli's gdspy package which enabled us to design our devices seamlessly. On a broader note, I am grateful to the developers of python and its packages (numpy, matplotlib and scipy) - they have made programming and analyzing data very rewarding. Credit is also due to the developers of LaTeX, Zotero, Matlab, Comsol and Fimmwave.

Among the senior researchers in our group who had a lasting impact on my professional development through these years, I am especially indebted to Jaime, Carl and Mohammad. Dr. Jaime Cardenas was a mentor from day one, as we started out as neighbors in the office. In return for his valuable fabrication knowledge and his expertise about all things in integrated photonics, I could only offer him a little help in LaTeX, quantum physics and simulations. His transparency and approachability despite his multiple projects are things that I have missed when he moved to Rochester as a professor. Thanks to him and Cecilia for always informing us of meteor showers and other astronomical events, and for hosting amazing taco-fiestas at their home. Dr. Carl Poitras greatly helped me in getting started in the group and on the experiments. He was someone we could go and ask for general advice on experiments on any project. Carl also helped a lot during my time as a teaching assistant for Michals integrated optics cource. Dr. Mohammad Soltani was another neighbor in the office with whom I had long and deep discussions on science. His rigor and insight, especially on nonlinear silicon photonics, is inspiring. I am glad that we have kept in touch regularly even after he joined

BBN. He has provided me with valuable career advice and pointers every time we have met since. Dr. Mian Zhang has also been extremely forthcoming with advice about academia, and it was a pleasure learning optomechanics from your elegant explanations. Mohammad Soltani was probably the most experienced of the late night gang in the office, and other members of that gang such as Shreyas, Aseema, Kevin, Steve, Chris and Felippe also made it a pleasure to work late at nights in the lab. I am glad that this culture is continuing with the more recent members such as Lin, Gaurang, Euijae and Ipshita. Among those who worked during the saner hours, thanks are due to Moshe Zadka for taking care of the servers; to Brian Stern for making posters filled with puns; to Dr. Mohammad Amin Tadayon for advice on navigating visas; to Romy Fain for advice on machining; to Dr. Austin Griffith for teaching me the meaning of "bailiwick" and for imitating Sean Connery; and to Brian Lee, Dr. Raphael St-Gelais and Dr. Biwajeet Guha in general.

Since late nights have been such an integral part of grad school, I would like to individually thank everyone who was a part of that experience. Dr. Shreyas Shah warmly welcomed me into the lab on day one with an espresso shot, and it was great learning the more physics-y and mathematical side of nonlinear coupled equations from you. Chris was a walking encyclopedia whom we could refer to whenever we needed to fact check anything under the sun. Chris and I started as comrades in the biosensing/optofluidics area in our first year, and have since then moved on to very different projects. Steve's straightforward nature and trumpet-playing skills only add to his formidable perseverance in work – something that I have found very inspiring throughout the years. We went from buddies sharing the Velocity laser in the early days to friends sharing long conversations on dating and tech startups in recent times. Kevin was usually present after midnight, whether to discuss science, fabrication and CAD, or to discuss Bhangra, philosophy and personal life,

along with Aseema, Steve, Chris, and of course, the pseudo-Lipson-lab members – Ved and Suren. Kevin had a very different perspective from the majority of peers we meet in grad school. It is exciting to see him exploring the world with his globe-trotting, soul-searching trips post Ph.D – a bold, commendable step in itself. Aseema and Kevin have been especially great in providing personal advice, and I am grateful to them for painstakingly listening through long and detailed stories in this regard. I hope I have been patient enough to listen to your (sometimes long) stories too! With Aseema, I have had my most interesting conversations in the office, on topics ranging from the very mundane to the most controversial. I will definitely miss the never ending chats with her about academia and research, and Euijae has been a very informed addition to these chats in the recent past due to his tortuous multi-university career path. If the choice of colors in the figures of my papers have improved over the years, it is due to Aseema's suggestions. She was kind enough to laugh at every (non) funny and punny joke that I cracked, much to the dismay of others. In this context, I am glad that Gaurang is continuing the legacy of puns in our lab. It has been great to work with him on the thermal project, which has involved many stimulating discussions, which have often digressed to life and philosophy. Gaurang's calm composure is contrasted by Ipshita's never-ending arguments with him – something that has kept us entertained in the office along with William's one-line quips. Ipshita has introduced me to some of the crazier ideas being explored in our group, with graphene or wilder materials.

Among the newer members at Columbia, I've enjoyed these last two years in NYC in the company of Dr. Samantha Roberts, Dr. Utsav Dave, Dr. You-chia Chang, Euijae Shim, Oscar Jimenez and Dr. Tong Lin. I am immensely pleased that Lin and Utsav have taken over my setup, and I can't wait to see them do amazing experiments on nonlinear optics and frequency combs in the near future.

Talking about nonlinear optics, Dr. Yoshi Okawachi's treasure of knowledge on frequency combs has been a blessing, along with Dr. Kasturi Saha, Mengjie Yu, Chaitanya Joshi, Dr. Alexander Klenner and Dr. Jae Jang.

Nathan Ellis deserves a special mention for teaching me the art of machining in great depth and rigor. He is the manager of the Clark hall machine shop at Cornell, and he always had constructive suggestions for the designs I discussed with him, especially about the optical cavity construction. The ten-week course he led was not only very useful, but also very enjoyable - it made machining during and after the course a fun experience. I'd also like to thank Scott Coldren, Kim Cotton and Krystal Paulino, without whose administrative support, we would not have been able to meander our way through the many procedures of academic research.

I am lucky to have found the most amazing set of friends in grad school. In particular, I'd like to start with the names of my roommates Pranav Gupta, Aurosish Mishra, and Amit Bhatia, and some of my Cornell friends Ved Gund, Aniket Kakatkar, Shreyas Honrao, Rohil Bhatnagar, Payal Seth, Pankaj Singh and Anuja Bagul. Ved and Aniket's frequent trips to New York ensured that we ventured into the city to Fat Cat, instead of just spending our weekends near Columbia. With Aniket, Rohil, Payal and Chaitanya I've enjoyed several music concerts and events in NYC over the years. Rohil has been extremely welcoming and hosted me every time I have visited Ithaca after moving to NYC. His likings are similar to mine in many aspects, which has led to an ever increasing friendship with him. He, along with Payal and Pankaj have kept me up-to-date with the happenings in Ithaca.

Ritika Dusad was a close friend and a special physics buddy through a significant part of the journey. She was a strong support, especially during the long winter breaks in Cornell when very few souls would remain in Ithaca. She also provided me with valuable feedback on my manuscripts and thesis proposal slides.

I look forward to seeing her do very interesting work in the exciting field of low temperature physics that she have chosen.

Returning closer to the lab, I have incidentally made several very good friends in Prof. Gaeta's group, including Dr. Prathamesh Donvalkar, Chaitali Joshi, Gauri Patwardhan and Chaitanya Joshi. With Pratham, I have enjoyed exchanging professional and personal discussions, be it about rubidium, frequency combs or finance and Wall Street. I always learnt something new about modern world history from the Saturday morning brunches with you. Your persistence and discipline are qualities that I admire. Along with Pratham, I should also mention Kadambari Chheda for her garrulous nature and fun ideas. Chaitali Joshi has been a great friend – there is hardly any topic under the sun that we havent talked about – be it politics, economics, the environment, quantum optics or about Scott Aaronson's latest blog post. I would like to use this space to reiterate that, contrary to your conviction, experimental physics papers are not nearly as opaque as you think they are compared to computer science papers (!) Gauri has been the best of friends through two major personal crises that struck me in the last two years - I possibly cannot thank her enough for her support and understanding through those critical times. During the same period, she has introduced me to new experiences. Her hypothetical questions and "sensible" one-liners are second to none. It has been a pleasure to get the chance to work with Gauri on her more recent simulations. Chaitanya is another friend with whom I have collaborated quite a bit in our recent projects, but our friendship goes far beyond the lab. In fact, we have known each other from the beginning of grad school, and at this point we have enough mutual information to never miss a chance to throw a gibe at each other. His blunt remarks and sarcasm only make the conversation more fun, especially since we have at times very differing opinions about academia. I hope I get to frequently

see all of you even after moving far from the east coast.

Last, and perhaps the most, I would like to thank my family for being there for these long years. The geographical distance between them and me has become more bearable because of the long phone calls and chats that we have shared through the duration of my PhD. My parents have always emphasized the importance of prioritizing academics above everything else at each stage of my career, something that was essential to furthering my studies to this stage. Their constant good wishes and guidance are a major part of the reason why I have reached where I am today.

PREFACE

On December 29, 1959, Richard Feynman gave a lecture, "There's plenty of room at the bottom," to an audience at Caltech. He talked about the direct manipulation of matter at the nanometer scale - specifically, about the possibility of manipulating individual atoms. This inspired the field of nanotechnology decades later, although its direct influence on catalyzing the birth of the field is a subject of debate.

On June 1, 1982, Feynman published an article titled "Simulating physics with computers" in the International Journal of Theoretical Physics, where he looked into the possibility of exactly mapping quantum physics problems onto a computing machine. This laid down the foundations of a universal quantum computer.

Today, progress in technology has brought us to a juncture where we can think of combining these two fields - nanotechnology and quantum computing, using the field of nanophotonics, i.e., the science of manipulating light-matter interaction at the nanoscale. This dissertation is an endeavor to take steps towards realizing the grand goal of nanophotonic quantum computing. In the journey towards this grand goal, we realize several intermediate milestones (e.g. squeezed light generation) as well as practical applications (e.g. dual-comb spectroscopy).

TABLE OF CONTENTS

LIST OF TABLES

LIST OF PUBLICATIONS DURING PH.D.

1. A. Dutt, C. Joshi, X. Ji, J. Cardenas, Y. Okawachi, K. Luke, A. L. Gaeta, M. Lipson, "On-chip dual comb source for spectroscopy," (in review) arXiv:1611.07673 (2016).

2. A. Mohanty, M. Zhang, A. Dutt, S. Ramelow, P. Nussenzveig, M. Lipson, "Quantum Interference between Transverse Spatial Waveguide Modes", **Nat. Comm. 8, 14010 (2017).**

3. X. Ji, F. A. Barbosa, S. P. Roberts, A. Dutt, J. Cardenas, Y. Okawachi, A. Bryant, A. L. Gaeta, M. Lipson, "Ultra-low-loss on-chip resonators with sub-milliwatt parametric oscillation threshold," **Optica** 4, 619 (2017).

4. A. Dutt, S. Miller, K. Luke, J. Cardenas, A. L. Gaeta, P. Nussenzveig, M. Lipson, "Tunable squeezing using coupled ring resonators on a silicon nitride chip", **Opt. Lett.** 41, 223 (2016).

5. S. A. Miller, Y. Okawachi, S. Ramelow, K. Luke, A. Dutt, A. Farsi, A. L. Gaeta, M. Lipson, "Tunable frequency combs based on dual microring resonators," **Opt. Express** 23, 21527 (2015).

6. J. Cardenas, M. Yu, Y. Okawachi, C. B. Poitras, R. K. W. Lau, A. Dutt, A. L. Gaeta, M. Lipson, "Optical nonlinearities in high confinement SiC waveguides", **Opt. Lett.** 40, 4138 (2015).

7. A. Dutt, K. Luke, S. Manipatruni, A. L. Gaeta, P. Nussenzveig, M. Lipson, "On-chip Optical Squeezing", **Phys. Rev. Applied** 3, 044005 (2015).

8. K. Luke, A. Dutt, C. B. Poitras, M. Lipson, "Overcoming Si_3N_4 film stress limitations for high quality factor ring resonators", **Optics Express** 21, 22829 (2013).

CHAPTER 1

INTRODUCTION

Optics, the science of light, has become an all-pervading aspect of our everyday lives. It spans areas as fundamental as the study of the furthest galaxies in the universe, to aspects as trite as home and street lighting, television, supermarket checkouts and medical clinics. The invention of the laser by Theodore Maiman in 1960 was a paradigm shift that not only allowed for a better understanding of light-matter interactions, but also ushered in unprecedented new technologies such as long-distance optical fiber communications and laser-written compact disks.

The desire for more compact optical devices over the last two decades has mirrored the progress of electronics, pushing the frontiers of optics to smaller and smaller scales. Novel phenomena appear when light is confined to compact geometries, enhancing its interaction with matter. This had led to the birth of the field of photonics, or the modern science of light. Optical fibers, the backbone of the telecommunications industry, guide light in very small cross sections ($\sim$ tens of microns) over large distances with low loss. These fibers are made of silicon dioxide, or silica glass. Using alternative materials such as silicon and silicon nitride, light can be confined to even smaller geometries, on the order of microns to hundreds of nanometers – and the study of light at these scales has come to be known as nanophotonics.

In this dissertation, we will explore several applications of the novel paradigms offered by nanophotonics in the areas of quantum and nonlinear optics. Quantum optics involves the study of the behavior of light departing from its classical aspects, allowing us to enter regimes which would not be possible with classical light. This enables applications such as quantum-enhanced sensing, quantum si-

mulation and quantum computing. Nonlinear optics relates to the study of light at high intensities, where different wavelengths (i.e. colors) of light, usually noninteracting at low intensities, start mixing with each other to produce new wavelengths. While considered a menace for optical fiber communications, nonlinear optics can be harnessed in a beneficial manner for spectroscopy, metrology, and frequency conversion of light.

The majority of research in quantum and nonlinear optics has been the preserve of bulky tabletop setups. Here we integrate these fields into millimeter-sized chips using micron-scale waveguides and resonators. This enables a compact, scalable and robust platform for exploring phenomena such as squeezed light generation and on-chip entanglement. We use the same platform for producing light spanning a broad optical spectrum, called a frequency comb, with hundreds of frequencies all within a single beam. This comb is used for fast, real-time spectroscopy of dichloromethane, an organic solvent.

1.1 Central themes of the dissertation

In this section, we introduce the various themes central to our work. These themes are explained in detail in the next chapter.

1.1.1 Nanophotonics on a silicon chip

Nanophotonics is the manipulation of light at the nanometer scale, in analogy with microelectronics and nanoelectronics. Nanophotonics has found widespread use in optical communications, sensing, optomechanics, spectroscopy and biological

applications such as neurophotonics and optogenetics. Of particular interest is silicon photonics [1, 2], which leverages the massive infrastructure and mature fabrication technology of electronics to enable devices that can guide, route and manipulate light. The choice of materials is directed by its compatibility with complemenatary metal-oxide-semiconductor (CMOS) technology, the mainstay of electronics. Silicon (Si), silicon nitride (Si_3N_4) and silicon dioxide (SiO_2) are very commonly used CMOS-compatible materials in the semiconductor electronics industry. For the entirety of this dissertation, we will use silicon nitride waveguides covered by a silicon dioxide cladding. These waveguides can confine light to the micrometer scale, leading to high intensities. Improved fabrication techniques in silicon nitride allow us to achieve ultra low loss and consequently propagate light for long distances without it diminishing in intensity significantly. The combination of high intensities with long propagation lengths enables efficient nonlinear optics studies in this platform.

1.1.2 Nonlinear optics

Nonlinear optics concerns itself with the behavior of light at high intensities, where the response of the material medium through which light propagates is not linear. In the frequency domain, the wavelengths of light at the output of the medium can be different from those at the input due to the material nonlinearity. Since light is composed of very weakly interacting bosons, called photons, nonlinear effects become important only at high intensities, which corresponds to either high powers or very tightly confined geometries. In this dissertation, we take the latter route to explore nonlinear optics at moderate powers in on-chip photonic structures. Specifically, we show how a multitude of new frequencies can be generated, all

phase-coherent with each other, using nanophotonic waveguides and resonators. These frequencies are used for spectroscopy. When operated at low powers, where only a few new frequencies are produced, we investigate quantum correlations between the generated light beams. Nonlinear optics is fundamental to the study of the quantum properties of light.

1.1.3 Quantum optics

Quantum optics is the study of the effects produced by the granularity of light, i.e. the fact that a beam of light is made up of discrete particles photons, with wave and particle properties. Interestingly, a very large class of phenomena in optics can be described by considering the light field to be a classical wave, and quantizing exclusively the behavior of electrons. This includes the phenomena of laser oscillation and thermal emission. Quantum properties of light become important typically when the nonlinear interaction between one or more light beams produces correlations beyond what is expected classically. For example, a laser beam sent through a nonlinear medium produces pairs of photons that are perfectly correlated in intensity, well beyond the classical limit of the input laser. Extended to higher powers of the input laser beam, and combined with properly designed resonators, these correlations can manifest themselves in the form of "twin beam" squeezing - where the macroscopic intensities of the beams are correlated in a statistical sense. We will study in detail the generation of such squeezed beams in this dissertation. Squeezed light is intimately related to quantum entanglement – an aspect that Schrödinger called the very essence of quantum mechanics, after Einstein, Podolsky and Rosen pointed out the *spooky action-at-a-distance* ("spukhafte Fernwirkung") that entanglement entails.

1.1.4 Quantum information processing (QIP)

Quantum technologies have moved from the domain of textbooks to real-world applications in the last few decades. Quantum key distribution is perhaps the most well-developed application of quantum information till date. A host of platforms have been explored for QIP, including trapped ions, photons, nuclear spins, quantum dots, superconducting qubits, defect centers in diamond and other materials, and topological quantum states (See Nature Physics insight [3] and the articles therein [4–9]). While the jury is still out on the best platform for QIP, superconducting qubits and photonics are among the best suited in terms of simplicity and scalability. Besides, any quantum technology that operates over long distances will almost inevitably use optics as a low loss and low-decoherence carrier to transmit information. Quantum information processing encompasses the fields of quantum computing, quantum communications and quantum simulations, whose individual goals are distinct but closely related. In contrast to classical computing where bits can take values of 0 or 1, information in QIP is encoded in quantum bits or "qubits" which can exist in a superposition of states $\alpha|0\rangle + \beta|1\rangle$. More importantly, nonclassical correlations can exist between distinct qubits, which allows certain algorithms to show an exponential speedup over their classical counterparts, as shown by Shor in the case of prime factoring [10, 11]. In fact, prime factoring and quantum key distribution [12, 13] protocols have provided arguably the greatest impetus to the development of QIP technologies.

Quantum optics offers a versatile platform for implementing quantum information processing (QIP) [14]. Due to the low loss with which light can be guided over very long distances ($\sim$ hundreds of kilometers over fibers), the electromagnetic field of a light beam can be used to encode information, both in the continuous

degrees of freedom such as the amplitude and phase, as well as in the discrete degrees of freedom such as polarization or photon number. These two regimes are respectively referred to as the continuous variable (CV) and discrete-variable realizations of optical QIP.

Any information processing system consists of sources/transmitters, circuits and detectors/receivers. While detectors and photonic circuits to route light are sufficiently advanced for optical QIP, sources of quantum light are often probabilistic and fragile, making deterministic QIP a herculean task. Similarly, since photons are weakly interacting, making gates to control light in analogy with the transistors of electronics is extremely challenging. Operating at moderately high powers in the CV regime, as opposed to the very low powers used in discrete variable QIP, is one approach to solve this problem. Squeezed states are an essential resource for CV QIP, which will be studied at length in this dissertation. Cluster states, an especially useful multimode counterpart of squeezed states, offer a promising realization of a universal quantum computer.

1.2 Outline of the dissertation

Chapter 2 discusses the tools essential in our study of integrated quantum and nonlinear optics: microresonators. We start with a basic introduction to waveguides, high quality factor resonators, four-wave mixing, parametric oscillation and discuss the coupling setup in some detail. We also talk about the primary method used to tune resonances of microcavities: integrated microheaters. The devices used in this dissertation were designed and characterized by me, while their fabrication was handled by my colleagues Kevin Luke, Steven Miller and Xingchen

Ji.

Chapter 3 reports the first generation of squeezed light using an integrated FWM parametric oscillator. We elucidate the theoretical foundations, previous work and the applications of squeezed light, before delving into the details of our approach to produce broadband two-mode intensity-difference squeezing. This is also the first room-temperature source of squeezing using a CMOS compatible material. Chapter 4 extends these results to develop a method for tuning the degree of squeezing. Integrated microheaters applied to a coupled microresonator system are the keys elements for this realization of tunable squeezing. These chapters study the behavior of the FWM parametric oscillator just above the threshold of oscillation.

Chapter 5 discusses experiments further above threshold to go beyond two-mode squeezing, to investigate multimode correlations in parametric oscillators. Additionally, we explain the construction of a narrowband filter cavity to mitigate excess noise in the input laser which has deleterious effects on squeezing measurements. We also develop analysis cavities to enable phase-sensitive detection of the correlations between generated light beams, and show a path towards achieving continuous variable entanglement.

In chapter 6, we demonstrate, for the first time, the generation of two distinct frequency combs on the same chip from a single laser, to form what is called a dual comb spectrometer. This is a shift towards studying the classical dynamics of the parametric oscillators, in contrast to the nonclassical paradigms of the previous chapters. We show low-noise mode-locked operation of both combs, and study the formation of soliton states within the microresonators. We also perform real-time broadband absorption spectroscopy of dichloromethane (CH_2Cl_2) using the dual

combs over timescales as short as 20 µs.

Chapter 7 concludes with a discussion of the many possible research avenues one could take to build upon work presented here. The appendices contain details about device fabrication, analysis cavities, and a comparison of material platforms for nonlinear and quantum photonics.

CHAPTER 2

TOOLS OF THE TRADE: NONLINEAR MICRORESONATORS

This chapter provides an in-depth introduction to the silicon nitride microcavities that form the basis for the rest of the dissertation. We will talk about Maxwell's equations, nonlinear optics, four-wave mixing and parametric oscillation.

2.1 Maxwell's equations and nonlinear optics

Light is a time-varying electromagnetic field with wavelengths in the hundreds of nanometers to microns range. Like all electromagnetic fields, the behavior of light with electric field $\vec{E}$ and magnetic field $\vec{H}$ is governed by Maxwell's equations:

$$\vec{\nabla}.\vec{D} = \rho \tag{2.1}$$

$$\vec{\nabla}.\vec{B} = 0 \tag{2.2}$$

$$\vec{\nabla} \times \vec{E} = -\frac{\partial \vec{B}}{\partial t} \tag{2.3}$$

$$\vec{\nabla} \times \vec{H} = \vec{J} + \frac{\partial \vec{D}}{\partial t}, \tag{2.4}$$

along with the constitutive relations for the electric and magnetic flux densities $\vec{D}$ and $\vec{B}$ respectively,

$$\vec{D} = \epsilon_0 \vec{E} + \vec{P} \tag{2.5}$$

$$\vec{B} = \mu_0 \vec{H}. \tag{2.6}$$

where $\epsilon_0 = 8.85 \times 10^{-12}$ F/m and $\mu_0 = 4\pi \times 10^{-7}$ H/m are the electric permittivity and magnetic permeability of free space respectively. We have neglected the magnetic polarization as we will exclusively deal with nonmagnetic materials. Additionally, for a dielectric material at optical frequencies, there are no free charges and currents, hence the charge density $\rho = 0$ and the current density $\vec{J} = 0$.

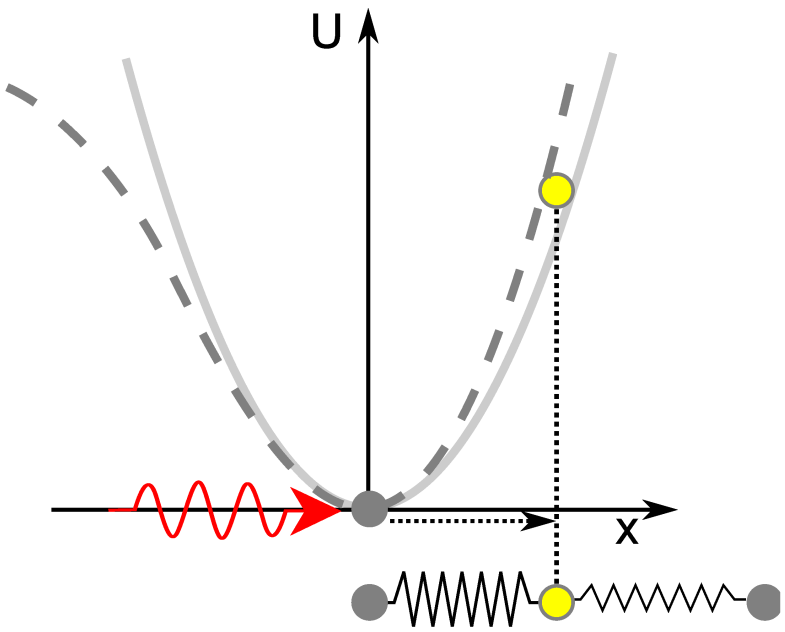

Figure 2.1: Potential U experienced by a bound electron in a dielectric. Near equilibrium, the potential can be represented by a quadratic function (solid line) and the response to an electric field is linear. Away from equilibrium (dashed line), the potential deviates to produce a nonlinear response. Image from [15]. The current figure shows a non-centrosymmetric potential. For silicon nitride and most other materials, the potential is symmetric about the origin, albeit nonlinear.

On taking the curl of Eqs. 2.3, combining it with 2.4 and 2.5 using vector identities and the relation $\mu_0\epsilon_0 = 1/c^2$, we arrive at Maxwell's wave equation,

$$\nabla^2\vec{E} = \frac{1}{c^2}\frac{\partial^2\vec{E}}{\partial t^2} + \frac{1}{\epsilon_0 c^2}\frac{\partial^2\vec{P}}{\partial t^2} \tag{2.7}$$

The wave equation for a linear, isotropic and homogeneous medium admits plane wave solutions of the form

$$E(\vec{r},t) = E_0 e^{i(\vec{k}.\vec{r}-\omega t)} \tag{2.8}$$

with wave vector $\vec{k}$ and angular frequency ω.

The polarization field $\vec{P}$ at the microscopic scale is determined by the response of the electrons in a material to an externally applied electric field. The bound

electrons can be approximated to be moving in the potential of the much heavier fixed nuclei. Near the equilibrium position, the potential experienced by the electron is quadratic, and the electrons feel a linear restoring force when excited by an external electric field [2.1 solid line]. For large displacements, the potential deviates from the quadratic function and the response becomes nonlinear. This happens when the driving electric field is comparable to the atomic field that holds the electron to the nucleus ($E_{\text{at}} \sim e/4\pi\epsilon_0 a_0^2 = 5 \times 10^{11}$ V/m, where a_0 is the Bohr radius).

In general, the polarization can be expanded as a Taylor series in the electric field as,

$$\vec{P} = \epsilon_0 \left[\underline{\chi^{(1)}} \vec{E} + \underline{\chi^{(2)}} \vec{E}\vec{E} + \dots \right] \tag{2.9}$$

where $\underline{\chi}$'s are tensors of appropriate rank for the susceptibility. More commonly, this equation is written in the component form (assuming Einstein summation for repeated indices):

$$P_i = \epsilon_0 \left[\chi^{(1)}_{ij} E_j + \chi^{(2)}_{ijk} E_j E_k + \dots \right] \tag{2.10}$$

Here i, j, k label any of the x, y, z components of the field.

The first term in the expansion for $\vec{P}$ is the linear response of the system, which represents small oscillations of the electrons about the mean position. The second term corresponds to the second-order nonlinearity, which is found only in restricted crystal structures lacking inversion symmetry. This lowest order nonlinearity is absent in most substances. This brings us to the next term, the third-order nonlinearity, also called the Kerr nonlinearity. Explicitly writing out the frequency domain expression for this term [16], we arrive at:

$$P_i^{(3),\text{NL}}(\omega_\sigma) = \sum_{mnp} \epsilon_0 \, \chi^{(3)}_{ijkl}(\omega_\sigma; \omega_m, \omega_n, \omega_p) E_j(\omega_m) E_k(\omega_n) E_l(\omega_p) \tag{2.11}$$

where $\omega_\sigma = \omega_m + \omega_n + \omega_p$.

The third-order nonlinearity is ubiquitous, in that it is found in all materials. Even vacuum is nonlinear above the Schwinger limit ($E > 10^{18}$ V/m). In the language of quantum electrodynamics, the four-photon vertex for the Feynman diagram of photon-photon scattering is very weak in vacuum. The presence of a material increases the strength of this effective four-photon vertex mediated by the electrons in the material. For the purposes of this dissertation, we will limit ourselves to *parametric* nonlinear processes, i.e. where the optical energy is conserved. Examples of non-parametric nonlinear processes include Raman and Brillouin scattering, and multiphoton absorption, where energy is lost to the phononic degrees of freedom of the material.

In Eq. 2.11, the frequencies ω's could be negative, using the convention $E(-\omega) = E^*(\omega)$ for real electric fields in the time domain. With this convention, Eq. 2.11 can represent a wide variety of nonlinear phenomena. Some examples of parametric processes based on the third order nonlinearity include,

- Third harmonic generation. ($\omega_\sigma = 3\omega_m; \omega_m = \omega_n = \omega_p$).
- The intensity dependent refractive index and self-phase modulation (SPM). ($\omega_\sigma = \omega_m = \omega_n = -\omega_p$).
- Cross-phase modulation (XPM) ($\omega_\sigma = \omega_m \neq \omega_n = -\omega_p$).
- Four-wave mixing (FWM), when at least three different frequencies are involved. ($\omega_\sigma \neq \omega_m, \omega_n, \omega_p$).

The work described in this dissertation uses FWM, along with the effects of XPM and SPM. Note that these three processes can occur between optical fre-

quencies that are close to each other, as opposed to third-harmonic generation, or any frequency mixing process mediated by the second-order nonlinearity.

Any nonlinear process occuring in dielectrics has to satisfy two stringent requirements to be efficient:

1. The fields should have a high intensity, because optical nonlinearities in dielectric materials are weak.
2. The fields should be phase-matched (momentum conservation). Energy conservation is enforced by the parametricity of the processes being studied here.

As we will see in the following sections, the first point is addressed in our work by using high-confinement waveguides that increase the intensity by facilitating a small effective area [Sec. 2.2.2]. Furthermore, high-quality factor microcavities are used for resonant enhancement of the field intensity [Sec. 2.2.3]. The second point is addressed by careful design of the waveguide geometry [Sec. 2.2.2].

2.1.1 Four-wave mixing (FWM)

Four-wave mixing is a third-order parametric nonlinear process whereby light fields at three frequencies (or wavelengths) interact to produce a new light beam at a fourth wavelength (called the idler). If two of the frequencies are identical, the process is termed as degenerate FWM. Typically, a weak signal beam (ω_s) interacts with one or two strong pump beams (ω_p) to produce light at the idler frequency ω_i. The signal beam gets amplified in this process, which is termed as parametric amplification.

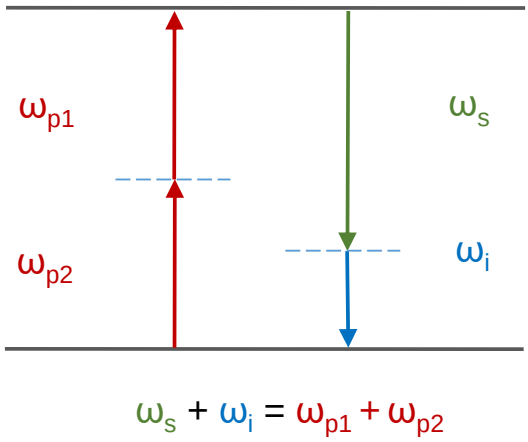

Figure 2.2: Energy level diagram for four-wave mixing (FWM) between two pumps (p1 and p2), signal (s) and idler (i) frequencies. For the degenerate case, $\omega_{\mathrm{p1}} = \omega_{\mathrm{p2}}$.

In the quantum description of four-wave mixing, two pump photons are annihilated to produce a signal photon and an idler photon in pairs, in an energy conserving process [Fig. 2.2]. We will see in Chapter 3 that this simultaneous production of photon pairs in an energy conserving interaction is at the heart of the generation of quantum-correlated twin beams and the consequent two-mode squeezing.

The coupled amplitude equations for four-wave mixing can be derived from Eq. 2.7 and 2.11, by substituting a slowly varying envelope similar to 2.8 for each of the signal, idler and pump frequencies. Under the strong undepleted pump

approximation, the coupled amplitude equations take the form [17–21],

$$\frac{dE_p}{dz} = -\frac{\alpha_p}{2}E_p + i\gamma|E_p|^2E_p \tag{2.12}$$

$$\frac{dE_s}{dz} = -\frac{\alpha_s}{2}E_s + 2i\gamma|E_p|^2E_s + i\gamma E_p^2E_i^*e^{-i\Delta\beta z} \tag{2.13}$$

$$\frac{dE_i}{dz} = -\frac{\alpha_i}{2}E_i + 2i\gamma|E_p|^2E_i + i\gamma E_p^2E_s^*e^{-i\Delta\beta z} \tag{2.14}$$

$$\tag{2.15}$$

where α's denote the linear power loss per unit length for the respective frequency, and $\gamma = \omega n_2/cA_{\text{eff}}$ is the nonlinear parameter, with $n_2 = 3\chi^{(3)}/8n_0$ the nonlinear index, and A_{eff} is the effective area to which the light beams are confined. The second terms in the last two equations represent XPM induced by the strong pump on the weak signal and idler beams. The final term mediates energy transfer between the pump and the signal and idler modes, and is responsible for parametric gain and amplification.

The efficiency of the power transfer is dependent on the linear phase-mismatch $\Delta\beta = 2\beta_p - \beta_s - \beta_i$, as well as the overall phase-matching factor κ including the effects of SPM and XPM. Here β represents the propagation constant of each frequency mode, which is the effective index multiplied by the free-space wave vector (more on this in section 2.2.2 on waveguides). Following the treatment in Agrawal and several other references [17–19], the total phase mismatch is obtained as,

$$\kappa = 2\gamma P_p - \Delta\beta \tag{2.16}$$

An essential point to be noted from this equation is that $\Delta\beta$ must be positive to compensate for the XPM and SPM induced nonlinear phase shifts. Expanding β around the pump wavelength using its first and second derivatives β_1 and β_2:

$$\beta(\omega) = \beta(\omega_p) + \beta_1(\omega_p)(\omega - \omega_p) + \frac{1}{2}\beta_2(\omega_p)(\omega - \omega_p)^2 + \ldots \tag{2.17}$$

and using the fact that the signal and idler are symmetric in frequency by energy conservation arguments ($\omega_s - \omega_p = \omega_p - \omega_i$), we can show that $\Delta\beta \approx -\beta_2 \ (\omega_s - \omega_p)^2$. In other words, for $\Delta\beta$ to be positive and the overall phase-mismatch κ to vanish, the second-order dispersion β_2 has to be negative (anomalous) at the pump wavelength.

The requirement for anomalous group velocity dispersion $\beta_2(\omega_p) < 0$ is among the most important requirements for efficient FWM gain and parametric oscillation, and serves as a guiding principle when designing the dimensions of the waveguides. Note that Si_3N_4 devices with normal dispersion have been used for the generation of FWM frequency combs, in some cases assisted by mode crossings between the transverse spatial or polarization modes of a waveguide to attain locally narrowband anomalous dispersion [22–28]. In Sec. 2.2.2, we will see how the requirement of anomalous dispersion is satisfied by engineering the geometry of the waveguide, to counter the normal dispersion of bulk silicon nitride.

For degenerate FWM, the parametric gain coefficient per unit length can be shown to be [17, 21, 29, 30]:

$$g = \sqrt{(\gamma P_p)^2 - \kappa^2/4} = \sqrt{\gamma P_p \, \Delta\beta - (\Delta\beta)^2/4} \tag{2.18}$$

The FWM gain is plotted for values of the nonlinear parameter γ typical for silicon nitride in Fig. 2.3. A few points are worth mentioning here: (i) The parametric gain coefficient increases with the pump power, (iii) Realistically large gain coefficients are achievable over a broad bandwidth, which exceed the typical propagation loss of silicon nitride waveguides (~ 10 dB per m or lower) (ii) One can see that the peak of the FWM gain curve shifts away from the pump wavelength for larger values of the pump power and for lower values of the anomalous dispersion. These design parameters are critical for broadband frequency comb generation

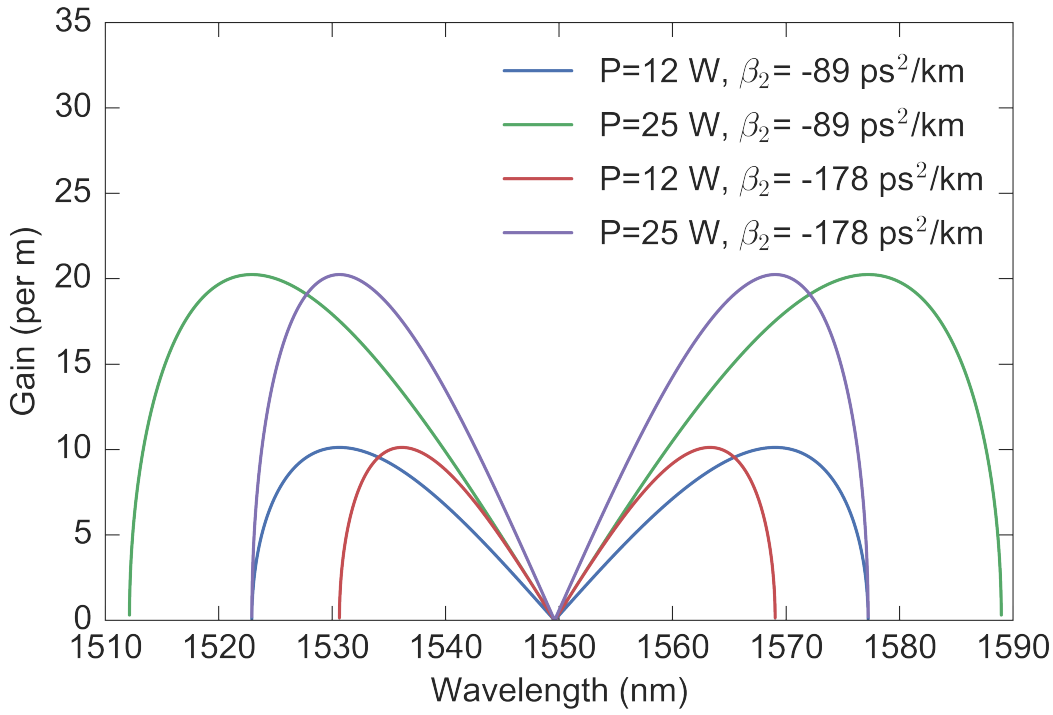

Figure 2.3: FWM gain and bandwidth for various pump powers (P) and dispersion coefficients (β_2) around the pump wavelength of 1550 nm, plotted using Eq. 2.18. The peak of the gain curve shifts away from the pump wavelength for higher values of pump power and for lower values of $|\beta_2|$. $\gamma = 1$ W^{-1} m^{-1}. Similarly, the range of wavelengths over which FWM gain persists increases with a decrease in $|\beta_2|$ and an increase in pump power P_p.

(Chapter 6) and for engineering the first oscillating mode in squeezing experiments (Chapter 3).

2.1.2 Optical parametric oscillation (OPO)

When the parametric gain coefficient exceeds the total loss in the medium, net amplification is observed. If a resonant feedback structure is build around the

parametric amplifier, optical parametric oscillation (OPO) can be attained, similar to the case of a laser cavity above threshold. However, in contrast to a laser, the oscillating beams possess manifestly quantum properties. Parametric oscillation was first observed by Giordmaine and Miller [31] in a lithium niobate crystal. Since the pioneering experiments of Wu *et al.* in the mid-1980s, OPOs have become indispensable for quantum optics [32–34].

For silicon nitride waveguides, a microring resonator provides an ideal way of implementing this feedback cavity, and also enhances the light intensity in the waveguide by two to three orders of magnitude. In the triply resonant case of parametric oscillation described here, a strong pump beam generates light at two new frequencies – the signal and idler frequencies – by amplifying vacuum fluctuations at these modes. Matsko *et al.* [35, 36] have calculated a threshold of oscillation that depends on the cavity mode volume V, the refractive index of the cavity medium n and the loaded Q_{L} and coupling Q_c quality factors according to the formula,

$$P_{\mathrm{th}} \approx 1.54 \frac{\pi}{2} \frac{Q_c}{2Q_{\mathrm{L}}} \frac{n^2 V}{n_2 \lambda_p Q_{\mathrm{L}}^2} \tag{2.19}$$

This expression assumes vanishing or very low anomalous dispersion, and equal quality factors for the three resonant modes participating in the oscillation. These are reasonably good approximations in the devices studied in our work. The higher the loaded quality factor of the cavities, the lower is the pump power needed for oscillation. A low pump power indicates a small frequency separation between the signal and pump modes, in accordance with Fig. 2.3.

2.2 Integrated photonics

Monolithically integrated optical devices use planar fabrication techniques to make rectangular waveguides and resonators for guiding light. Post-fabrication tuning of waveguide properties is achieved using thermal or electrical means. In this section, we introduce silicon nitride waveguides and resonators integrated with platinum microheaters for thermal tuning.

2.2.1 Silicon nitride for nonlinear photonics

Silicon nitride (Si_3N_4) is our material of choice for integrated photonics at telecommunications wavelengths (around 1550 nm) due to several factors.

First, it has a moderately high refractive index of 2, which makes it much better at guiding light than silica ($\sim n = 1.5$). The index is less than that of semiconductors such as silicon, germanium and III-V materials, but linear and nonlinear losses are much larger in these semiconductors. The effective area of modes in a Si_3N_4 waveguides is significantly smaller than that of optical fibers by 1-2 orders of magnitude, depending on the waveguide dimensions, which is again made possible by the higher index.

Second, Si_3N_4 has a broad transparency window that spans most of the visible and the entire near-infrared wavelength range ($\sim 0.4 - 3$ µm). This property is beneficial for broadband comb generation, spectroscopy and frequency agility.

Third, and very importantly, it is compatible with complementary metal-oxide-semiconductor (CMOS) technology, enabling massively parallel fabrication and economical production of devices leveraging the already existing infrastructure

of silicon-based microelectronics. Si_3N_4 is used as a diffusion barrier in CMOS fabrication lines, and as a passivation layer for microchips. Hence, it is an integral part of CMOS foundries. We use low-pressure chemical vapor deposition (LPCVD) techniques to grow films for the waveguiding layer.

Fourth, Si_3N_4 has not been reported to show Raman or Brillouin scattering, unlike silica and silicon. These processes are non-parametric, leading to deleterious effects on quantum noise measurements. In fact, guided acoustic wave Brillouin scattering (GAWBS) [37–40] and Raman noise [41–44] have limited the degree of squeezing observable in silica fibers. Indirect evidence has been reported of the effect of Raman frequency shifts on Si_3N_4 frequency combs [45, 46], but further studies are required to ascertain the presence or absence of Raman scattering in Si_3N_4 at telecommunication wavelengths.

Furthermore, for nonlinear photonics, silicon nitride waveguides are ideal due to the high nonlinear index of Si_3N_4 ($n_2 = 2 \times 10^{-19}$ m^2 W^{-1}), and due to the ability to tailor the dispersion of the waveguide mode by engineering the geometry of the waveguide. Its nonlinearity is about ten times lower than that of silicon and ten times higher than silicon dioxide.

All these reasons have made Si_3N_4 the dominant material for nonlinear photonics at telecommunication wavelengths. In fact, when the field of FWM-based Kerr frequency combs began 10 years ago in microresonators [47], several material platforms were explored [53, 54], as summarized quantitatively in the table in Appendix A, and illustrated in Fig. 2.4. Today, Si_3N_4 has been adopted by most research groups in favor of other material platforms (see recent work from the groups of Kippenberg [55–59], Weiner & Qi [23, 25, 60–62], Diddams [63], Wong [26, 64–66]. From an experimental standpoint, the ease of fabrication and

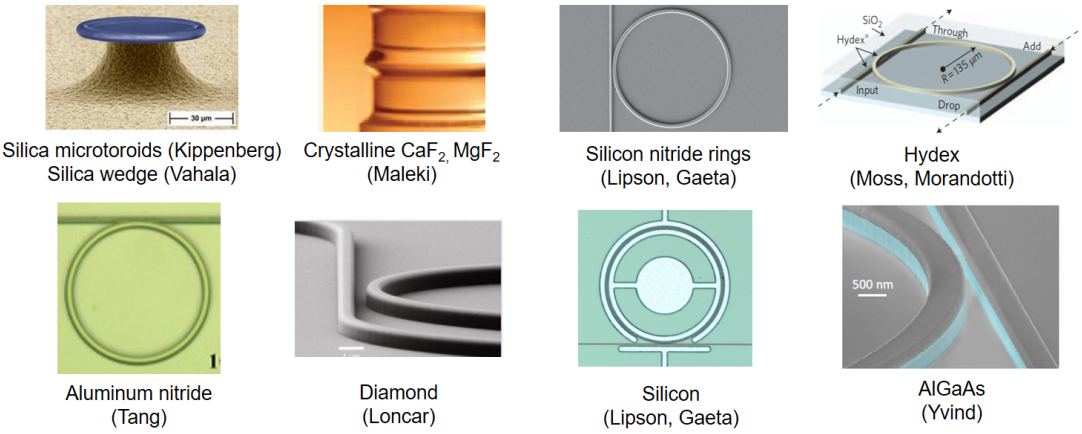

Figure 2.4: Microresonator platforms for nonlinear optics, especially with respect to frequency comb generation. All of these are planar and waveguide coupled, except for silica microtoroids and crystalline resonators. Images adapted from [36, 47–52]

the broad optical span that have been demonstrated are major drivers for Si_3N_4 nonlinear optics.

2.2.2 High-confinement waveguides

A waveguide consists of a central region called the core, made of a higher refractive index material, surrounded by a lower index cladding. We choose silicon nitride as the waveguide core material and silicon dioxide (or silica) as the cladding. Light is guided in the core region by total internal reflection at the core-cladding interface.

In the wave picture, one can write down Maxwell's wave equation 2.7 in the linear regime with the assumption that $\vec{P} = \epsilon_0 \chi^{(1)} \vec{E}$ and $\epsilon_r = 1 + \chi^{(1)} = n^2$,

$$\nabla^2 \vec{E}(\vec{r}, \omega) = \frac{n^2(\omega)\ \omega^2}{c^2} E(\vec{r}, \omega) \tag{2.20}$$

where we have used plane wave solutions as the ansatz. On imposing the boundary

conditions for the electric and magnetic fields into the above equation, discrete eigensolutions can be found for the fields, with eigenvalues for the effective index corresponding to different guided modes of the waveguide [67]. The propagation constant for the modes are defined by

$$\beta(\omega) = \omega\, n_{\text{eff}}(\omega)/c \tag{2.21}$$

The effective index of the fundamental mode is the highest. Successively higher order transverse modes have lower indices, approaching the cladding.

Silicon nitride waveguides confine light to small mode areas, of the order of a square micron or lower. The intensity of a light beam is related to the power (P) and effective area (A_{eff}) by the simple relation,

$$I = \frac{P}{A_{\text{eff}}} \tag{2.22}$$

where the effective modal area for a single mode of the FWM nonlinear interactions we will be dealing with is defined by [29],

$$A_{\text{eff}}^{-1} = \frac{\int |E|^4 dA}{\left(\int |E|^2 dA\right)^2} \tag{2.23}$$

While single mode waveguides are preferred for most linear applications to prevent intermodal crosstalk, nonlinear effects are often more efficient in multimode waveguides due to the dimensions dictated by phase-matching requirements. We use the commercial finite element modeling software, COMSOL Multiphysics, to numerically solve for the eigenmodes of a waveguide and find their effective indices. The refractive index for silicon nitride and for silicon dioxide as a function of wavelength are provided to the model in the form of Sellmeier equations. This allows us to incorporate material dispersion effects [68, 69].

$$n_{Si_3N_4}^2 = 1 + \frac{3.0249\,\lambda^2}{\lambda^2 - 135.3406^2} + \frac{40341\,\lambda^2}{\lambda^2 - 1239842^2} \tag{2.24}$$

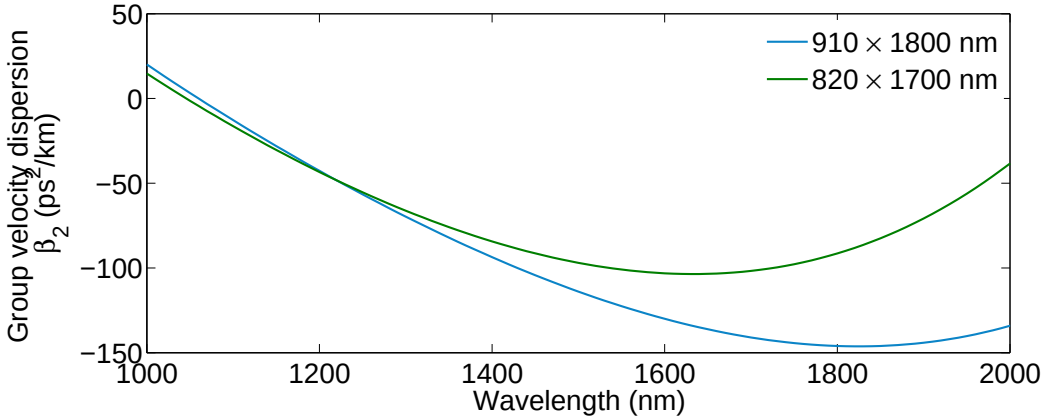

Figure 2.5: Group velocity dispersion vs. wavelength for two geometries, for the fundamental transverse-electric mode. Both dimensions show strong anomalous dispersion around the pump wavelength of 1550-1560 nm.

where λ is the wavelength in nanometers.

The waveguides used in this dissertation have widths around 1300 – 1500 nm and heights of either 730 nm or 950 nm. The 950 nm high waveguides have a higher anomalous group velocity dispersion (GVD) than the 730 nm waveguides, resulting in more narrowband comb generation. A representative plot of the GVD is shown in Fig. 2.5. We see that the dispersion is anomalous, despite the fact that the bulk dispersion of Si_3N_4 is strongly normal at these wavelengths. These dimensions correspond to high-confinement geometries [70, 71], since the electric field intensity is predominantly localized in the silicon nitride core. This is in contrast to weakly guiding systems such as optical fibers and thin photonic waveguides that have been previously demonstrated to achieve low loss [72–76].

2.2.3 High quality factor resonators

High-confinement waveguides localize light in the transverse direction to a small effective area and increase the intensity of the guided wave; however, for nonlinear optics, even higher intensities are needed. To achieve this, one can either localize light temporally using pulses, or in the longitudinal spatial direction using cavities. We choose the latter approach as it is more suited for generating frequency combs. The ultra-low losses achievable through improved fabrication techniques have pushed the frontiers in terms of the quality factor [71, 77, 78].

An optical cavity consists of a defined trajectory that light re-traces multiple times. Each single pass through the cavity is called a roundtrip. When an integer number of wavelengths that fits in one roundtrip of the cavity, constructive interference occurs and light gets resonantly enhanced within the cavity. Cavities can be implemented in various configurations. A few common ones include the standing wave Fabry-Perót cavities and photonic crystal cavities, and the traveling wave ring cavities made of three or more mirrors. Although these macroscopic cavities have been shown to have very high quality factors and finesse, their large mode volume limits the efficiency of nonlinear processes. Nevertheless, the first OPO was demonstrated in such a macroscopic cavity [31]. Moving to the microscopic realm, optical microcavities have been realized as whispering gallery mode configurations such as microtoroids [79], microspheres [80, 81] or crystalline rod resonators [48, 82, 83], in microdisks [84] and in waveguide-based geometries such as microrings.

A microring resonator comprises a waveguide bent and folded onto itself to form a closed circular optical path, and coupled to a bus waveguide [Fig. 2.6]. Constructive interference occurs when the phase acquired by the light in one roundtrip

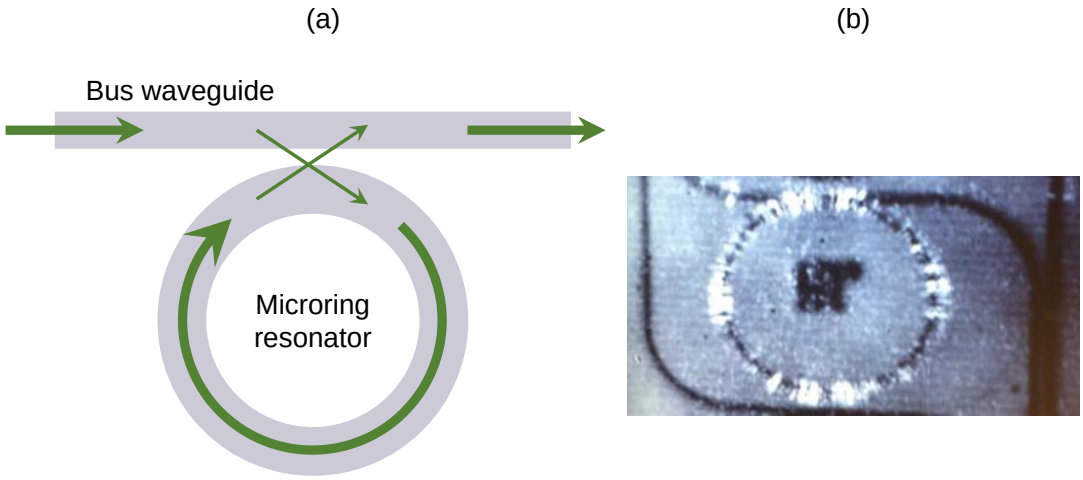

Figure 2.6: (a) A ring resonator coupled to a bus waveguide (b) An image captured by a CCD camera and an imaging column showing near-infrared light glowing in the microring.

around the circumference, $\beta \times L$, is an integral multipe of 2π:

$$\beta L = 2m\pi, \quad m \in \mathcal{Z} \tag{2.25}$$

For a circular ring resonator, $L = 2\pi r$, where r is the radius of the ring. To fit a ring within one field of the electron beam lithography tool, we sometimes use a non-circular geometry, (see Fig. 3.2). Since $\beta = \omega\, n_{\text{eff}}(\omega)/c = 2\pi\, n_{\text{eff}}/\lambda$, this is equivalent to the condition

$$L\, n_{\text{eff}} = m\lambda_m \tag{2.26}$$

i.e., the optical path length is an integral multiple of the wavelength. Resonance frequencies are related to the wavelength by $f_m = c/\lambda_m$. On resonance, the light transmitted through the bus waveguide shows a dip as the input light destructively interferes with the resonant light leaking through the coupling region out of the

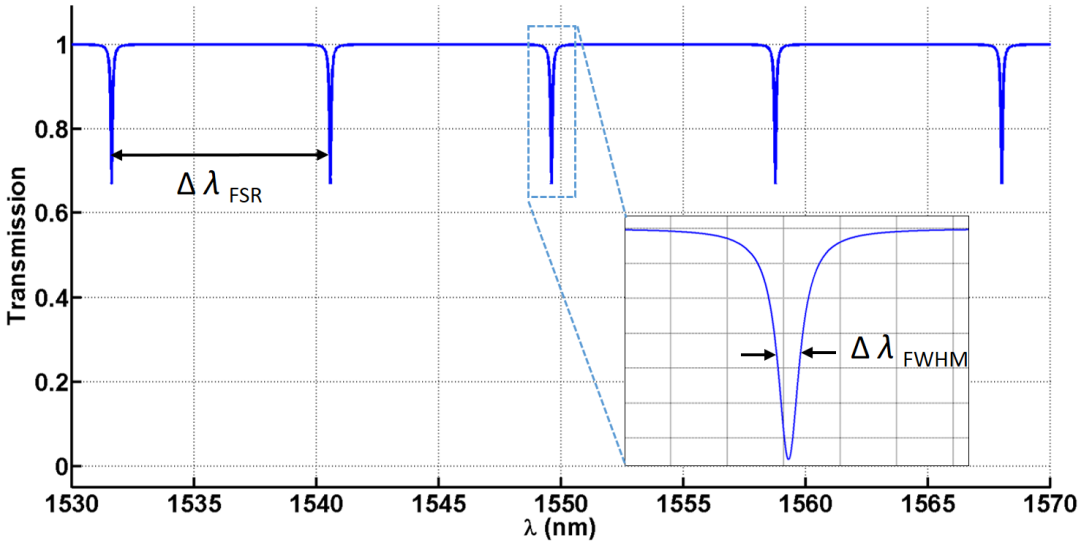

Figure 2.7: Simulated transmission spectrum of of a ring resonator. The zoom-in shows an expanded view of a single resonance. The free-spectral range (FSR) and the full-width at half maximum (FWHM) are marked. Parameters used correspond to a Si_3N_4 ring with a radius of 20 µm, a propagation loss of 2 dB/cm, an intrinsic Q $\approx 1.8 \times 10^5$ and a loaded Q of 1.7×10^4.

cavity, as can be seen in a typical simulated transmission spectrum shown in Fig. 2.7. The spacing between adjacent resonance frequencies belonging to longitudinal modes m and $m+1$ can be derived from this expression to be,

$$\Delta f_{\mathrm{FSR,m}} = \frac{c}{n_g(\lambda_m)L} \tag{2.27}$$

and is called the free-spectral range (FSR) of the resonator. Here $n_g = n_{\mathrm{eff}} - \lambda dn_{\mathrm{eff}}/d\lambda$ is the group index. The group index is related to the first order dispersion by the relation $\beta_1 = d\beta/d\omega = 1/v_g = n_g/c$. It represents the speed at which information is carried by a pulse, or in other words, the speed at which the envelope of a wave packet travels. In free space, light always travels at c, but in a waveguide made of a certain material, this speed is reduced, and the effective speed is dependent on the wavelength, captured by the group velocity v_g. The FSR

changes with wavelength (or frequency), and this change is related to the second order dispersion $\beta_2 = d^2\beta/d\omega^2$ through the following relation [35]:

$$\begin{aligned} \Delta^2 f_{\mathrm{FSR}} &= (f_{m+1} - f_m) - (f_m - f_{m-1}) && (2.28) \\ &= \Delta f_{\mathrm{FSR,m+1}} - f_{\mathrm{FSR,m+1}} && (2.29) \\ &\approx -\frac{2\pi\beta_2}{L^2\beta_1^3} && (2.30) \end{aligned}$$

A microresonator's quality factor is defined as the ratio of the energy stored in it on resonance $\mathcal{E}$ to the energy lost per cycle, normalized by the angular resonance frequency $\omega_m = 2\pi f_m$:

$$Q = \frac{\omega_m \mathcal{E}}{-d\mathcal{E}/dt} \tag{2.31}$$

When the quality factor is not too low (> 10), this expression can be put in a more experimentally accessible form:

$$Q = \frac{f_m}{\Delta f_{\mathrm{FWHM}}} = \frac{\lambda_m}{\Delta\lambda_{\mathrm{FWHM}}}. \tag{2.32}$$

Here Δf_{FWHM} and $\Delta\lambda_{\mathrm{FWHM}}$ refer to the full-width at half-maximum for the resonator in the frequency and wavelength axis. The quality factor defined above and measured in experiments is called the loaded Q, Q_L – it has all the loss mechanisms included, and is determined by the measured FWHM linewidth when the ring is "loaded" by waveguide coupled to it. For an isolated ring (when the waveguide is infinitely far away), the most common mechanisms of loss are scattering and absorption losses in the ring, which together contribute to the intrinsic quality factor Q_i. In a loaded ring, there is an additional portion of light that is lost through the coupling region, and this is called the coupling Q, Q_c. The various quality factors are related by the expression [21, 85, 86],

$$\frac{1}{Q_L} = \frac{1}{Q_i} + \frac{1}{Q_c}. \tag{2.33}$$

The coupled Q can be theoretically calculated or numerically simulated (in e.g. FIMMWAVE) and is exponentially related to the coupling gap between the ring and the bus waveguide. At critical coupling [85], the loss from coupling exactly matches the intrinsic losses within the ring, and we get perfection extinction of the transmitted light on resonance ($T_{\min} = 0$). If the coupling loss is higher (lower) than the intrinsic loss, the ring is said to be overcoupled (undercoupled), and the on-resonance (normalized) transmission minimum $T_{\min}$ is between 0 and 1. It can be shown that Q_c and Q_L are related to the minimum transmission by,

$$Q_c = \frac{2Q_L}{1 \pm \sqrt{T_{\min}}} \tag{2.34}$$

where the + and - signs corresponds to over- and under-coupled regimes respectively. From these expressions, one can calculate the escape efficiency, which tells us how much light is usefully extracted from the ring instead of being sacrificed to intrinsic losses within the ring:

$$\eta_c = \frac{Q_L}{Q_c} = \frac{1 \pm \sqrt{T_{\min}}}{2} \tag{2.35}$$

The escape efficiency η_c will be the limiting factor determining the theoretically achievable maximum squeezing level ($S_{\max} = 1 - \eta_c$) in Chapters 3 and 4. For a plot of the escape efficiency, see Fig. 4.6.

The intrinsic Q also provides us a very sensitive method of estimating propagation loss within the waveguide through the relation,

$$Q_i = \frac{2\pi n_g}{\lambda \alpha} \tag{2.36}$$

where α is the per unit propagation loss. During the early part of this dissertation work, the highest achievable intrinsic quality factors in Si_3N_4 were 7×10^6 [71] yielding a propagation loss of 4.2 dB/m. Improvements in fabrication techniques have recently increased Q_i to 3.7×10^7 in high-confinement ring resonators and $6.7 \times$

10^7 in wide-cross-section rings (10 µm), corresponding to ultra-low propagation losses of 0.8 dB/m [77].

2.2.4 Integrated microheaters

A major development during the course of this dissertation has been the incorporation of integrated platinum microheaters in the vicinity of the Si_3N_4 microrings, which enables us to tune the resonance wavelengths of the ring via the thermo-optic effect. Here we expand on the need for such tunability, and characterize the microheaters.

A mechanism of tuning the resonance frequencies of any cavity is desirable when the driving light beam does not have a tunable frequency. Non-tunable lasers, such as fiber lasers and planar-lightwave-circuit based lasers have narrower linewidths and lower noise that their tunable counterparts. Even if the laser is tunable, it is often convenient to have an extra control knob for aligning the frequencies of multiple independent microrings, as we will see in Chapters 4 and 6. In macroscopic cavities, tunability is typically achieved by attaching a piezoelectric transducer to one of the mirrors to change the length of the cavity (Chapter 5, Sec. 5.2).

In integrated microresonators, the possibility of physically changing the length of the cavity is not feasible. Fortunately, the thermo-optic effect dictates that the effective index of the resonator can be varied by changing its temperature, and from Eq. 2.26, this would change the resonance wavelength λ_m by affecting the *optical* path length. One can put the chip on a Peltier element connected to a current source or a thermoelectic controller (TEC) to change the temperature, but this is cumbersome and slow because the heating and cooling affects the entire chip

– the large heat capacity and long diffusion timescales of the heating mechanism restrict the precision of temperature control.

Microheaters, on the other hand, provide highly localized heat flow and reduced thermal cross-talk [87], enabling temperature control on the tens-of-microsecond timescales. Platinum is chosen as the material because it can withstand high temperatures without melting, and good quality of this metal can be sputtered on to the oxide cladding after the rings have been fabricated. It also provides satisfactory electrical contacts to the tungsten probe tips used to drive the heaters.

To minimize optical loss induced by the metallic platinum layer on the waveguide mode, a 2 µm SiO_2 cladding is used between the Si_3N_4 layer and the platinum layer. The heaters are about 100 nm thick and 3–6 µm wide. They have a resistance varying from 50–300 Ω. This enables significant power transfer to the heaters using modest voltage drives. For very small resonators, the heaters can be wound multiple times around the circumference of the ring to attain reasonable resistance values without reducing their width below what is reliably possible using contact photolithography [see Appendix B]. We apply voltages to the heaters through a DC supply or a Keithley source monitoring unit, depending on the precision required. Arbitrary waveform generators are also used for continuous dynamic tunability, as will be seen in Chapter 6.

The resonance frequency shift of the microrings is calibrated to be 1 –1.25 GHz per mW of electrical power applied to the heaters [Fig. 2.8]. For this measurement, we use a tunable laser and a DC power supply. We first note the frequency of the tunable laser when the ring is on resonance and no power is applied. Next, we apply increasing amounts of electrical power to the heaters and observe the change in the laser frequency needed to return to the same power. A linear fit provides

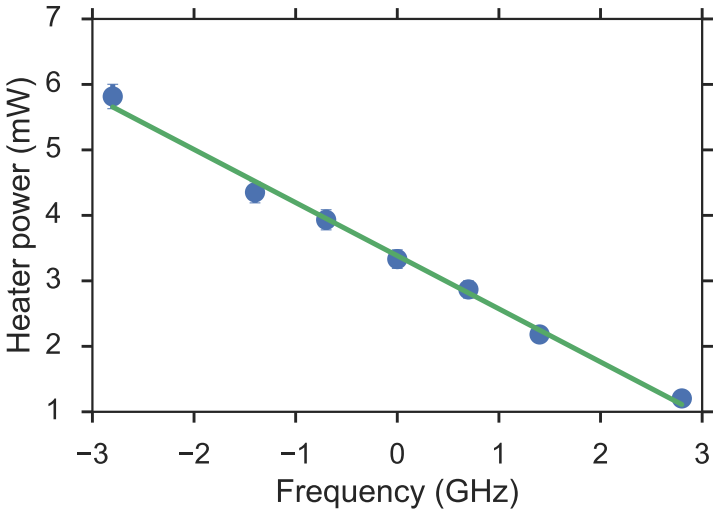

Figure 2.8: Calibration of the resonance frequency shift with heater power.

the required conversion between frequency and electrical power. A wavemeter (Advantest Q8326) with an accuracy of 0.1 pm is used to accurately verify the laser wavelength during this calibration. A subtle point to be noted here is that the heat changes the FSR of the rings and not directly the resonance positions. For large values of the longitudinal mode number m, a linear shift of the resonance frequencies with heater power turns out to be a good approximation. The slope of the curve is negative because both silicon dioxide and silicon nitride have a positive thermo-optic coefficient. Hence, an increase in heater power causes an increase in resonance wavelength [Eq. 2.26], which corresponds to a decrease in frequency.

Next, we measured the response time of the heaters by applying a 4 mV peak-to-peak square wave voltage and monitoring the transmitted power through the bus waveguide as shown in Fig. 2.9. We infer rise and fall times of 24 and 22 µs respectively from the exponential fits to the rising and falling edges of the transmitted optical power. The amplitude of the square wave voltage should be much smaller than the voltage required to tune across a ring resonance, to achieve

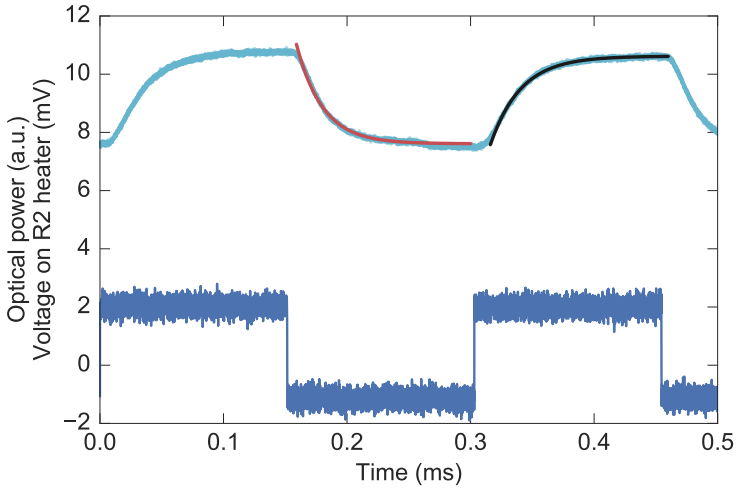

Figure 2.9: Measurement of heater response speed. A 4 mV peak-to-peak square wave modulation is applied to the heater on a microring at a low optical power. The DC offset of the applied voltage is tuned to bias the ring one side of the resonance. An exponential fit to the optical transmitted power provides a rise time of 24 µs and a fall time of 22 µs.

a linear transduction of the voltage to the transmitted optical power and mitigate the effects of the nonlinearity of the Lorentzian response on the exponential fit. For good signal-to-noise ratio, the ring is operated near the maximum slope of the Lorentzian response for these measurements of the heater speed. Additionally, the power coupled to the bus waveguide is kept low ($\sim$ 70 µW) to avoid thermal shift of the resonance. The 3 dB bandwidth of the heater response is 7 kHz, but the heaters can be operated at much higher speeds, albeit at lower tuning efficiency.

In later chapters we will see that the integrated microheaters are essential for dual frequency comb generation from a single pump laser, and for tuning the degree of squeezing in coupled microrings.

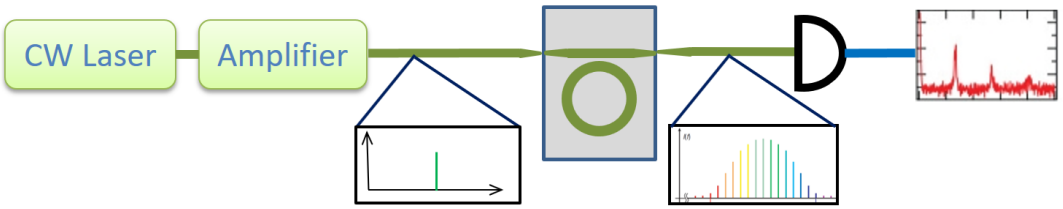

Figure 2.10: Schematic of a basic coupling setup for characterizing nonlinear microresonators. The description in the text is more exhaustive, and some components such as the polarization paddles, the polarizing filter, the imaging column and the translational stages have been omitted for clarity.

2.3 Basic experimental setup

Here we provide a brief overview of the basic components common to most experiments. We will describe detailed experimental setups as and when required in each of the following chapters.

The nonlinear microresonators are excited by continuous wave laser light around 1550 nm, after being amplified and filtered appropriately with an erbium doped fiber amplifier (EDFA) and a bandpass filter. This laser, which acts as the pump, is sent through polarization paddles and into a 2.5 µm-spot-size lensed fiber (OzOptics). For our experiments, we mounted the lensed fiber on a three-axis stage (Newport) with differential micrometers for coarse alignment to the on-chip waveguide. A three-axis piezoelectric actuator cube was also used for fine control of the position of the fiber. The chip is kept on a one-axis translational stage and a three-axis rotational mount. The output was collected with an aspheric lens (40×) to reduce collection losses, but a lensed fiber could also be used in principle. The characterization setup after the chip is highly dependent on the measurement to be performed. Required fractions of the output beam are sent to an optical

spectrum analyzer (OSA) and to a power meter to observe the onset of parametric oscillation and for alignment purposes, respectively. Only a small portion of the lensed fiber(s) should be freely hanging, to alleviate instabilities at high pump powers caused by cantilever motion of the fibers. A polarizing filter is used after the output lens to optimize to the transverse-electric mode for our experiments. Vertically above the chip, an imaging column mounted on a two-axis translational stage is also used. A 10× or 20× long working distance objective [Fig. 2.11], combined with a gooseneck fiber illumination from an incandescent lamp source, help to magnify the waveguides and microrings on the chip for alignment purposes. The imaging is preferably done with a Merlin/Indigo near-infrared CCD (charge coupled device) camera, and uses InGaAs pixels for detecting light. Alternately, a visible CMOS camera was also used in conjunction with a fiber coupled red laser beam for initial alignment. The fiber was switched to the 1550 nm band laser after visible alignment.

To isolate the coupling setup from air currents in the laboratory, a custom-shaped box made of acrylic was built. The entire setup was placed on floating optical tables to minimize the effect of mechanical vibrations affecting the experiments.

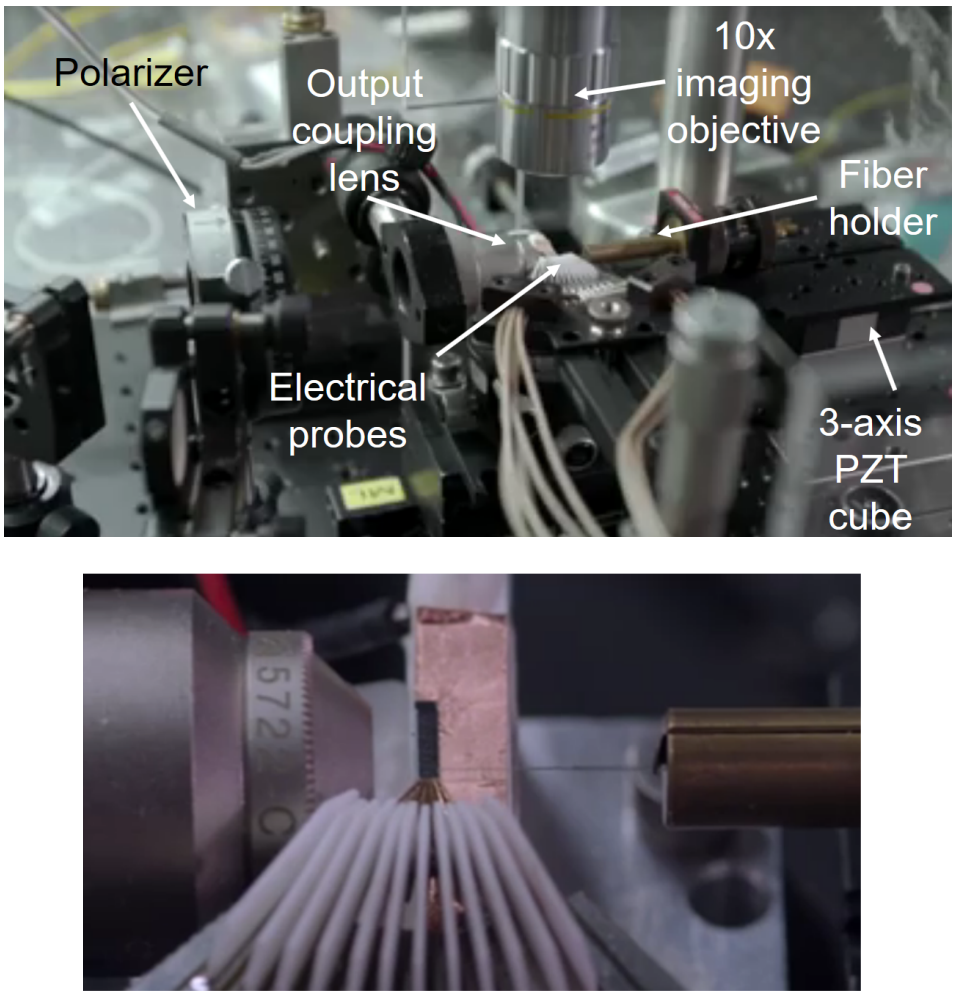

Figure 2.11: Image of the coupling setup showing the fiber holder, the electrical probes for microheaters, the output collection lens and the polarizer. The fiber, the probes and the chip are all mounted on translational stages, as is the objective for the imaging column. The bottom panel shows an expanded view of the chip (black) on copper tape, the input fiber, the collecting lens and the probes.

CHAPTER 3

ON-CHIP OPTICAL SQUEEZING

This chapter explores the generation of quantum states of light, specifically, squeezed light, using the nonlinear microresonators introduced in the previous chapter. Our aim is to develop a compact, robust and scalable source of broadband squeezed light integrated on a silicon-based chip. [1]

3.1 What are squeezed states?

A squeezed state is a state of light in which the electric field's noise at certain phases is reduced below the noise of the vacuum state, i.e. the noise when there is no light at all [89]. Although counterintuitive at first, squeezing is a direct manifestation of the quantum nature of light. In this section, we elucidate a simplified framework of squeezed light, and explain how nonlinearity is central to the generation of squeezed states.

A beam of light can be represented by its time-varying electromagnetic field. Even if we remove all classical or technical sources of noise that contribute to fluctuations in the field, this electromagnetic field still has noise due to quantum fluctuations, also called vacuum fluctuations or zero-point fluctuations. The minimum quantum noise allowed by Heisenberg's uncertainty relation is attained for the vacuum field, and for a special class of states called coherent states [90–92]. For example, the light emitted by a single mode low-noise laser far above threshold approximates a coherent state.

[1] Parts of this chapter have been published in *Physical Review Applied* [88]

Let us consider a field $E(z,t)$ with an angular frequency ω confined to a volume V, with quadrature amplitudes X and Y,

$$E(z,t) = \sqrt{\frac{2\hbar\omega}{\epsilon_0 V}}\left[X\cos(\omega t - kz) + Y\sin(\omega t - kz)\right] \tag{3.1}$$

Here X and Y could represent the amplitude quadrature and the phase quadrature respectively. Quadratures are a convenient representation of the slowly varying envelope of signals with a fast time-varying oscillation, and are commonly used in radio frequency communication systems. X and Y are referred to as the in-phase (cosine) and quadrature (sine) components of the signal with a fast oscillation at frequency ω. Whereas a field's positive frequency and negative frequency components can be complex valued, the quadratures in classical signals are always real-valued, and hence can be measured directly through, for example, heterodyne detection by mixing with a local oscillator.

When the field is quantized, the quadrature amplitudes X and Y become non-commuting operators. They are related to the field annihilation operator a by the relations:

$$X = a + a^\dagger, \quad Y = -i(a - a^\dagger) \tag{3.2}$$

with the commutator $[a, a^\dagger] = 1$ and consequently the following commutation relations for the quadrature operators:

$$[X, Y] = 2i \tag{3.3}$$

Again, the field operators a and $a^\dagger$ are not Hermitian, and cannot be measured as physical quantities, but the Hermitian operators corresponding to the quadrature amplitudes can be measured through homodyne and heterodyne detection. Defining $\Delta X = \sqrt{\langle (X - \langle X\rangle)^2\rangle}$, we directly arrive at the uncertainty relation for the root mean square fluctuations in two orthogonal quadratures,

$$\Delta X\ \Delta Y \geq \frac{1}{4}\left|[X, Y]\right|^2 = 1 \tag{3.4}$$

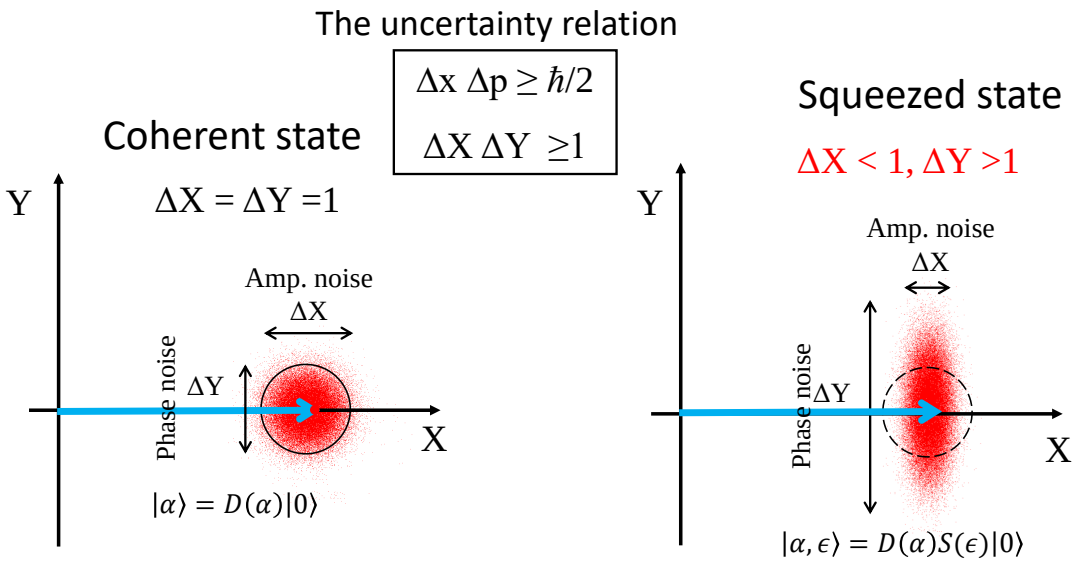

Figure 3.1: Coherent and squeezed states of the electromagnetic field. The blue phasors represent the mean value of the field. The red areas represent the noise ellipses around the mean value for coherent states (on left) and squeezed states (on right).

We can depict this minimum uncertainty product in the form of a noise ellipse as shown in Fig. 3.1. The blue arrows in the figure indicate the mean value of the field. The red noise ellipses represent the fluctuations about the mean value arising due to quantum noise. The area of the noise ellipse, which is equivalent to the product of the rms fluctuations in the X and Y quadratures, cannot be reduced below that dictated by the uncertainty relation. For coherent states of light [91], the fluctuations in all quadratures are equal and the noise ellipse takes the form of a circle (left panel of Fig. 3.1). The fluctuations in a coherent state define what is called the *shot noise level*. The shot noise level will be an important calibration for the experiments described in this work, as it sets the lower bound on the minimum fundamental noise level achievable classically, independent of the source. Noise

levels below the shot noise level for a particular optical power indicate quantum noise reduction and squeezing.

While the area of the noise ellipse cannot be reduced, one can reduce the fluctuations in one quadrature, say, the amplitude quadrature, X, at the expense of increasing the fluctuations in the orthogonal phase quadrature, Y. Such a state of light is called a squeezed state of light. A brief accessible review and introduction to squeezed light can be found in Ref. [89].

An alternative semiclassical way to understand the shot noise level, and the difference between coherent and squeezed states of light, is to imagine the light beam as a stream of propagating photons. For a coherent state or a laserlike beam, the time of arrival of successive photons is completely uncorrelated because the photons are noninteracting bosons. As is typical in such a discrete memoryless system, the distribution of photon number in a given time window follows Poisson statistics, i.e. the variance of the photon number is equal to the mean photon number. Thus, the fluctuations in the amplitude (which are related to the photon number variance) originate from the randomness in the time of arrival of photons. Squeezing involves a redistribution of the photon number distribution such that an amplitude squeezed state would have a more orderly arrangement of the time of arrival of photons than a coherent state. This introduces correlations between the photons which turn out to be quantum mechanical correlations. Since amplitude and phase quadratures are conjugate observables, a reduction in the amplitude noise is concomitant with an increase in the noise of the phase quadrature, and vice-versa. Later we will see that squeezing is intimately related to an essential feature of quantum mechanics, entanglement.

On a more mathematical note, following the treatment in Refs. [93] and [89], we

can define a coherent state with a mean photon number $|\alpha|^2$ using the displacement operator $D(\alpha)$ applied to the vacuum state:

$$|\alpha\rangle = D(\alpha)|0\rangle = \exp(\alpha a^\dagger - \alpha^* a)|0\rangle \tag{3.5}$$

where a is the annihilation operator for the mode of the electromagnetic field. By contrast, a squeezed coherent state can be defined using the squeezing operator $S(\epsilon)$ applied on the vacuum state:

$$S(\epsilon) = \exp(\epsilon\, a^2 - \epsilon^* a^{\dagger 2}) \tag{3.6}$$

$$|\alpha, \epsilon\rangle = D(\alpha)S(\epsilon)|0\rangle \tag{3.7}$$

A special case of this general squeezed coherent state is the squeezed vacuum, for which $\alpha = 0$.

A comprehensive experiment illustrating squeezed vacuum and light squeezed in different quadratures was reported by Breitenbach, Schiller and Mlynek [94].

Till now, we have been dealing with a *single mode* of the electromagnetic field. The kind of state defined by Eq. 3.7 are therefore called *single-mode squeezed states*. Squeezing, or quantum noise reduction, can also occur between two distinct modes of the field, e.g. two orthogonal polarization or frequency modes, labeled by corresponding annihilation operators a and b. In such a case, the *two-mode squeezing* operator can be defined as [89]:

$$S_2(\xi) = \exp(\xi\, ab - \xi^* a^\dagger b^\dagger) \tag{3.8}$$

Such states are not necessarily squeezed in their individual quadratures (e.g. X_a and X_b), but exhibit squeezing in a sum or difference of quadratures (e.g. $X_a - X_b$).

Both Eq. 3.7 and 3.8 directly show that the squeezing operator involves the product of fields in the exponential. Linear evolution of light alone – such as mixing two beams on a beam splitter, propagation through a material or polarization rotation – does not produce such products of the fields in the exponential. The squeezing operator is manifestly nonlinear in its exponent. One could consider the evolution of a field in the interaction picture, under the influence of a nonlinear Hamiltonian,

$$H_{\text{int}} = i\hbar\alpha(a^2 - a^{\dagger 2}) \tag{3.9}$$

and show that the unitary evolution operator $S = \exp(-iH_{\text{int}}t/\hbar)$ is of the same form as the single-mode squeezing operator in Eq. 3.7 if $\epsilon = \alpha t$ (where we have assumed α and ϵ to be real for simplicity, without loss of generality). A similar argument can leads to an interaction Hamiltonian for the two-mode squeezing case:

$$H_{2,\text{int}} = i\hbar\alpha'(ab - a^\dagger b^\dagger) \tag{3.10}$$

One can go even further and write down the equations of motion for the X and Y quadrature operators to show that they evolve under the influence of the Hamiltonian in Eq. 3.9 in the following manner [89]:

$$X(t) = S^\dagger X(0) S = X(0)\exp(-\alpha t) \tag{3.11}$$

$$Y(t) = S^\dagger Y(0) S = Y(0)\exp(\alpha t) \tag{3.12}$$

In other words, the X quadrature is deamplified and the Y quadrature is amplified. Which quadrature is amplified is determined by our choice of the phase of the complex number $\epsilon = \alpha t$. Here we chose a real ϵ, resulting in the X quadrature being deamplified. An important consequence is that, not only the field, but also its fluctuations are deamplified for the X quadrature as a result of evolution under the

squeezing operator. If we start with a coherent or vacuum state, the fluctuations in $X(0)$ correspond to zero-point fluctuations. In such a case, $X(t)$ has reduced fluctuations below the shot-noise limit, i.e. the time evolution converts a minimum uncertainty coherent state into a squeezed state.

Next, we seek physical realizations of the interaction Hamiltonians discussed above. It turns out that nearly all *parametric* nonlinear processes can result in some degree of squeezing, as long as the Hamiltonian is at least quadratic in the creation and annihilation operators. The parametricity of the process is important because non-parametric processes (such as Raman scattering, two-photon absorption, etc.) cause non-unitary evolution due to their non-energy conserving nature (in the optical domain), which leads to increased noise or losses. In fact, the simplest nonlinearity in optics, the second-order nonlinearity, possesses a Hamiltonian that is of the form that we are seeking:

$$H_{\mathrm{PDC}} = i\hbar\chi_{\mathrm{eff}}\ a_p a_s^\dagger a_i^\dagger\ -\ i\hbar\chi_{\mathrm{eff}}^*\ a_p^\dagger a_s a_i. \tag{3.13}$$

This represents the three-wave mixing process between the optical fields at the pump (p), signal (s) and idler (i) wavelengths, mediated by the second-order effective nonlinearity χ_{eff}. The frequencies of the three modes follow the energy conservation relation, $\omega_p = \omega_s + \omega_i$. The first term corresponds to parametric down conversion and the second term corresponds to sum-frequency generation. Since photons are weakly interacting, the material nonlinearities are low enough that nonlinear effects become significant only when one of the optical fields is strong, either through cavity enhancement or pulsed operation. For a strong pump, we can replace a_p by its complex-valued mean field A_p, and the Hamiltonian reduces to,

$$H_{\mathrm{PDC}} = i\hbar\ [\chi_{\mathrm{eff}} A_p\ a_s^\dagger a_i^\dagger\ -\chi_{\mathrm{eff}}^* A_p^*\ a_s a_i]. \tag{3.14}$$

We can see that the above Hamiltonian is identical to Eq. 3.9 or Eq. 3.10 for $\alpha = \chi_{\text{eff}} A_p$ depending on whether the signal and idler modes are degenerate (i.e. the same mode in all degrees of freedom) or non-degenerate (i.e. distinguishable in at least one degree of freedom).

Most solids, and all liquids and gases have a vanishing second-order nonlinearity because of inversion symmetry. A more ubiquitous nonlinearity in optics is the third-order nonlinearity, and the corresponding four-wave mixing Hamiltonian can be written as [95],

$$H_{\text{int}} = -\frac{1}{2}\hbar g_0 \sum_{x,y,z,w} \delta(x-y+z-w)\, a_w^\dagger a_y^\dagger a_x a_z \tag{3.15}$$

$$\tag{3.16}$$

The Kronecker delta enforces energy conservation. In the above equations, $g_0 = n_2 c\hbar\omega_{pump}^2 / n_0^2 V_{\text{eff}}$ quantifies the strength of the nonlinearity. The smaller the mode volume in which the field is confined, the higher this coefficient g_0. Restricting to the case of three fields again (degenerate pumping): pump (p), signal (s) and idler (i), with $\omega_s + \omega_i = 2\omega_p$, this Hamiltonian can be separated into self-phase modulation (SPM), cross-phase modulation (XPM) and four-wave mixing (FWM) terms.

$$H_{\text{int}} = H_{\text{SPM}} + H_{\text{XPM}} + H_{\text{FWM}}\,, \tag{3.17}$$

$$H_{\text{SPM}} = -\frac{1}{2}\hbar g_0 \sum_{x=p,s,i} \left(a_x^\dagger\right)^2 (a_x)^2 \tag{3.18}$$

$$H_{\text{XPM}} = -2\hbar g_0 \left[a_p^\dagger a_p a_s^\dagger a_s + a_p^\dagger a_p a_i^\dagger a_i + a_s^\dagger a_s a_i^\dagger a_i\right] \tag{3.19}$$

$$H_{\text{FWM}} = -\hbar g_0 \left[a_p^{\dagger 2} a_s a_i + a_p^2 a_s^\dagger a_i^\dagger\right] \tag{3.20}$$

Similar to the case of the second-order nonlinearity, the last term can produce two-mode squeezing (Eq. 3.10) when a strong pump $a_p \to A_p$ is used. The generation of two mode squeezing using FWM interactions is the focus of this chapter.

3.2 Background and state-of-the-art

3.2.1 Generation of squeezed states

The quantum nature of light was investigated in many contexts in the second half of the twentieth century, among them being the spontaneous emission from atoms and its inhibition [96, 97], photon antibunching in resonance fluorescence, and squeezed light generation [98]. Motivated by the arguments of Carlton Caves regarding the limits to interferometric phase detection for gravitational wave observatories [99, 100], theoretical predictions for ways to generate squeezed light abounded in the 1970s and early 1980s [101–110]. However, it was not until the seminal experiments of Slusher *et al.* in 1985 that the race to observe squeezing for the first time was concluded [111]. They used sodium vapor in an optical cavity to generate squeezed vacuum by the process of resonant FWM. Recent years have seen rubidium supplant sodium as the primary alkali atom vapor for squeezed light generation [112–116]. It is worthwhile to note that the typical experiments in these systems involve a pump laser and a probe beam at a different wavelength seeding the atomic vapor. Our work elaborated later uses a single laser beam to pump the nonlinear FWM microresonator.

Following closely on the heels of the first demonstration, parametric down conversion was shown to generate significant levels of squeezing in the spring of 1986, both below threshold [32, 33], and later, above [34] the oscillation threshold of parametric amplifiers. Indeed, parametric down conversion has become the workhorse for realizing strong squeezing for the past three decades [117]. Increasing squeezing levels of 6 dB [118], 7 dB [119, 120], 9 dB [121], 10 dB [122], 12.3 dB [123], 12.7 dB [124] were gradually reported. The current record for the highest

degree of detected squeezing is 15 dB [125] realized through improvements in the efficiency of detectors, homodyne visibility and low-loss optical setups. Second harmonic generation, the reverse of parametric down conversion, has also produced squeezed light, albeit limited in the degree of squeezing even in theory [108, 126–134].

A third way to generate squeezing has been through the third-order Kerr nonlinearity in optical fibers. Starting with the pioneering demonstration by Shelby *et al.* in 1986 [135] at liquid helium temperatures, various configurations have been investigated to generate squeezed light, mostly at room temperature. These configurations include (i) the use of pulses in fiber interferometers to achieve large nonlinear phase shifts and consequent single-mode squeezing [136–138], (ii) The use of seeded nondegenerate FWM in fibers to generate two-mode squeezing ("twin beam"-type correlations) [139], (iii) The use of polarization interferometers in a single fiber for squeezed light generation [140–142], (iv) The use of spectral filtering of solitons propagated through long fibers for photon-number squeezing [37, 143, 144]. Symmetric interferometers, i.e. those with a 50:50 beam splitter at the input/output coupling ports, generate quadrature squeezed light [136, 138], while asymmetric interferometers generate amplitude squeezed light or photon-number squeezed light [145, 146]. Guided acoustic-wave Brillouin scattering (GAWBS), which refers to the phase noise caused by the thermally-induced refractive index variations in the fiber, is a severe limitation to achieving high levels of squeezing using the Kerr nonlinearity. An excellent early review of quantum soliton pulses [37] in optical fibers can be found in [38]. Techniques have been developed to address GAWBS to increase the degree of detected squeezing in fibers [39, 40]. Raman scattering is also known to limit squeezing in fibers [41–44]. As we will see later, Raman and Brillouin scattering noise has not been reported explicitly in

the strongly pumped regime till date in silicon nitride waveguides or resonators, as opposed to silica or silicon, making silicon nitride an attractive platform for generating squeezed light.

Towards integrated sources of squeezed light

The experiments mentioned above were all restricted to table-top bulk optical cavities or fibers. The push to miniaturize quantum sources of light on a chip has led researchers to explore integrated options to generate nonclassical states. Early work in this direction involved lithium niobate ($LiNbO_3$) waveguides [147, 148] or potassium titanyl phosphate (KTP) waveguides [149, 150]. However, these waveguides have relatively large dimensions: $\sim> 5-10$ µm due to the low core-cladding index contrast, making their widths comparable to the core diameter of optical fibers. For compact photonic circuitry, narrower widths are desirable. Due to the low index contrast, they cannot be used to make compact ring cavities (which require tight bends) on chip, thus requiring high peak-power pulses and long lengths to generate squeezing. The first microresonator-based source of squeezed light was reported by Fürst *et al.*. They used a crystalline whispering-gallery mode disk resonator made of MgO doped $LiNbO_3$ to observe two-mode squeezing as well as single-mode intensity squeezing in parametric down conversion. The bandwidth of their squeezing was limited to 30 MHz due to the high loaded Q of the cavity. Additionally, $LiNbO_3$ and KTP waveguides are not CMOS compatible, making their integration with large scale, mature fabrication processes difficult. It should be noted that Safavi-Naeini *et al.* [151] have reported 0.2-dB squeezing of light using a silicon optomechanical resonator, which, although CMOS compatible and very interesting from a scientific perspective, is intrinsically restricted to a bandwidth of a few megahertz around the mechanical resonance and uses suspended structures

operating at low temperatures, making it less robust compared to sources based on all-optical nonlinearities.

Most previous integrated demonstrations have used the second-order nonlinearity. On the other hand, as early as in 1991 [152] and 1992 [153], the full analysis of nondegenerate FWM in cavities led to the prediction of two-mode squeezing between the signal and idler modes generated above threshold, akin to the case for the $\chi^{(2)}$ OPO [154]. In particular, the fluctuations in the intensity difference between the signal and idler fields was theoretically calculated to be squeezed below the shot-noise level, even when SPM and XPM were accounted for.

In our work we develop the first integrated FWM source of squeezing from an above threshold OPO, based on the third-order Kerr nonlinearity. We aim to produce *broadband* twin-beam squeezed light from an on-chip CMOS compatible silicon nitride ring resonator. Note that this is different from twin-beam squeezing based on seeded FWM such as in fibers or rubidium vapors

3.2.2 Applications of squeezed states

Squeezed light is useful for two major classes of applications. The first class relates to the use of the reduced noise in certain quadratures for beating the classical limit or the shot-noise limit in sensing, spectroscopy or imaging schemes [155]. The second class of applications relates to the use of squeezing - and its first cousin, entanglement - as a quantum resource for continuous variable quantum information processing [14, 156].

Quantum enhanced sensing and related technologies

Squeezing implies quantum noise reduction below the vacuum fluctuations - the shot-noise limit. A lower noise floor in certain phases or quadratures translates to a higher signal-to-noise ratio for the same absolute signal power. This in turn reduces the minimum detectable signal. A few years after the first experimental observation of squeezed light, proof-of-principle applications were demonstrated in sub-shot-noise spectroscopy [118, 157, 158]. Multimode squeezed light can surpass the standard quantum limit for imaging [159, 160]. In keeping with the initial motivation, squeezed light has now been incorporated into the LIGO and the GEO600 gravitational wave detectors [161–163]. Squeezes states are useful for the absolute calibration of photodiode quantum efficiency [125, 164] and for magnetometry [165, 166]. In the past few years, nonclassical light has made forays into biological sensing [160, 167, 168], into displacement sensing of cantilever motion [169] and into phase estimation [170]. Clock synchronization is another application of squeezed light that has been suggested by Giovanetti *et al.* [171].

Quantum information processing

Squeezing is an essential resource for quantum information processing (QIP) in the continuous variable (CV) regime [156]. In CV QIP, information is encoded in the amplitude and phase quadratures of the electromagnetic field, which are observables with a continuous range of values. This is in contrast to discrete variable QIP, where information is encoded in the form of quantum bits or qubits, using systems that can take one of two states, or a superposition thereof (such as polarization, spin, and so on.) The benefits of CV QIP are: (i) it is deterministic/unconditional as opposed to single-photon QIP which is probabilistic due to sources, (ii) CV quantum states can be produced at room temperature using standard nonlinear materials and modest laser powers, (iii) it can be detected at room

temperature using high quantum efficiency p-i-n photodiodes. On the other hand, single photon QIP is difficult due to the weak optical nonlinearity in most materials, which leads to a weak interaction of two single photons. The drawbacks of CV QIP are mainly the lack of well-developed error correction and fault tolerance algorithms, and the fragility of squeezed states to losses. Menicucci has presented a fault-tolerance threshold of 20 dB squeezing [172]. Better codes are expected to reduce this value to what is feasible with current technology ($\sim$ 15 dB). Deterministic entanglement [173–183] and unconditional quantum teleportation [184, 185] are enabled by mixing two squeezed states on a beam splitter. A long-term holy grail of the field is to realize a universal quantum computer in the CV regime. However, Gaussian states (such as squeezed and coherent states) combined with linear operations and quadratic nonlinearities are not enough to realize a universal quantum computer [186], and at least one non-Gaussian operation is required. The past decade has seen the rise of the one-way model of CV quantum computing, which works by performing measurements on an initial highly entangled multimode state called a "cluster state" [187, 188]. Experiments in the groups of A. Furusawa [189], C. Fabre and N. Treps [190, 191] and O. Pfister [192] have shown promising developments in this direction, bringing a universal quantum computer closer. These protocols could in principle be realized on a chip-scale using the platform we are introducing.

3.3 Silicon nitride microring OPO for squeezing: Design and methodology

Our approach to generate broadband squeezing utilizes silicon nitride microring resonators operated as a triply resonant optical parametric oscillator (OPO) above threshold. As explained in Chapter 2, Sections 2.1.1 and 2.1.2, this process of degenerate-pump FWM involves the annihilation of two pump photons to produce a signal photon and an idler photon simultaneously in pairs, as shown in Fig. 3.2.

Many efforts have been directed at the development of on-chip single-photon light sources using CMOS compatible materials such as silicon, silica and silicon nitride [193, 194] and other platforms [195, 196]; at the development of detectors [197], and logic gates [14]. The development of brighter nonclassical light sources, such as squeezed light sources [89], on CMOS-compatible platforms has been lagging behind.

Silicon suffers from two-photon absorption and free-carrier absorption at telecommunications wavelengths (1550 nm), which inhibits parametric oscillation [198] and induces additional loss channels, which are detrimental to squeezing. Silicon dioxide, on the other hand, does not suffer from these issues due to its large bandgap. However, silicon dioxide has a broad Brillouin and Raman gain window [199–202], which is probably the primary reason why the observation of squeezing has been obscured in silica microresonators, even though these microresonators have achieved ultra-high quality factors [79, 203] and have generated frequency combs [47, 204–206]. As we mentioned in Section 3.2.1, Raman and Brillouin scattering have historically limited the degree of observable squeezing in fibers, and a similar effect is expected for silica microresonators.

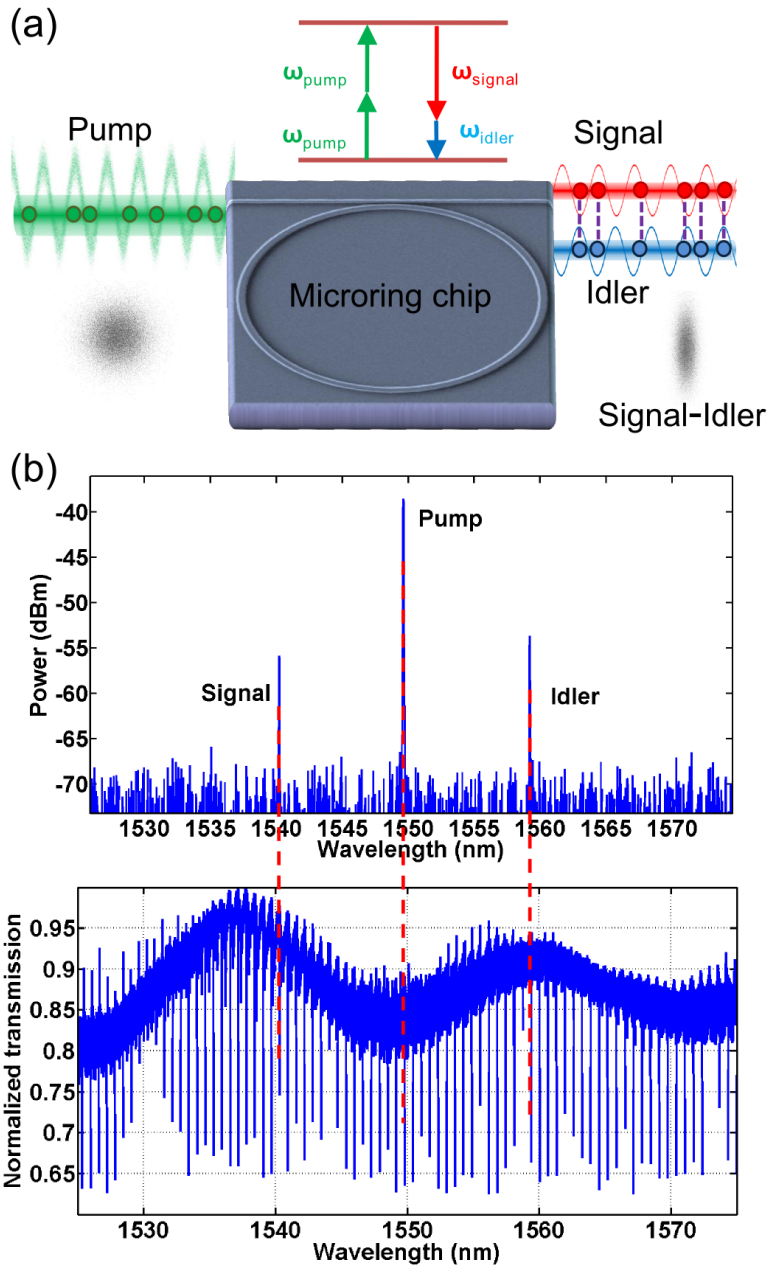

Figure 3.2: (a) Schematic of the generation of intensity correlated signal and idler beams via four wave mixing in the on-chip microring optical parametric oscillator (OPO). (b) Top: Optical spectrum analyzer scan of the light coupled out of the chip, at a pump power just above the parametric oscillation threshold. The Si_3N_4 ring is pumped at 1549.6 nm, generating signal and idler modes at 1540.2 nm and 1559.2 nm, respectively, which are 15 cavity modes away from the pump wavelength, as can be seen in the bottom figure. Bottom: Transmission spectrum of the ring for transverse electric (TE) polarization.

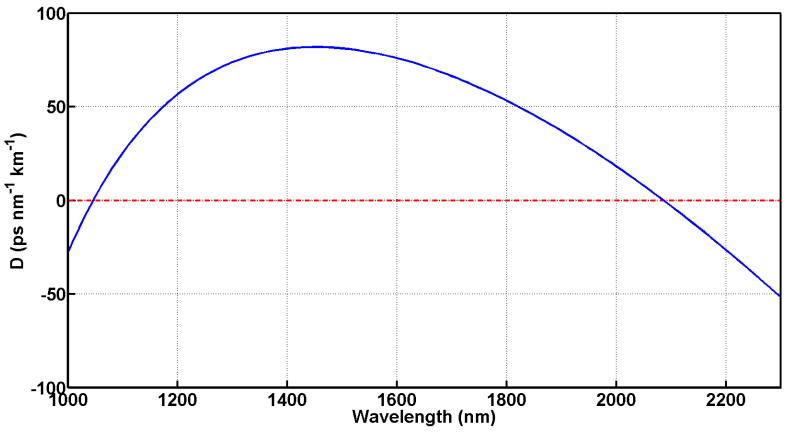

Figure 3.3: Group velocity dispersion of the 820 × 1700 nm waveguide used for the experiments in this chapter

Silicon nitride, as discussed in Chapter 2, is an ideal nonlinear platform for photonics in the telecom wavelength range because of the absence of broad Raman and Brillouin gain peaks. Our devices have a bus waveguide length of 1.5 mm and a ring circumference of 1.8 mm, corresponding to a free spectral range (FSR) of 80 GHz. In order to obtain FWM gain and optical parametric oscillation, the dispersion is engineered to be anomalous at the pump wavelength (see Fig. 3.3) to compensate for the Kerr nonlinear phase shift due to the pump [207, 208]. We design the ring waveguide cross section to be 820 nm high and 1700 nm wide, resulting in a slightly anomalous group velocity dispersion at the pump wavelength of 1549.6 nm.

From Eq. 3.20, one can derive the coupled amplitude equations for the fields in the microring to be [95],

$$\begin{aligned}\dot{\hat{a}}_l = &-\kappa\,\hat{a}_l + i\left[\Delta - \frac{1}{2}\zeta_2 l^2\right]\,\hat{a}_l + \delta_{l,\mathrm{pump}}\,\sqrt{2\kappa_\mathrm{c}}\,A_\mathrm{in} \\ &+ ig_0 \sum_{m,n,p} \delta(m-n+p-l)\,\hat{a}_n^\dagger \hat{a}_m \hat{a}_p \\ &+ \sqrt{2\kappa_\mathrm{c}}\,\hat{V}_{\mathrm{c},l} + \sqrt{2\kappa_\mathrm{i}}\,\hat{V}_{\mathrm{i},l} \end{aligned} \tag{3.21}$$

In deriving this system of Heisenberg-Langevin equations, we have introduced losses through terms of the form $(-\kappa_{c,i}a_l + \sqrt{2\kappa_{c,i}V_{c,i;l}})$, where c and i refer to the coupling loss channel and the intrinsic loss channel respectively. We can obtain the steady state classical solution for the mean fields by setting mean value of the vacumm fluctuations entering through the loss channels to be zero, and ignoring the time derivatives on the left hand side. This results in the pump power threshold for parametric oscillation Eq. 2.19. Next, we write down the equations for the output field at mode l, which are related to the input fields by the relation,

$$\hat{A}_{\mathrm{out},l} = \sqrt{2\kappa_{\mathrm{c}}}\,\hat{a}_l - A_{\mathrm{in}}\delta_{l,\mathrm{pump}} - \hat{V}_{\mathrm{c},l}\,. \tag{3.22}$$

In order to obtain significant squeezing, the cavity output coupling losses κ_c must be a large fraction of the overall losses. Relatively large losses are also desired for a large cavity bandwidth. On the other hand, a low pump power threshold is desirable, since it avoids detrimental thermal effects and also minimizes the influence of technical noise from the pump laser. The squeezing factor depends on the ratio between the internal ring losses, given by the ring's intrinsic quality factor (Q_i), and the coupling coefficient between the bus waveguide and the ring resonator, determined by the loaded quality factor (Q_L). The smaller the ratio of these losses, the better the squeezing obtained. Other important experimental parameters to achieve a significant, detectable twin-beam squeezing are (i) Nearly equal power in the signal and idler modes, which is possible if the quality factors of the resonances and the coupling loss out of the chip at the signal and idler frequencies are equal, (ii) a separation of 10-40 nm between the pump and the signal/idler modes, so that the grating and the balanced detectors have similar efficiencies, (iii) A low parametric oscillation threshold $\sim<$ few tens of mW. Any residual imbalance in the signal and idler beam power can be equalized using a variable optical attenuator on one of the beams. In experiment, we adjust the

power on the beams slightly till the twin beam intensity noise is minimized. Note that this only works if the imbalance is rather small ($< 20\%$), as larger attenuation of either beam would reduce the amount of squeezing detected. From Eq. 3.22, the squeezing factor of the intensity difference between the signal and idler fields, relative to the shot noise level, can be shown to be [35, 95, 152, 209],

$$S(\Omega) = 1 - \frac{\eta_c \eta_d}{1 + \Omega^2 \tau_c^2} \tag{3.23}$$

where Ω is the sideband frequency, τ_c is the cavity photon lifetime, η_d is the detection efficiency and $\eta_c = 1 - Q_L/Q_i$ is the ratio of the coupling losses to the total losses.

The simultaneous requirement of large coupling losses and low threshold is a challenge, since the threshold is inversely proportional to the product of Q_i and Q_L. We can meet these requirements by designing a ring with a very large Q_i, larger than 2 million, and operating in the highly overcoupled regime. The high intrinsic Q enables the generation of the beams with a low pump power threshold of around 90 mW despite operating in this overcoupled regime. The corresponding intracavity power is estimated to be 7 W, which is an order of magnitude lower than the intracavity pump oscillation threshold of 65 W in Ref. [210]. The loaded Q (200,000) is designed to be much lower than the intrinsic Q ($Q_i \approx 2$ million), facilitating a broad cavity linewidth of the order of 1 GHz. This is tantamount to a squeezing bandwidth of ~ 1 GHz.

The key to the realization of on-chip optical squeezing is the engineering of the dispersion and quality factors of the longitudinal modes of the microring resonator, to generate the twin beams at two well distinguished frequencies with low threshold pump powers. In contrast to many tabletop squeezing experiments, where the twin beams can usually be separated spatially based on their different polarizations, in

our platform the beams are co-propagating in the same output waveguide with equal polarizations, and therefore in order to be distinguishable, the beams are required to have well separated frequencies. A delicate interplay between the group velocity dispersion and the quality factor of the ring, which together shape the FWM gain curve around the pump determines at which frequencies the twin beams will be generated [95, 211, 212]. Specifically, the frequency difference between the pump and the first pair of oscillating signal and idler modes scales inversely as the square root of the second order dispersion (D_2) and the loaded quality factor (Q_L): $\omega_{\text{pump}} - \omega_{\text{signal}} \propto \text{FSR}/\sqrt{Q_L D_2}$. Here we engineer the structure to ensure that the signal and the idler beams are generated at two well distinguished wavelengths separated by around 20 nm, at 1540.2 and 1559.2 nm when the OPO is pumped at 1549.6 nm, enabling the beams to be spatially separated using a diffraction grating with an 85% efficiency. These two modes are 15 cavity resonances away from the pump wavelength, as can be seen from the transmission spectrum of the ring shown in Fig. 3.2(b). The large wavelength difference between twin beams not only enables spatial separation of the twin beams, but also enables filtering of the pump wavelength, which is essential to mitigate the effects of the residual pump from affecting the twin beam squeezing measurements.

3.3.1 Experimental setup

The experimental setup used to measure the squeezing is shown in Fig. 3.4. The ring was pumped by a continuous wave, tunable laser (New Focus Velocity 6328) followed by an erbium doped fiber amplifier (JDSU OAB1552+20FA6) and a band-pass filter (BPF) with a bandwidth of 9 nm to reduce the amplified spontaneous emission noise generated by the EDFA. Light is evanescently coupled to the mi-

croring through a waveguide. The output from the waveguide was collected with a high NA (NA = 0.25) objective lens, leading to a loss of less than 1 dB. A diffraction grating with an efficiency of 85% was used to spatially separate the pump and the two beams. The beams were propagated over a distance of 1.5 m in free space so that they were significantly diverged in space to reject the pump, and enable individual alignment of the two beams to the balanced detectors. After blocking the pump, the beams were focused on the two inputs of a Thorlabs PDB 150C balanced detector. The balanced detection system consists of a pair of well-matched InGaAs photodiodes with a quantum efficiency of 80%, followed by a low noise transimpedance amplifier to amplify the difference in photocurrents between the detectors. To observe the variance of the intensity difference noise between the two balanced detectors, the RF output of the balanced detection system was sent to an electronic spectrum analyzer. The detection system had a bandwidth of 5 MHz and a transimpedance gain of 10^5 V/A. The PDB 150 C has a variable gain-bandwidth setting, with gain varying from $10^3 - 10^7$, with a corresponding decreasing bandwidth of 150 MHz to 100 kHz. A small fraction (5%) of the light coming out of the chip was sent to an optical spectrum analyzer (OSA) to observe the onset of parametric oscillation. The setup includes a variable optical attenuator (VOA) to calibrate the shot noise level and to check the degradation of squeezing with attenuation of the twin beams.

We measure the squeezing in intensity difference of the two beams generated when the triply resonant OPO is pumped above threshold by comparing the noise level to the shot noise level generated from the coherent pump source.

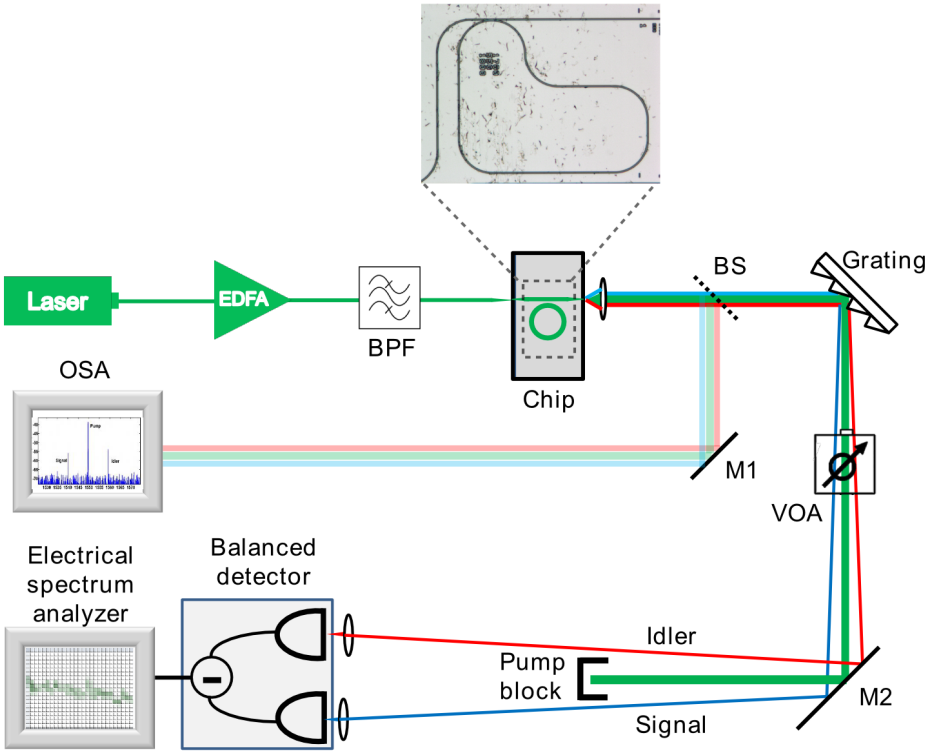

Figure 3.4: Experimental setup. The on-chip microring resonator is pumped by a continuous wave laser followed by an erbium doped fiber amplifier (EDFA) from JDS Uniphase and a bandpass filter (BPF). To ensure efficient coupling in and out of the chip, inverse tapers are used [213]. A lensed fiber is used for input coupling. The output from the waveguide is collected with a high NA objective lens. The diffraction grating spatially separates the pump and the twin beams. After blocking the pump, the beams are focused on a balanced detector. The RF output of the balanced detector is sent to an electrical spectrum analyzer. A small fraction of the beams is sent to an optical spectrum analyzer (OSA) to monitor the onset of parametric oscillation. The inset shows a microscope image of the ring resonator coupled to the bus waveguide. The shape of the fabricated ring is non-circular to fit the resonator within one field of the electron beam lithography tool and hence avoid stitching errors. EDFA: Erbium doped fiber amplifier. BPF: Bandpass filter. OSA: Optical spectrum analyzer. VOA: Variable optical attenuator. M1, M2: mirrors. BS: Beam splitter

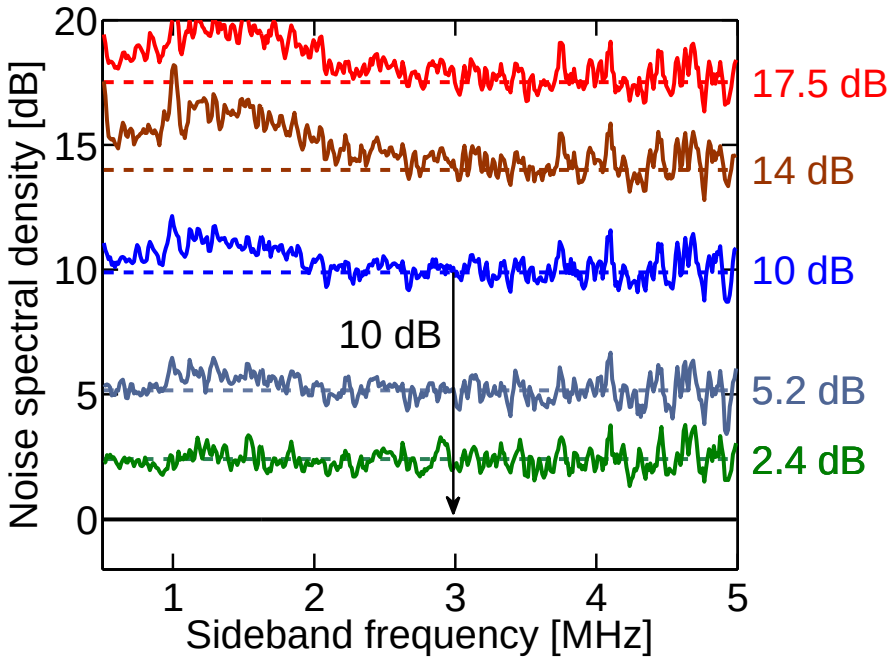

Figure 3.5: Linearity of the balanced detection system from 0.5 MHz to 5 MHz. The data have been dark noise corrected and normalized to the shot noise spectrum at a base local oscillator (LO) power of $P_0 = 7.8\,\mu$W, corresponding to the horizontal solid line at 0 dB. The dashed lines depict the mean optical power in the corresponding spectrum referenced to the base LO power P_0, in dB. There is significant technical noise at low frequencies, which is clearly evident at relative powers above 10 dB. The data have more fluctuations at high frequencies due to higher electronic noise and consequently lower dark noise clearance for the base LO power P_0. The dark noise varies from 5 dB below the 0 dB reference at 0.5 MHz to 1 dB below the reference at 5 MHz. Around 3 MHz, the detection system is linear over more than 20 dB, which is also substantiated by the linearity of the shot noise calibration measurement in Fig. 3.6.

3.3.2 Shot noise calibration

We calibrate the shot noise level by splitting the pump beam on a 50:50 beam splitter, directing the two halves to the two detectors and monitoring the DC and AC components of the balanced detector output simultaneously. The common mode rejection ratio (CMRR) of the detectors was independently measured to be more than 27 dB. The laser is detuned far from the microring cavity resonance during shot noise calibration measurements. The electronic noise of the detection system is measured by blocking all light incident on the detectors. As seen from Fig. 3.5, the detection system is linear over 20 dB near a sideband frequency of 3 MHz. There is excess technical noise at frequencies below 2 MHz, which cannot be rejected completely by the finite CMRR of the detection system. Focusing on the noise at 3 MHz, it can be seen from Fig. 3.6 that the shot noise level is linearly proportional to the optical power in each beam, in accordance with theory. This confirms that around 3 MHz, the CMRR of the detectors is high enough to reject common mode noise between the two beams, and are not saturated at these optical powers. We repeated the shot noise calibration measurements with multiple lasers - a tunable New Focus Velocity 6328 (linewidth $<$ 300 kHz), an NP Photonics Rock single frequency fiber laser (linewidth $\sim$ 10 kHz), and a RIO Orion single frequency planar laser (linewidth $<$ 3 kHz). The shot noise levels were found to be consistent between different lasers over several iterations of calibration to within 1 %.

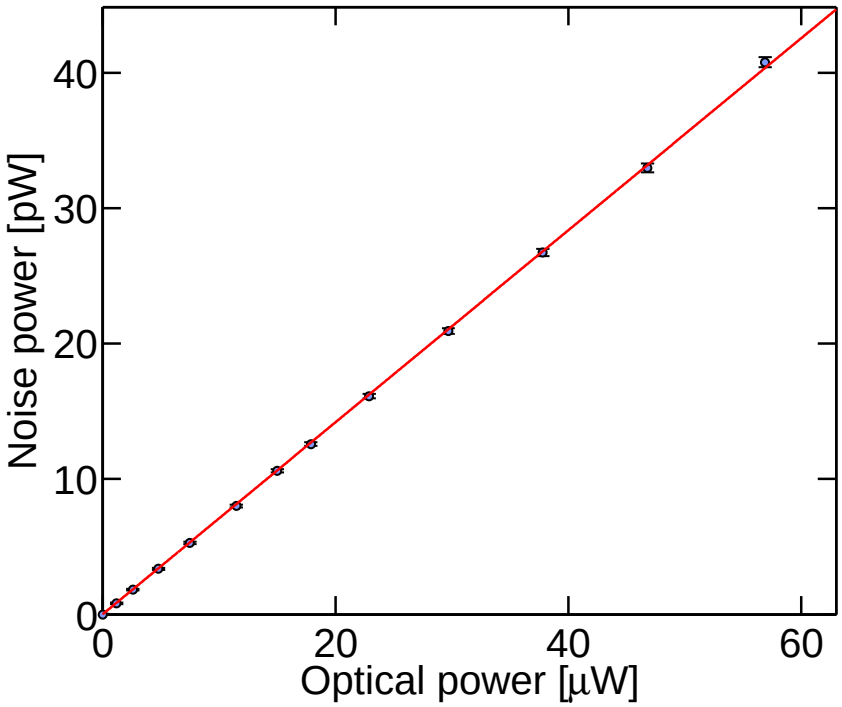

Figure 3.6: Shot noise calibration, showing the linearity of the noise power in the photocurrent difference with optical power, as expected from theory. The data are taken at a Fourier sideband frequency of 3 MHz, using a spectrum analyzer with a resolution bandwidth of 30 kHz and a video bandwidth of 100 Hz. Data points have been corrected by subtracting the electronic noise of the balanced detection system. Error bars are extracted from the raw data.

3.3.3 Squeezing measurements

We observe more than 30 % sub-shot noise quantum intensity correlations between the twin beams generated when the pump laser is tuned to an on-chip resonance at 1549.6 nm. Twin beam intensity difference squeezing measurements are presented in Fig. 3.7(a). The solid line corresponds to the signal-idler intensity correlation measurement, which is below the shot noise level, demonstrating clear intensity difference squeezing. These measurements were taken at Fourier sideband frequencies from 0.5 to 5 MHz, using a spectrum analyzer with a resolution bandwidth of 30

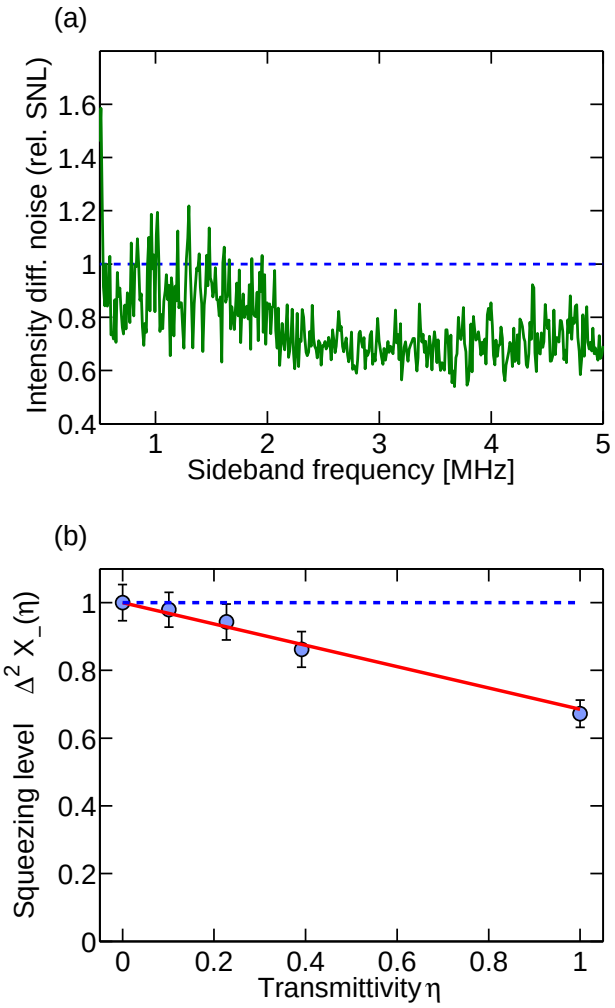

Figure 3.7: Intensity difference squeezing. a) The variance of the signal and idler photocurrent difference, normalized to the shot noise level (SNL), on a linear scale. The dashed line at 1 represents the SNL. The dark noise clearance was 16 dB at 0.5 MHz, and decreased to 5 dB at 5 MHz. The data was taken with a pump power of 93 mW. The power in the signal and idler beams is 45 μW, which requires low dark noise detectors, commercially unavailable at higher frequencies. Squeezing at low frequencies is masked by excess technical noise below $\sim$ 2 MHz, that can be clearly seen in Fig. 3.5. b) Variation of squeezing with attenuation at a sideband frequency of 3 MHz. The x-axis is the transmittivity of the variable optical attenuator, η. The y-axis is the intensity difference noise in shot noise units, - the variance of the signal and idler photocurrent difference compared. Error bars are determined from the standard deviation of the measured data points.

kHz and a video bandwidth of 100 Hz. Squeezing is not observed at very low frequencies, owing to technical noise in the pump laser. Note that the the ASE filter is absolutely essential to the observation of squeezing. In our experiments, we measured the noise with various optical filter bandwidths of 9 nm (WDM), 1 nm and 0.22 nm (tunable grating filter from JDSU). Since the signal and idler are typically > 10 nm away from the pump, a filter bandwidth of 9 nm is sufficient to reject most of the ASE noise directly at the signal and idler wavelengths. Hence, we did not observe any reduction in the individual noise levels or the twin beam intensity difference noise when the filter bandwidth was reduced below 9 nm to 0.22 nm. However, we observed > 5 dB reduction of the classical excess noise when a 9 nm ASE filter was introduced in the pump before the chip as opposed to an unfiltered pump. The on-chip OPOs used here could in principle act as a platform for generating large squeezing factors over broad bandwidths due to the highly overcoupled design of the rings.

We confirm that the squeezing factor degrades linearly with increasing attenuation, and the intensity difference noise approaches the shot noise level for high attenuation, as is typical of squeezed states (Fig. 3.7(b)) (see [214], Eq S1). By using the variable optical attenuator (VOA) in the experimental setup (Fig. 3.4), we measure the influence of decreasing transmission through the VOA on the squeezed twin beams. The dependence of the variance of the intensity difference noise, normalized to the corresponding shot noise level, can be modeled by mixing the unattenuated two-mode squeezed state with a vacuum state, on a beam splitter with transmittivity η:

$$\Delta^2 X_-(\eta) = \eta\, \Delta^2 X_-^{(0)} + (1-\eta)\, \Delta^2 X_v \tag{3.24}$$

where the left hand side represents the variance after attenuation, $\Delta^2 X_-^{(0)}$ represents the unattenuated variance (i.e. before the VOA), and $X_v = 1$ is the variance of vacuum. All variances are normalized to the shot noise level at the corresponding power.

The observed noise reduction of 1.7 ± 0.4 dB corresponds to a generated squeezing of 5 dB when corrected for detection losses and the non-ideal quantum efficiency of the detectors. This is less than the 10 dB of squeezing expected from the ratio of Q_i and Q_L owing to residual excess pump noise of 25 dB relative to the shot noise level, and the possible rotation of the optimally squeezed quadratures by the process of FWM [215, 216]. Furthermore, higher intrinsic quality factors of 7 million [71] and 37 million [77] have been demonstrated by us in silicon nitride rings, resulting in a lower oscillation threshold, which not only helps in reducing excess noise in the pump, but also leads to a higher ratio of Q_i to Q_L. Other groups have also reported improvements in the quality factor of nitride rings [60]. It should thus be possible, in principle, to reach much stronger noise reductions in this platform. Fundamentally the on-chip OPOs are expected to exhibit squeezing over GHz bandwidths in view of the broad linewidth of the cavity. We have demonstrated here squeezing in the MHz range, limited only by the bandwidth of our low-dark-noise detectors. It should be noted that commercially available detectors at 1550 nm have insufficient dark noise clearance at GHz sideband frequencies at optical powers of a few tens of μW, corresponding to the power in the generated twin beams just above threshold.

3.4 Conclusions and outlook

These results constitute an experimental demonstration of all-optical squeezing in an integrated CMOS compatible platform. Our source generates bright squeezed light using a singly pumped FWM process, in contrast to other sources of above threshold squeezing which utilize parametric down-conversion. Since FWM is based on the third order nonlinearity, the technique presented here can be extended to several different material platforms, in contrast to the more restrictive second order nonlinearity only found in non-centrosymmetric materials. Our demonstration paves the way for a myriad of on-chip quantum optics experiments over broad bandwidths in a scalable, compact and robust platform. A natural extension of the current chapter's experiment would be to measure phase-sum squeezing of the twin beams, enabling a demonstration of continuous-variable quantum entanglement [177] based on the inseparability criterion formulated by Duan *et al.* as well as by Simon [217, 218]. This will open the way to realize deterministic quantum information protocols at very high speeds. In future, the frequency separation of the twin beams can be done on chip using ring-resonator-based add-drop filters tuned to the signal, idler and pump wavelengths so that they are demultiplexed to different waveguides [219]. This opens up the possibility to cascade the on-chip OPO with photonic structures to manipulate squeezed and entangled states of light generated by the OPO, further emphasizing the highly scalable nature of our platform. The introduction of such non-classical light sources into future data communications by leveraging the mature infrastructure of microelectronics, currently being introduced into silicon photonics [2], is a very promising avenue to be explored. In the next chapter, we will look into one such exploration - external tuning of the degree of squeezing using coupled rings and microheaters.

CHAPTER 4

TUNING THE DEGREE OF SQUEEZING

For most applications of squeezed light, a higher degree of squeezing is naturally considered beneficial. This is true for general quantum enhanced sensing, spectroscopy and quantum information processing. [1]

Nevertheless, there exist applications where higher squeezing can be detrimental, such as quantum-enhanced optical phase tracking [99, 221]. There are other areas where one needs an optimal degree of squeezing to generate exotic quantum states like Schrödinger kittens. For such uses of nonclassical light, as well as from a fundamental point of view in terms of quantum state control, it is desirable to have an external knob that allows us to tune the squeezing level. This chapter demonstrates an electrical knob to continuously tune the degree of squeezing based on coupled ring resonators.

4.1 Applications of tunable squeezing

It is essential to control the squeezing factor for applications such as quantum enhanced optical phase tracking and for the generation of Schrödinger cat states [222]. A large degree of squeezing in one field quadrature is inevitably concomitant with a large anti-squeezing in the orthogonal quadrature, which increases the phase estimation error [99, 221]. It is convenient to classify phase estimation into two categories, phase sensing and general phase estimation. In phase sensing, the phase is always expected to lie within some small interval. For instance, in gravitational wave detectors, the interferometer is locked at the dark fringe, and

[1] This chapter has been published in Ref. [220]

miniscule variations of the arm lengths of the MZI are monitored about the dark fringe [223]. In such cases, the anti-squeezing in the orthogonal quadrature does not affect phase measurement error significantly, unless one is operating in the regime where radiation pressure noise dominates [99].

On the other hand, in general phase estimation [224–227], one is typically dealing with phases which are not constrained to small intervals and can lie anywhere in the interval $[0, 2\pi]$. The effect of anti-squeezing in the orthogonal quadrature is significant for phase estimation or phase tracking since it involves detecting large excursions in phase space from the mean value of the signal.

Following the treatment in Ref. [221], the effective squeezing factor $R_{\rm sq}$ for phase estimation including the contribution from anti-squeezing can be written as:

$$R_{\rm sq} = \Delta_f^2 \; e^{2r_p} + [1 - \Delta_f^2] \; e^{-2r_m} \tag{4.1}$$

where e^{2r_p} and e^{-2r_m} are the anti-squeezing and squeezing levels respectively, and Δ_f is the phase tracking error. It is clear from this equation that for small values of the tracking error $\Delta_f \ll 1$, $R_{\rm sq} \approx e^{-2r_m}$, as is the case for small phase sensing. For general phase estimation, the error Δ_f at any point in time can be significant enough that the anti-squeezing level starts to degrade the effective squeezing factor, canceling out the advantages of using quantum squeezed light. This is illustrated in Fig. 4.1. The mean square error was calculated by combining the above equation with Eq. 3 and S20 from Ref. [221]. We see that for low squeezing levels, the dashed red curve (ignoring the effect of anti-squeezing) agrees with the solid red curve (where anti-squeezing is accounted for). For increasing levels of squeezing, the phase error initially reduces, but turns around and increases beyond an optimal degree of squeezing. This is valid even for pure squeezed states (i.e. no degradation

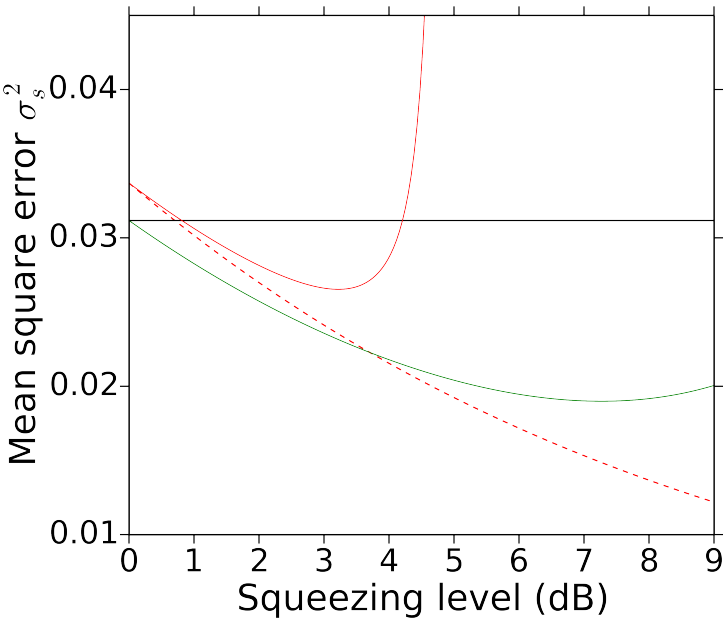

Figure 4.1: Plot of the rms phase estimation error vs. the squeezing level e^{-2r_m} for pure squeezed states (green) and for impure squeezed states (red) with a loss of 0.33. The dashed red line indicates the phase error ignoring the effects of anti-squeezing. It is clearly seen that there is an optimal degree of squeezing for these set of parameters for both pure and impure squeezed states, beyond which an increase in squeezing level increases the error. The optimal squeezing level is higher for pure squeezed states ($\sim$ 7 dB) and lower ($\sim$ 3.5 dB) for practical experimental squeezed states, i.e. when losses are taken into account. The solid horizontal line is the shot-noise limit, and operation below this line represents a quantum advantage [221].

of squeezing due to loss), as shown by the green curve. A theoretically optimum degree of squeezing of around 7 dB is obtained for pure squeezed states, which reduces to $\sim$3.5 dB when unavoidable experimental imperfections such as losses (of 33%) and finite bandwidths are taken into account [221]. Note that here the squeezing and anti-squeezing levels measured are related to the generated levels through the equations:

$$e^{2r_p} = \eta_l e^{2r} + (1 - \eta_l) \tag{4.2}$$

$$e^{-2r_m} = \eta_l e^{-2r} + (1 - \eta_l) \tag{4.3}$$

where e^{2r} is the pure squeezing level, and $0 < \eta_l < 1$ is the detection efficiency due to losses. For pure states $\eta_l = 1$, the product of the squeezing and anti-squeezing level is 1, and the state is one of minimum uncertainty as allowed by the Heisenberg relation. For impure states, the product of the measured squeezing and anti-squeezing level is always greater than 1, due to the effect of losses. The experimental data reported by Yonezawa *et al.* follow the solid red curve, and hence to obtain the lowest phase error, it is desirable to have a control knob that allows us to tune the degree of squeezing to the optimal value. Moreover, since the optimal degree of squeezing depends on the experimental parameters such as the bandwidth and loss of the measurement of feedback system, tunability is additionally helpful when these parameters are changed.

A tunable squeezing factor is also required to generate optical Schrödinger kittens or cats depending on the size of the desired cat state [222, 228–230]. A Schrödinger cat state is a quantum superposition of macroscopically distinct classical states. Typically, a superposition of coherent states with opposite phases, $|\psi\rangle_{\text{cat}} = N(|\alpha\rangle \pm -|\alpha\rangle)$, is considered a Schrödinger cat state, with $N = \sqrt{2 \pm 2\exp(-2\alpha^2)}$ representing a normalization constant for the wave function. The larger the value of α, the less the overlap $\exp(-2\alpha^2)$ between the two macroscopic states, and the better it approximates an ideal cat state. Such cat states have been proposed for use in optical quantum computing [231, 232]. A common way to produce kitten states (cat states with a low mean photon number) is through photon subtraction from a squeezed vacuum state. The highest fidelity of the targeted cat state is achieved when a squeezed state with a particular degree of squeezing is used. The optimal squeezing level required increases with the size

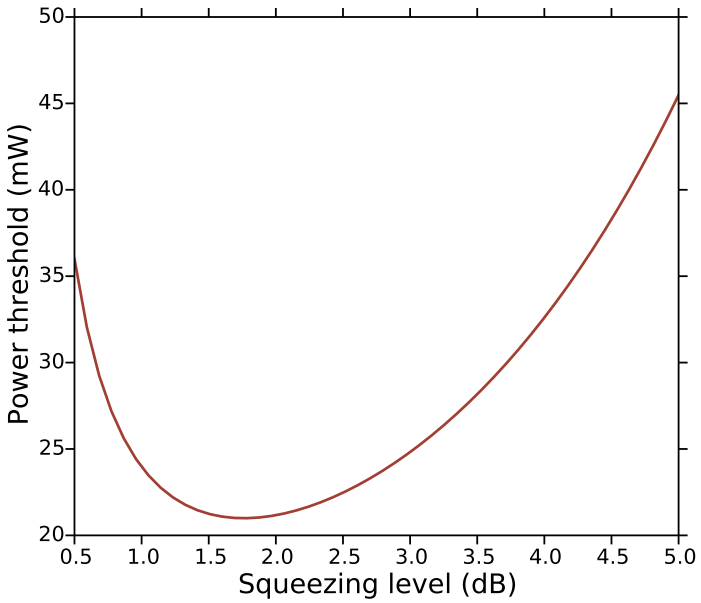

Figure 4.2: Plot of the theoretical threshold power vs. squeezing level for a typical silicon nitride microring resonator. The power threshold is minimum in the slightly undercoupled regime. The threshold increases rapidly in the overcoupled regime where strong squeezing is obtained. Hence, if an application requires a limited degree of squeezing, it is wasteful to operate at a high threshold power and attenuate it to the desired squeezing level. A tunable coupling mechanism is much more desirable so as to operate at a lower power threshold as needed.

of the cat state, as reported in [229].

4.2 Methods to tune squeezing

Conventional OPO cavities limit us to a fixed degree of squeezing, since they are usually made of discrete mirrors with a fixed reflectivity or using microresonators with a certain coupling. The coupling condition can in principle be modified by changing the mirrors, but this is a cumbersome process, especially for the monoli-

thic cavities used to achieve strong squeezing [122, 210], where the mirror coatings are deposited directly on the nonlinear crystal. More recently, tapered fibers [233] and diamond prisms [234, 235] have been used to control the evanescent coupling to whispering gallery mode microresonators, but this requires precise experimental control of the coupling gap at the tens-of-nm level. Note that the degree of squeezing below the oscillation threshold can be changed by varying the pump power [236, 237]. However, above threshold, the degree of squeezing in the intensity difference is independent of the pump power relative to threshold. In other words, as long as the input power P_{in} is greater than the oscillation threshold P_{th}, the intensity difference squeezing level is independent of the ratio P_{in}/P_{th} for a fixed coupling [154, 236]. Another way to tune the squeezing factor is to variably attenuate a highly squeezed state, but this method is inefficient since a large pump power is required to generate the initial highly squeezed state. This is because high squeezing is obtained from strongly overcoupled OPOs, which have a large oscillation threshold for the pump [234]. This is evident from Fig. 4.2

4.2.1 Our approach – tunable coupling

We chose to continuously tune the degree of squeezing by controlling the coupling condition. This is applicable to any cavity-based source of squeezed light. Here we demonstrate a tuning of the squeezing level generated in a silicon nitride triply-resonant microring OPO that was discussed in the previous chapter 3 [88]. Specifically, the noise in the intensity difference between the twin beams is reduced below the shot noise level, and this reduction or squeezing factor, above the

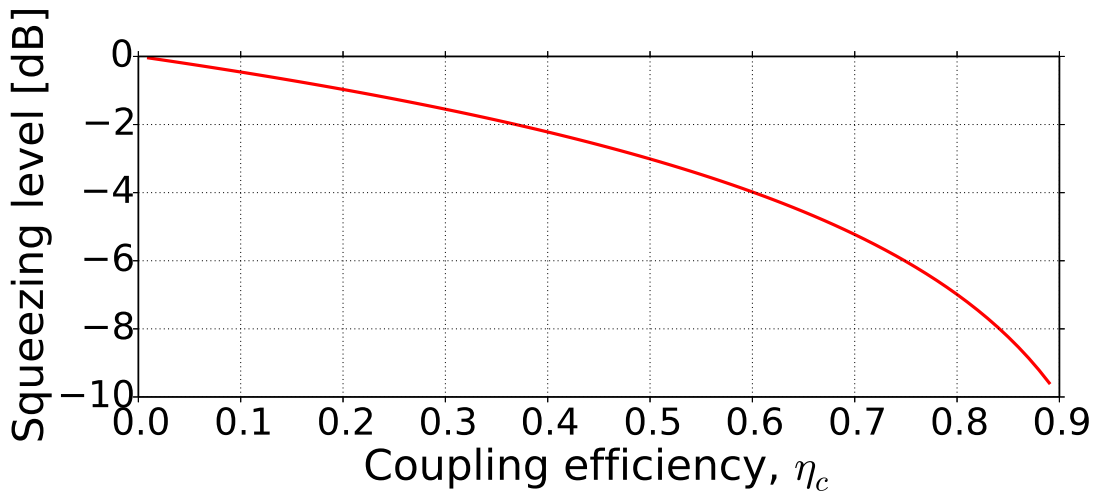

Figure 4.3: Theoretical plot of the low-frequency squeezing ($\Omega\tau_c \ll 1$) vs the coupling efficiency η_c, ignoring detection losses, based on Eq. 4.4. One can continuously tune the squeezing level by going across this curve.

oscillation threshold, can be quantified as [88, 152, 209, 238],

$$S(\Omega) = 1 - \frac{\eta_c \eta_d}{1 + \Omega^2 \tau_c^2} \tag{4.4}$$

where $S(\Omega)$ is the intensity-difference noise normalized to the shot noise level at a sideband frequency Ω; η_c is the coupling efficiency, i.e. the ratio of coupling loss to the total (intrinsic + coupling) loss; η_d is the detection efficiency, which takes into account the losses from the chip to the detectors as well as the nonideal quantum efficiency of the detectors; and τ_c is the cavity photon lifetime.

The tuning of the degree of squeezing is achieved here by externally controlling the coupling efficiency η_c of a double-ring system [Fig. 4.3]. Our device consists of two coupled microring resonators, each with a radius of 115 µm, as shown in Fig. 4.4(a). One of the rings, R1, is coupled to a bus waveguide to launch light into the double ring system, while the second ring, R2, is coupled only to R1.

By changing the offset between the resonance frequencies of R1 and R2, one can control the fraction of light in each ring and hence induce strong changes in the coupling condition of the double ring system to the bus waveguide [239, 240]. It should be noted that coupled cavity systems have been explored in various applications such as heralded single photon sources [241, 242], coupled-resonator-induced transparency [243, 244], four-wave mixing and frequency comb generation [23, 245–247]. Here we utilize a coupled two-cavity system to tune the generated squeezing factor.

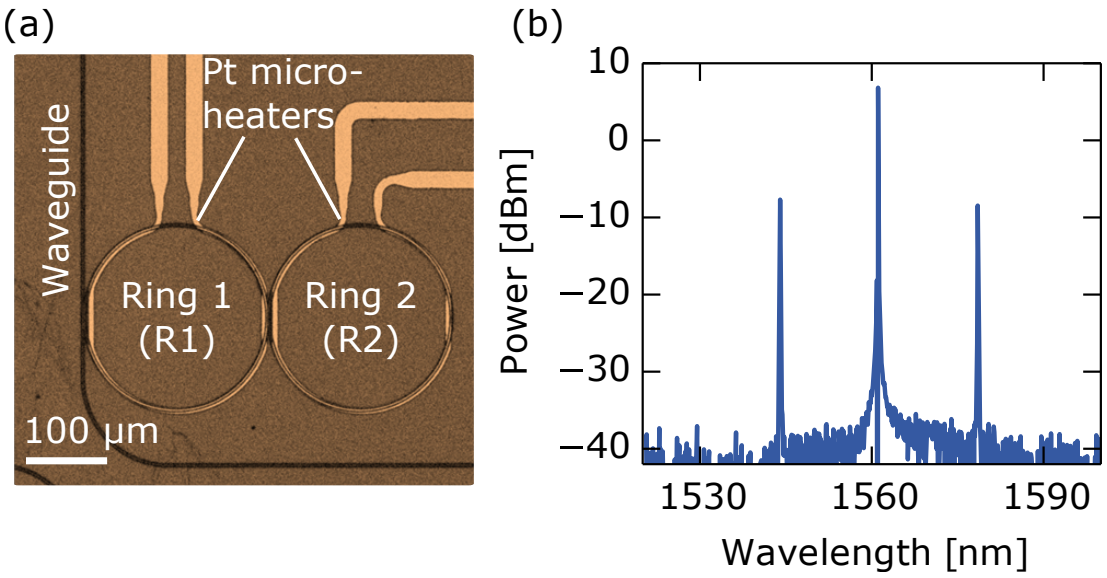

Figure 4.4: (a) Optical microscope image of the coupled double-ring system used to tune the degree of squeezing. (b) Optical spectrum analyzer scan of the pump, signal and idler modes.

4.3 Device design – coupled rings with microheaters

Our device uses microheaters integrated on double rings to thermally control the coupling efficiency η_c between the rings and the bus waveguide and consequently

tune the degree of squeezing. The squeezed light source is based on what was described in the previous chapter, i.e. a silicon nitride microring OPO. There are two major additions in the device used for tunable squeezing: (i) We use two mutually coupled rings instead of the single ring used before, (ii) We use platinum microheaters on top of the rings for thermal control. The rings were fabricated on 950 nm thick Si_3N_4 films grown using low-pressure chemical vapor deposition (LPCVD), with 4 µm of thermal oxide as the substrate. Trenches were defined in the wafer to mitigate stress-induced crack propagation in the nitride film, as described in [71]. The 1500 nm-wide waveguides were patterned with electron-beam lithography using ma-N 2405 resist on a JEOL 9500 system. Both rings have 6 µm wide platinum heaters which can be independently controlled to tune the resonance wavelength of the rings by the thermo-optic effect. To minimize losses caused by interaction of the optical modes with the platinum layer, the heaters and contacts were fabricated more than 2 µm above the Si_3N_4 layer. By thermally tuning the resonance wavelength of the double ring system to the pump laser at 1561.1 nm, bright signal and idler beams were generated at 1544.1 nm and 1578.5 nm, as shown in Fig. 4.4(b).

4.4 Results

4.4.1 Characterization of the mode crossing

As is typical of coupled cavity architectures, the double ring system exhibits an avoided crossing when the heaters on R1 and R2 are tuned to match the resonance wavelengths of the supermodes of the system to the fixed laser wavelength

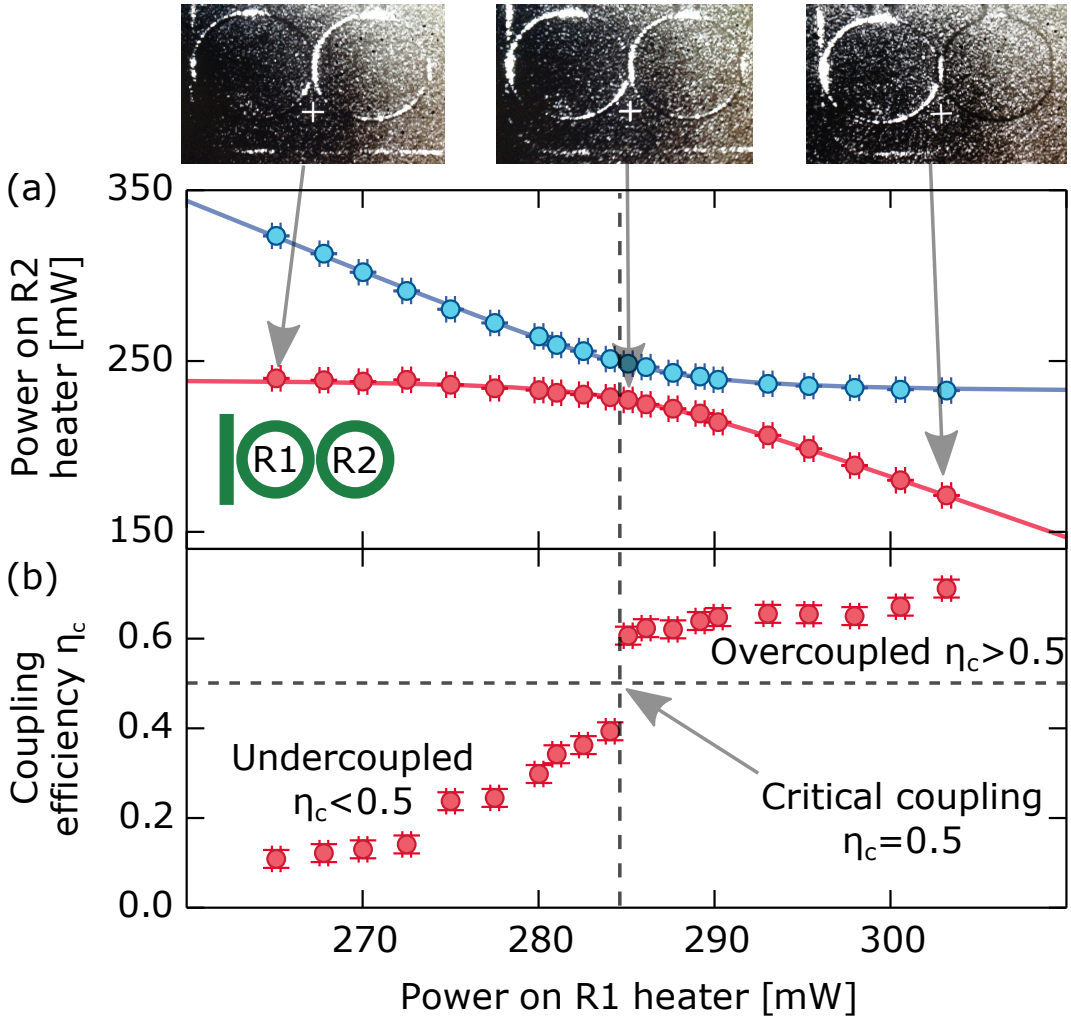

Figure 4.5: (a) Avoided crossing of the two-ring system, as the microheaters on the rings R1 and R2 are tuned to observe resonances at the fixed pump wavelength. The solid lines are fits to Eq. 4.5. From the top view IR images it is clear that light is initially localized in R2 and switches gradually to R1 as one tunes from one side of the avoided crossing to the other. (b) Coupling efficiency η_c vs. the power on the R1 heater, for the lower red branch of the avoided crossing.

(Fig. 4.5(a)). For these measurements, the input power coupled into the waveguide is kept below 5 µW to minimize thermal shift of the resonances due to the circulating optical power in the rings. From the top-view infrared camera images, we clearly see that the supermode of the double ring system undergoes a transition from being primarily localized in R2 to being localized in R1, for the lower red branch of the crossing.The eigenfrequencies of the supermodes can be written as,

$$\omega_{\pm} = \frac{\omega_1 + \omega_2}{2} \pm \sqrt{\left(\frac{\omega_1 - \omega_2}{2}\right)^2 + \kappa_{12}^2} \tag{4.5}$$

where ω_1 and ω_2 are the resonance frequencies of the two rings R1 and R2, in isolation, and κ_{12} represents the coupling coefficient between the rings. The solid lines in Fig. 4.5(a) are fits to Eq. 4.5, after accounting for the fact that the resonance frequencies of the rings change by approximately 1 GHz per mW of electrical power applied on the heaters [239]. For the remainder of this paper, we choose to focus on the lower red branch, although similar tunable coupling efficiencies were also observed for the upper branch. Note that avoided crossings have been reported between the transverse electric (TE) and transverse magnetic resonance wavelengths of a single ring resonator in the context of comb generation [248]. On the contrary, our design explicitly uses the fundamental TE modes of two coupled rings to generate tunable squeezing.

4.4.2 Tunable coupling

We observe a continuous change in the coupling efficiency η_c between the dual-ring system and the bus waveguide from 10% to 70% when tuning the heaters from one side of the avoided crossing to the other, as illustrated in Fig. 4.5(b). The coupling efficiency is determined from the expression $\eta_c = (1 \pm \sqrt{T_{\min}})/2$, where

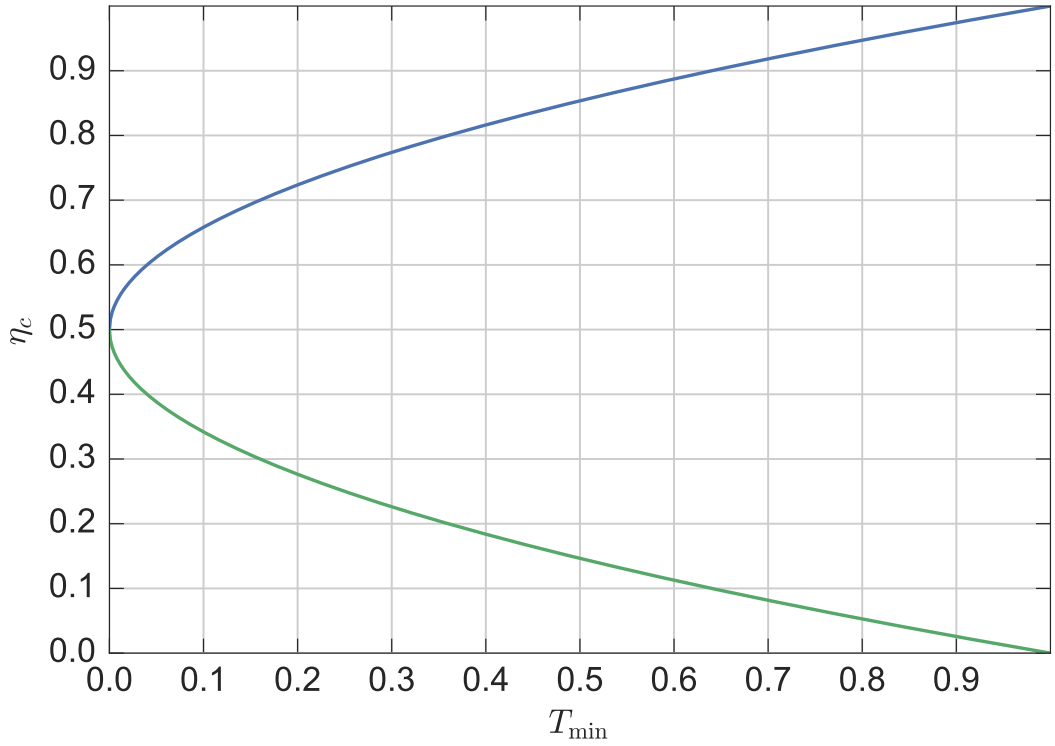

Figure 4.6: Coupling efficiency vs. minimum transmission on resonance for the overcoupled (blue) and undercoupled (green) regimes, based on the equation $\eta_c = (1 \pm \sqrt{T_{\min}})/2$. The + and - signs correspond to the overcoupled and undercoupled regimes. For a particular value of $T_{\min}$, one can determine whether the ring is overcoupled or undercoupled by monitoring in which direction the loaded quality factor moves when $T_{\min}$ changes. An increase in loaded quality factor indicates a movement of the ring from the overoupled towards the undercoupled regime.

the + and signs represent overcoupled ($\eta_c > 0.5$) and undercoupled ($\eta_c < 0.5$) regimes respectively, and $T_{\min}$ is the normalized transmission through the waveguide when the dual-ring system is on resonance with the laser [Fig. 4.6]. It should be emphasized that the directional coupling coefficient between the waveguide and R1 as well as between R1 and R2 is kept constant throughout the experiment, as these are fixed by the fabricated gaps between the waveguide and the rings. The maximum η_c is limited by the coupling coefficient of the bus waveguide to R1. The

change in overall coupling can be intuitively explained by looking at the supermodes of the two-ring system [239, 240]. The mode on the blue-detuned side of the avoided crossing has a weaker overlap with the bus waveguide than the mode on the red-detuned side, and hence the coupling efficiency increases as one moves from the blue-detuned side of the avoided crossing to the red-detuned side.

4.4.3 Experimental setup

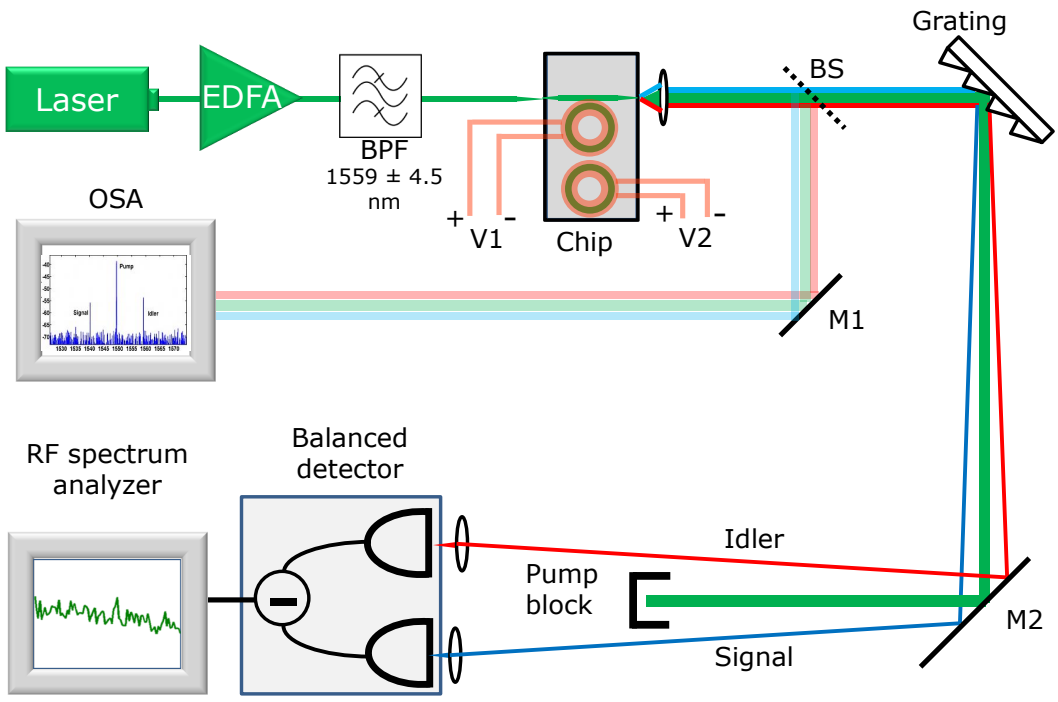

Figure 4.7: Experimental setup. EDFA: erbium doped fiber amplifier. BPF: bandpass filter. V1, V2: voltages applied to the microheaters on rings R1 and R2. BS: 1% beam sampler, anti-reflection (AR) coated on one surface. M1, M2: mirrors. OSA: optical spectrum analyzer.

We now describe the experimental setup used to generate and detect tunable squeezing as shown in Fig. 4.7, which is similar to the one described in the previous

chapter. The differences are outlined here. The rings are pumped by a low-noise single-frequency RIO Orion laser with a narrow linewidth < 3 kHz [249]. Etched facet inverse tapers are used to efficiently mode match the lensed fiber to the input of the waveguides [250]. The output of the chip is collected with an AR coated, high NA (NA $= 0.56$) aspheric lens to minimize losses to $\sim$12%. Tungsten electrical probes are used to apply voltages V1 and V2 to the contacts of the heaters on each of the two rings R1 and R2, respectively. The signal and idler beams are directed to the two arms of a balanced detection system (Thorlabs PDB450C-AC), which consists of a pair of InGaAs photodiodes with a quantum efficiency of 80%, followed by a low-noise transimpedance amplifier with a bandwidth of 4 MHz and a gain of 10^5 V/A. The difference of the photocurrents is sent to an RF spectrum analyzer to measure the noise in the intensity difference between the two beams incident on the detectors. About 1% of the output of the chip is sampled using a wedged beam sampler and sent to an OSA to monitor the onset of parametric oscillation.

4.4.4 Tunable degree of squeezing

We demonstrate a squeezing factor tunable from 0.5 dB in the strongly undercoupled regime to $\sim$2 dB in the overcoupled regime. In Fig. 4.8(a), we plot the directly measured squeezing (red) in the intensity difference between the signal and idler beams, as a function of the coupling efficiency between the waveguide and the R1-R2 dual-ring system. Each data point in Fig. 4.8(a) was obtained from time traces of the kind shown in Fig. 4.8(b). The shot noise level was independently calibrated by splitting the pump on a 50:50 beam splitter and showed a linear dependence with optical power, as expected from theory. All measurements were taken at a sideband frequency of $\Omega/2\pi = 3$ MHz, using a spectrum analyzer with

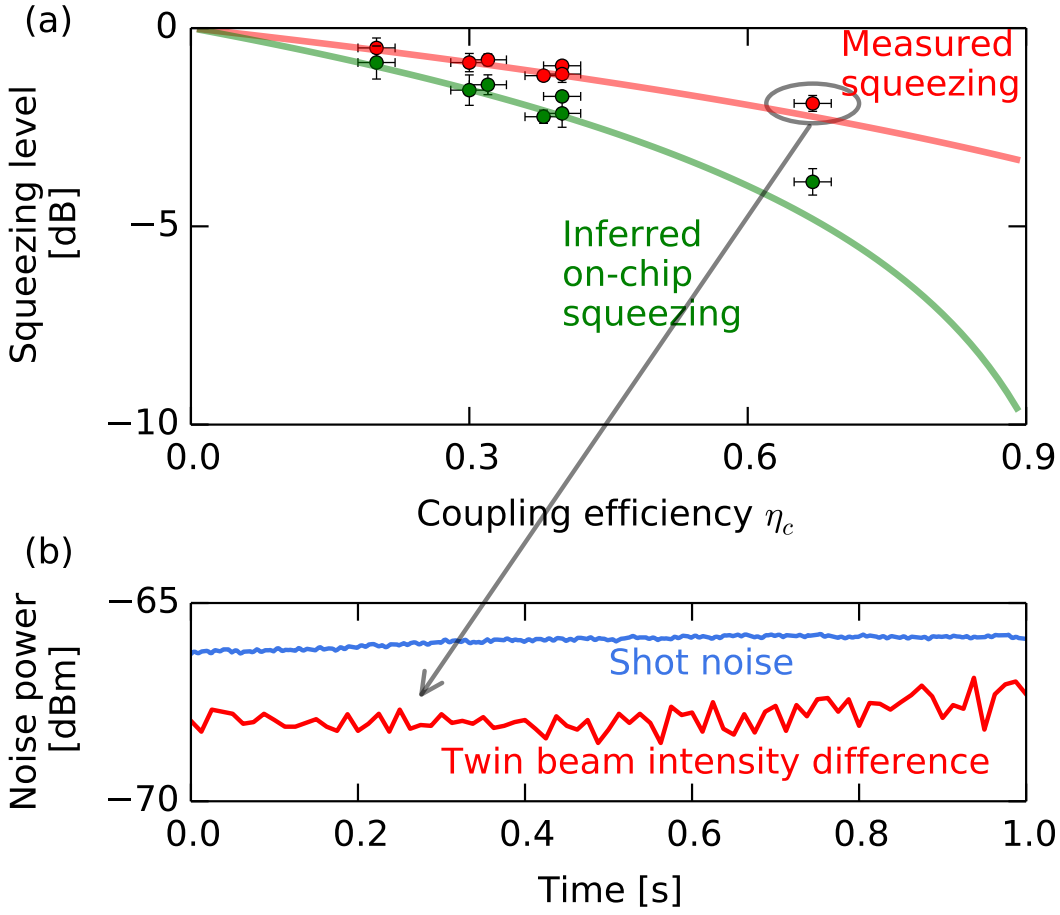

Figure 4.8: (a) The measured off chip squeezing (red) and inferred on-chip (green) squeezing levels for various η_c. The inferred on-chip squeezing is the level of squeezing generated on-chip, i.e. the expected degree of quantum noise reduction assuming $\eta_d = 100\%$. The data fit well to theoretical predictions based on the coupling and detection efficiencies (solid lines). Each data point in (a) is derived from time traces of the intensity difference noise, an example of which is shown in (b). (b) A time trace of the measured squeezing at a sideband frequency of $\Omega/2\pi = 3$ MHz. The dark noise is at -81 dBm.

a resolution bandwidth (RBW) of 30 kHz and a video bandwidth (VBW) of 100 Hz. The cavity lifetime at the signal and idler wavelengths was independently measured using a tunable laser to be $\tau_c = 0.5$ ns for the most overcoupled case, and increased to 1.3 ns for the most undercoupled case in our experiment. By accounting for the overall detection efficiency of 60%, we infer that the generated on-chip squeezing factor can be tuned from 0.9 ± 0.4 dB to 3.9 ± 0.3 dB. The measured and inferred squeezing levels match reasonably well with the predictions of Eq. 4.4 for $\eta_d = 60\%$ and $\eta_d = 100\%$ respectively. Note that different pump powers were used to achieve different levels of squeezing. For the most overcoupled case, we needed a pump power of 45 mW to reach the oscillation threshold, whereas much lower powers ~ 25 mW were needed for the critically coupled case.

The largest squeezing factor measured in our experiment was restricted by the maximum coupling efficiency of 70% that can be achieved in the current device. By using devices with a smaller coupling gap between the bus and R1, this factor could be increased even further. On the other hand, the smallest squeezing level that could be reliably resolved was limited by the fluctuations in the time traces of the intensity difference noise. The minimum detectable squeezing can in principle be reduced by video averaging or by using a smaller resolution bandwidth, but this increases the data acquisition time and would require greater long-term stability in the operation of the OPO than was possible in the setup.

4.5 Conclusions and outlook

In summary, we have introduced a technique to continuously change the degree of squeezing generated in an OPO by inducing strong changes in the coupling

condition through integrated thermal tuning. This technique can pave the way for on-chip realization of quantum-enhanced sensing protocols where an optimal degree of squeezing is necessary for attaining the maximum allowed sensitivity. The method demonstrated here can be extended to various on-chip platforms such as AlN, silica, diamond and silicon in which FWM oscillation has been reported [36, 50, 51, 251]. Specifically, in AlN, the nonvanishing second order nonlinearity can enable fast electro-optic tuning of the coupling condition through the Pockels effect [252], as opposed to the slower thermal response of microheaters used in our work. More generally, the concept of externally tuning the effective coupling coefficient by utilizing supermodes of a multiple-cavity system finds applications in several areas of classical and quantum optics. For example, it can be used to tune the conversion efficiency and bandwidth of frequency comb generation [239, 253]. Thus, coupled resonators are a useful tool to control nonlinear processes and the resultant nonclassical states of the light field generated in them.

CHAPTER 5

BEYOND TWO-MODE SQUEEZING: TOWARDS ENTANGLEMENT AND MULTIMODE CORRELATIONS

This chapter describes some preliminary experimental results on the path to move beyond twin-beam intensity difference squeezing that was shown in Chapter 3. In particular, we elucidate on the route towards an experimental demonstration of continuous variable entanglement on chip. Additionally, the Si_3N_4 platform is capable of generating a very large number of modes, forming an optical frequency comb [53, 54, 208, 254] often spanning more than an octave in frequency [57, 255]. We investigate multimode correlations between frequencies beyond the first pair of signal and idler modes generating by the OPO.

5.1 Multimode correlations

The experiments in Chapter 3 and 4 were carried out at pump powers just above the oscillation threshold of the OPO. On increasing the pump power, more modes gradually show up, due to four-wave mixing between the generated lines. A subtle point here is that the generation of higher order modes does not have a sharp threshold, because they can be produced by four-wave mixing of the first signal and idler modes with the pump. This is in contrast to the first pair of modes which are generated from vacuum fluctuations, and they can hence be generated only when the parametric gain overcomes the roundtrip loss in the ring.

The advent of the "cluster state" model of quantum computing has provided impetus to the development of multimode quantum correlated states. This model is related to the one-way quantum computer proposed initially by Raussendorf and

Briegel in the discrete variable regime [256], and later extended to the continuous variable (CV) regime by Braunstein, Menicucci and several others [172, 186, 257]. Also called the measurement-based quantum computer, such a model first requires the preparation of a highly entangled resource state, called a cluster state. Local measurements are then performed on this state to make the computation proceed such that the original cluster state is always destroyed (lending it the name "one-way") but the result of the computation is successful. Initial proposals to generate cluster states consisted of the production of single mode squeezed states which were then mixed on beam splitters [188, 257]. This technique suffers from a scalability issue because of the requirement to produce many squeezed states in tandem. It was soon realized that a single Gaussian multimode state could embody all of the correlations needed to create a cluster state, drastically reducing the complexity on the generation side [188, 258, 259]. The trick was to use a single multimode OPO combined with a multifrequency pump beam, in a formation akin to an optical comb. This is a *top-down* manner of creating a multipartite entangled state, rather than the bottom up method of mixing squeezed states on a beam splitter.

The optical frequency comb has been specifically proposed as a fertile ground to generate a cluster state [187, 258, 259]. This is not surprising, as the nonlinear interactions between the modes of the comb would typically result in quantum correlations. The frequency comb directly produced by a mode-locked laser [260] does not necessarily have quantum correlations between its modes, but is correlated classically since the modes are phase-locked to each other. When such a comb is down converted using a nonlinear medium placed in a cavity whose FSR matches the repetition rate of the modelocked laser, a multimode quantum correlated state is formed, as shown in Fig. 5.1 (b). Such a method has been experimentally

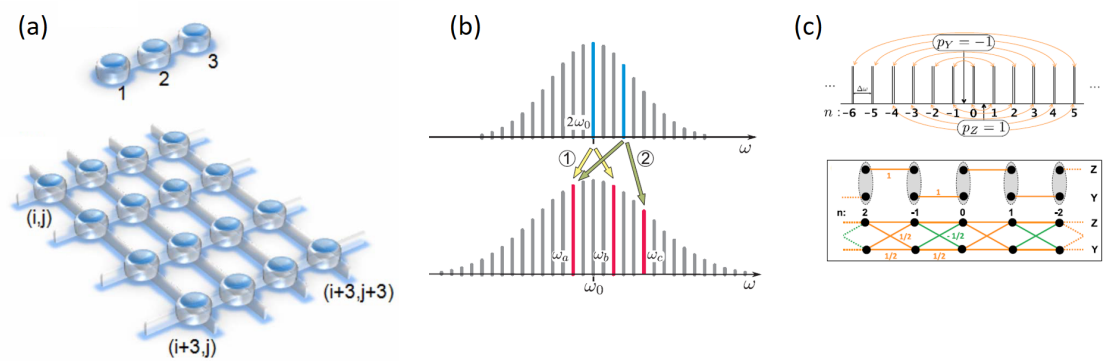

Figure 5.1: **Cluster states**. (a) A theoretical proposal by Gu et al. showing a 1D and a 2D cluster state with many connected modes sharing connections [188]. (b) An experimental schematic for realizing cluster states using a downconverted quantum frequency comb [190, 261]. The arrows show the modes which are generated by an energy conserving parametric down conversion process and posses pairwise quantum correlations. (c) Another scheme for realizing cluster states using modulated pulses [192, 262].

implemented by Roslund *et al.* to show entanglement between 10 modes and 511 bipartitions [190, 261]. In a different scheme [Fig. 5.1(c)], a c.w. laser was sent through a pair of orthogonally oriented nonlinear crystals in a cavity to generate cluster states spanning 60 modes [192, 262]. While these schemes rely on modes which are frequency multiplexed, the largest cluster state produced till date was multiplexed in the time domain by Yokoyama *et al.* [189]. They showed an ultra-large multipartite entangled state with more than 10,000 modes. A proposal to combine the frequency and time-domain approaches has been reported recently [263].

While the demonstration of large-scale multipartite entanglement in previous experiments is promising, these experiments date rely on bulky tabletop and fiber-based setups. With these recent developments in mind, it is natural to look for

more compact and scalable systems to generate multimode quantum correlations in the CV regime. Microresonator based Kerr frequency combs have the potential to generate multimode cluster states in an on-chip, compact and robust platform. The essential difference between the implementations described above and the Kerr comb platform is, while the former is based on the second-order $\chi^{(2)}$ nonlinearity, the latter exploits the more ubiquitous third order $\chi^{(3)}$ nonlinearity found in all materials. Moreover, a $\chi^{(3)}$ system is anticipated to exhibit richer dynamics because the third order nonlinearity can couple a larger number of modes at a time than its $\chi^{(2)}$ counterpart, and introduce correlations even between non-twin beams (i.e. signal and idler modes asymmetrically located in the spectrum with respect to the pump). A calculation of pairwise quantum correlations of Kerr combs has been reported by Chembo, both below as well as far above threshold [95]. Microresonator based OPOs and their transition to the mode-locked frequency comb state have been explored classically both in the temporal and the spectral domain [211, 212, 264–267]. These techniques look at the properties of the entire comb and do not provide direct information about correlations existing between different modes, especially below the transition to the mode-locked state. On the other hand, significant theoretical and experimental progress has been made in understanding the dynamics of comb formation. In this context, a thorough understanding of the comb dynamics and correlations between various modes is desirable to enable their use in the generation of multipartite entanglement.

We experimentally study the correlations between signal and idler modes that are asymmetrically located in frequency with respect to the pump. The modes located on the blue side of the pump are referred to as signal modes, and those on the red side are referred to as idler modes for the remainder of this chapter. We use a modified version of the setup introduced in Fig. 4.7, as shown in Fig. 5.2.

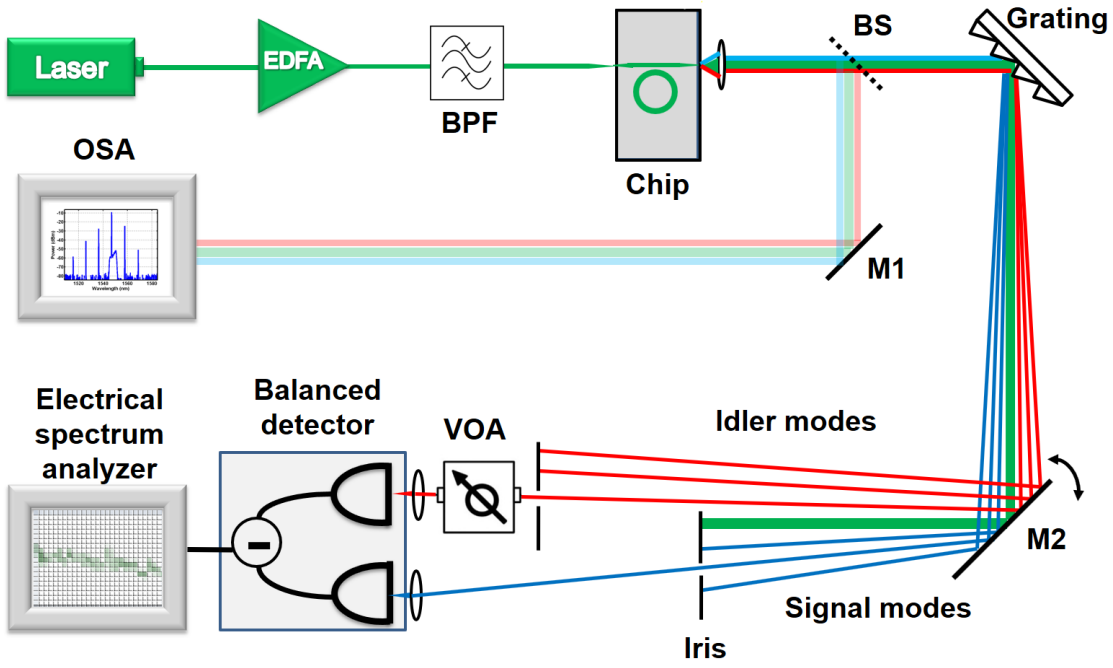

Figure 5.2: Modified version of experimental setup used to measure twin-beam intensity difference squeezing, adapted here for characterizing multimode correlations. VOA: variable optical attenuator. BS: beam splitter. BPF: band pass filter. M1, M2: mirrors.

The desired mode from the output of the chip is chosen using a rotating mirror and a pair of irises. Since signal and idler modes asymmetric with respect to the pump in frequency are typically of different powers, a variable optical attenuator (VOA) is used to equalize the power of the beams reaching the balanced detectors. This is important because the detectors' noise performance is best when the optical power incident on them is not too different (within ~ 50 µW).

Fig. 5.3 (a) depicts the optical spectrum generated by pumping the silicon nitride microring OPO around 9% above threshold. Chapter 3 studied sub-shot-noise correlations between modes signal 1 and idler 1. Here, we observe 22 dB near-shot-noise-limited intensity correlations between the non-twin beams. When the pump wavelength was tuned to a resonance of the ring at 1546.9 nm, several

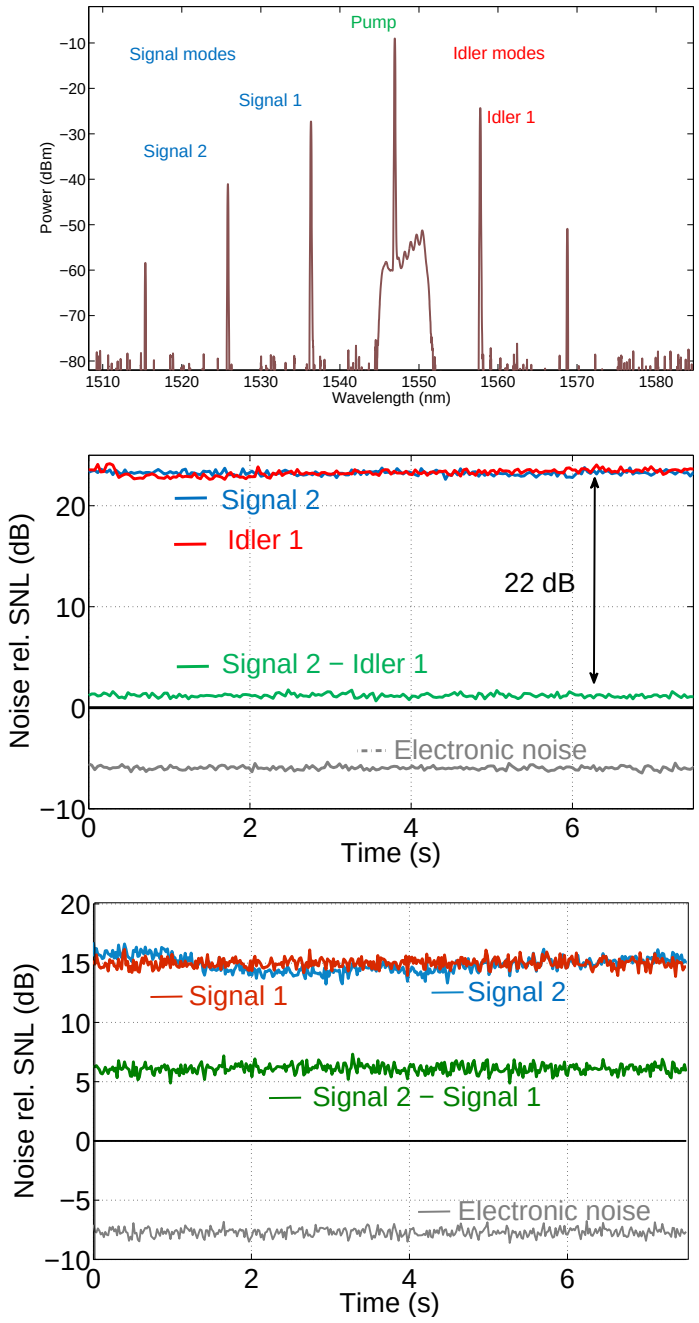

Figure 5.3: (a) Optical spectrum of the Si_3N_4 OPO pumped at 1546.9 nm. (b) Intensity noise in the signal 2 beam (blue), idler 1 beam (red) and the difference (green) at a sideband frequency of 3 MHz. The traces are normalized to the shot noise level (SNL) corresponding to 21 µW, which is the optical power in the beams after attenuating idler 1 for optimal correlations. (c) A much smaller correlation is seen for two signal beams located on the same side of the pump. Resolution bandwidth: 30 kHz, video bandwidth: 100 Hz.

bright signal and idler beams were generated as shown in Fig. 5.3(a). The intensity correlation between the modes at 1525.8 nm (depicted as signal 2) and at 1577.8 nm (depicted as idler 1) was measured to be 22 dB, within 1 dB of the shot noise level (SNL) at an optical power of 21 µW [Fig. 5.3(b)]. One can calculate the normalized correlation coefficient [268] between these two modes,

$$C(\omega) = \frac{S_{12}(\omega)}{\sqrt{S_{11}(\omega)S_{22}(\omega)}} \tag{5.1}$$

where the symmetrized cross-correlation coefficient between the modes i and j is defined by,

$$S_{ij}(\omega) = \frac{1}{2}\langle \delta I_i(\omega)\delta I_j(\omega)^* + \delta I_j(\omega)\delta I_i(\omega)^*. \tag{5.2}$$

We can use a modified relation $S_{12} = (S_{11} + S_{12} - S_d)/2$ to calculate the normalized correlation coefficient in our system to be 0.997, corresponding to nearly perfect correlations between the two beams. S_d represents the intensity difference noise measured in our setup. Idler 1 was attenuated by $\sim$ 15 dB to equalize the power in the two arms of the balanced detector. This, along with the excess noise of the pump, precluded the observation of quantum correlations below the shot noise level. We estimate the excess noise in the signal and idler beams solely due to FWM-converted excess pump noise to be around 11.5 dB at this optical power. This is close to the intensity correlation observed between signal 1 and signal 2 of around 10 dB. As expected the correlation between signal 2 and idler 1 is much stronger than that between signal 2 and signal 1 [Fig. 5.3(c)] since the former can be produced in pairs, $\omega_{\text{pump}} + \omega_{\text{signal1}} = \omega_{\text{signal2}} + \omega_{\text{idler1}}$, i.e. by nondegenerate FWM of the pump and signal 1, while there is no FWM process to produce signal 2 and signal 1 in pairs at these pump powers.

Nevertheless, the correlations presented above are classical as they are still

above the shot-noise level. To demonstrate quantum correlations, we need to mitigate the effect of excess noise in the pump laser. Besides, the measured intensity difference squeezing level in chapter 3 was less than that expected based on the coupling efficiency and detection loss. Hence, a reduction in the pump excess noise would be beneficial to increase the degree of squeezing. As we stated earlier, a demonstration of entanglement requires the simultaneous verification of intensity-difference squeezing and phase-sum squeezing. While intensity difference squeezing is a robust parameter and can be detected even in the presence of some excess noise (as long as the CMRR of the balanced detection system is high enough), phase-sum squeezing is much more sensitive to excess amplitude and phase noise in the pump [269]. All of these issues indicate that a thorough characterization of the pump laser noise is required.

Towards this end, we build a filter cavity to attenuate the fluctuations in the pump beam around the sideband frequency of 3 MHz, where we measure squeezing. The design and characterization of the filter cavity is described in the next section.

5.2 Mitigating pump laser noise

First, we measure the pump laser's intensity noise by using a setup similar to the shot noise calibration discussed in Section 3.3.2, but blocking the beams incident on the balanced detectors one at a time [Fig. 5.4]. The intensity noise fits to a quadratic polynomial, which is in accordance with the expectation that the excess noise should vanish at very low optical powers.

We see that the pump deviates from being shot noise limited at optical powers above $\sim$ 50 µW. At a power of 500 µW, the pump noise exceeds the shot noise

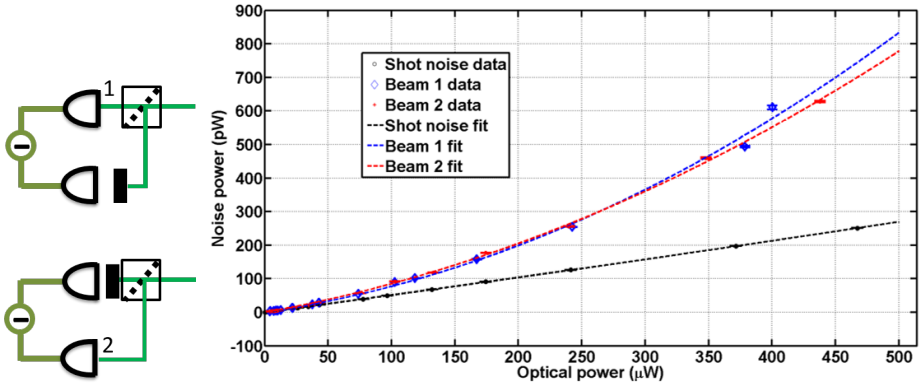

Figure 5.4: Intensity noise characterization of the pump laser beam. For shot noise calibration, both the inputs to the balanced detector are open. For intensity noise measurements, we block the beams one at a time, as depicted by the schematic on the left panel. While the shot noise is independent of the light source used, the intensity noise is a strong function of the laser. This plot is similar to 3.6 but has quadratic fits to the intensity noise in addition to the linear fit for the shot noise. The electronic dark noise has been subtracted from these measurements. RBW: 30 kHz, VBW: 100 Hz.

level by a factor close to 3. The microrings are pumped by much higher powers, of the order of tens of mW, and the residual noise in the pump is estimated to be comparable to the shot noise level after the excess common mode noise has been reduced by the finite CMRR of the balanced detection system. The residual noise increases with an increase in pump power, which explains the difficulty in observing quantum correlations for the multimode case. To mitigate excess pump laser noise, we design a transmittive filter cavity which would be inserted in the setup between the EDFA and the chip. This would act like a narrowband passive filter which strongly attenuates the excess amplitude and phase noise at the measurement frequencies of interest.

5.2.1 Design of filter cavity

The filter cavity is implemented in a bowtie configuration [270–272], using two flat mirrors and two high-reflectivity curved mirrors. It is essential to have a moderately high transmission efficiency as we will be using the transmitted beam as the pump for the microring OPO. We aim to design a traveling wave cavity with a linewidth lower than 10 times the measurement frequency. For our purposes, the measurement frequency is $\Omega/2\pi = 3$ MHz in the majority of the experiments reported here. This motivates a filter cavity linewidth of $\Delta\nu_{\mathrm{FWHM}} = 200$ kHz. A finesse of around 300 is feasible without compromising on the transmission efficiency significantly (the finesse is defined as the ratio of the FSR to the FWHM of the cavity). The expression for finesse is

$$F \approx \frac{\pi\alpha(R)^{1/4}}{1-\alpha^2\sqrt{R}} \tag{5.3}$$

where $R = \prod_i R_i$ is the product of power reflectivities of all the mirrors and $\alpha^2 = 1-\epsilon$ with ϵ being the fractional single-pass spurious power loss. The transmission efficiency is $T^2/(T+\epsilon)^2$, where $T = 1 - R_2$, is the transmittivity of the output coupling mirror. Assuming low spurious loss, we estimate a finesse of 300 for an input and output coupler reflectivity of 99 % and a transmittivity of 1 %. To achieve a cavity linewidth of 200 kHz with this finesse, the free spectral range of the cavity would need to be

$$\Delta\nu_{\mathrm{FSR}} = \Delta\nu_{\mathrm{FWHM}} F = 60 \text{ MHz} \tag{5.4}$$

In other words, the total cavity length would need to be $L = c/\nu_{\mathrm{FSR}} = 5$ m. For a bowtie cavity with a shallow angle, this corresponds to an arm length one-fourth of the total length.

A schematic of our constructed cavity is shown in Fig. 5.5. It consists of flat

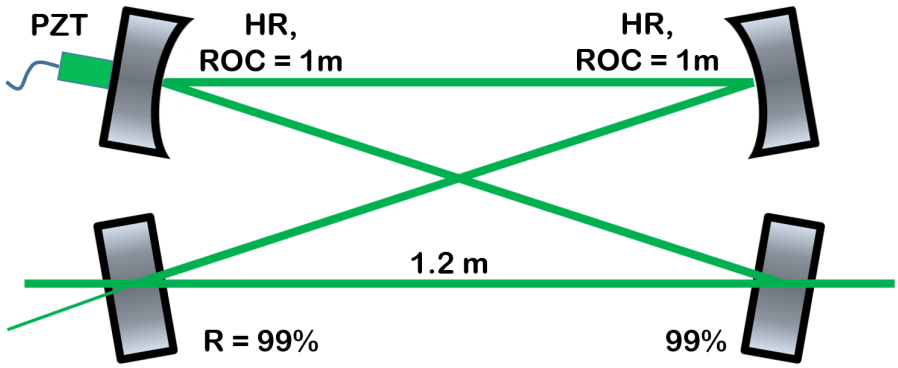

Figure 5.5: Schematic of the filter cavity. The laser beam to be filtered is incident from the left. HR: high reflectivity. PZT: piezoelectric transducer

input and output coupling mirrors with the desired reflectivity of 99 %. The other two mirrors have a radius of curvature of 1 m and a reflectivity higher than 99.9 % (Newport supermirrors). These specifications are for s polarization. The cavity is not too sensitive to polarization due to the shallow angles of incidence on the mirrors (< 1.5 °). The distance between the input and output coupling mirrors is 1.2 m, and the total cavity length is 4.9 m, resulting in an FSR of 61 MHz. The beam waist is calculated to be 0.22 mm in radius between the two curved mirrors and 0.8 mm between the two flat input and output couplers. A piezoelectric transducer (PZT) is glued to the holder for one of the mirrors before fastening it to mount. The PZT enables us to scan the cavity length across resonances and will be used for locking the cavity later.

Fig. 5.6(a) and (b) show some pictures of the initial prototype cavity that we built with discrete optical components and posts. We deposited the 99% reflective coatings for the input and output coupling mirrors on a silicon wafer in the cleanroom using plasma-enhanced chemical vapor deposition (PECVD). The process of designing the mirrors and depositing them is explained in Appendix C. After we verified the prototype, a more stable cavity was built on an aluminum base

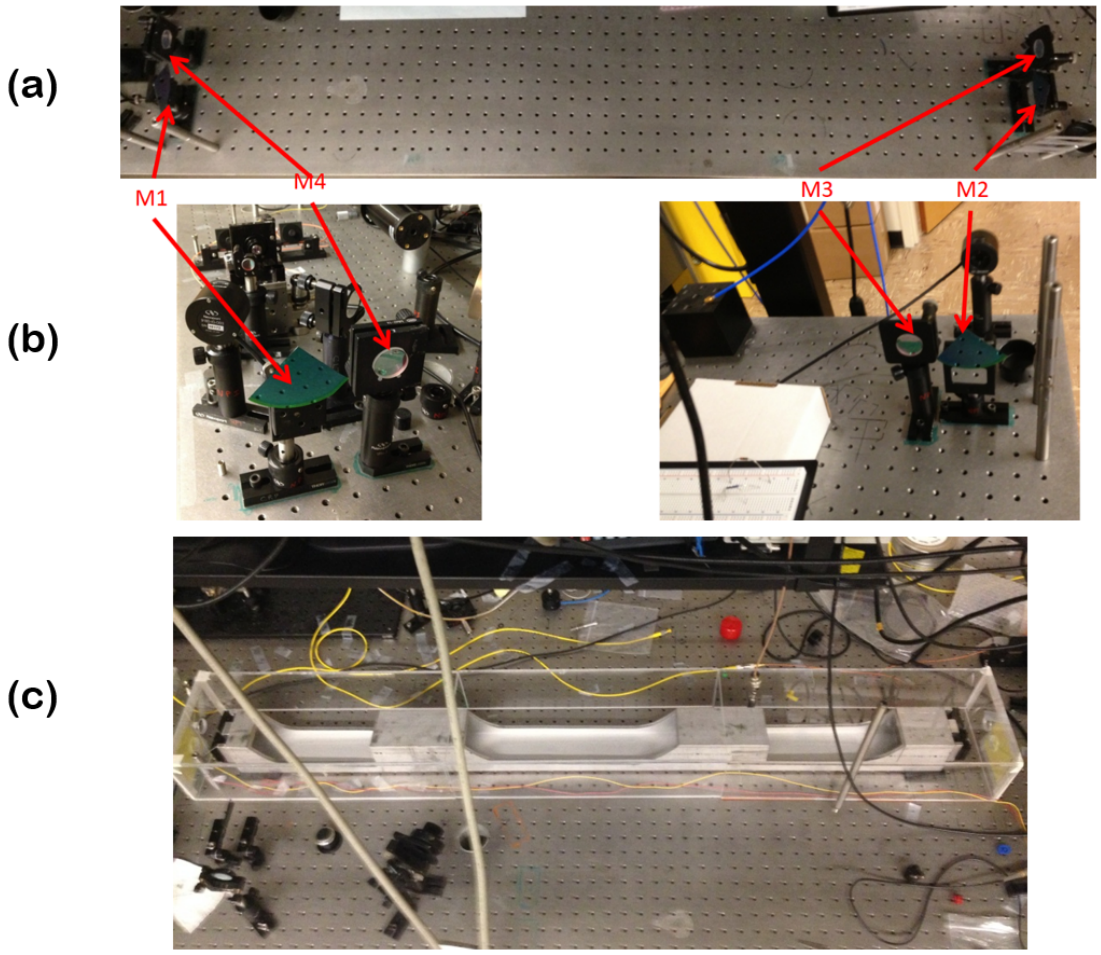

Figure 5.6: (a) Top view image of the prototype filter cavity built with discrete mounts and posts. (b) Zoomed view of the mirrors. The input and output couplers can be seen as pieces of a silicon wafer with deposited mirror coatings on them. (c) A more stable cavity design, mounted on an aluminum base with sorbothane pads underneath. The plexiglass box reduces air currents and thermal fluctuations from entering the space between the mirrors.

platform with flexure mirror mounts bolted to the ends of the platform 5.6(c). Such a configuration reduces the relative drifts between the four mirrors. Sorbothane pads were used between the base platform and the optical table to damp mechanical vibrations which affect the stability of the cavity. Additionally, we enclosed the cavity in a transparent plexiglass box to reduce air flow and thermal currents. The box had circular apertures for the input and output beams. These steps significantly reduced the short time cavity drift by approximately a factor of five.

5.2.2 Characterization

We measure the linewidth of the cavity by applying a triangular waveform to the PZT through a piezo controller (Thorlabs MDT693A, 0-150 V) and recording the transmitted and reflected powers. The piezo controller has an input port which accepts a modulation signal. This signal is amplified by a factor of 15 and added to the DC offset on the front panel to produce the output driving signal for the PZT. The frequency axis is calibrated by noting the voltage required to tune across one full FSR, using a scan of the form shown in Fig. 5.7. We fitted the triangular waveform recorded from the 8-bit oscilloscope by an ideal ramp function to alleviate the effects of digitization noise. This step is essential to get a good calibration of the frequency axis unless a higher bit resolution is used. Using this calibration, a Lorentzian fit to the resonances yields a 3 dB cavity linewidth of $\nu_{\mathrm{FWHM}} = 200$ kHz, in accordance with the initial design.

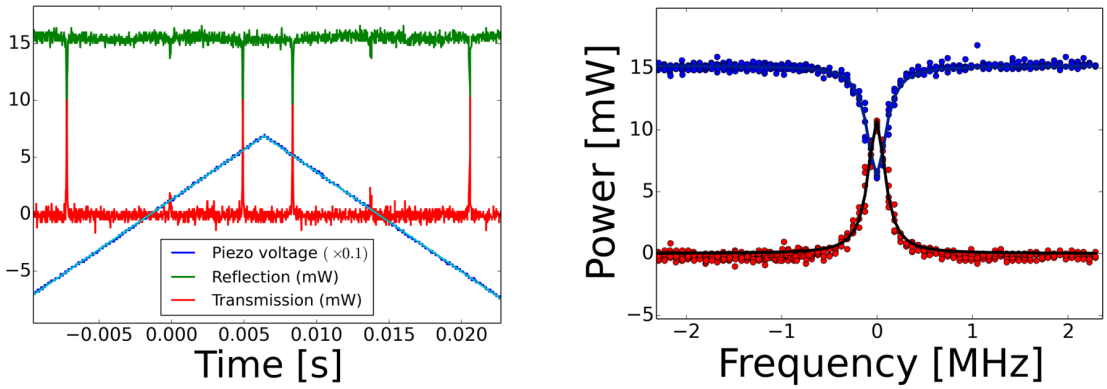

Figure 5.7: Left: Time traces of the reflected power (green), transmitted power (red) and the voltage ramp applied to the PZT (blue). We can see that the mode matching is good with ~ 15 % power coupled into higher order modes. The recorded voltage ramp is fitted to a linear ramp function to calibrate the frequency axis, by noting the voltage change required to scan from one fundamental resonance to another (one FSR = 61 MHz). Right: An expanded view of the transmission and reflection resonances, showing Lorentzian fits with a $\Delta\nu_{\mathrm{FWHM}} = 200$ kHz.

5.2.3 Locking cavity to the laser

The filter cavity is very narrowband and hence the pump laser would drift away from the peak of the resonance. Since we want to maintain maximum power transmission through the cavity to pump the on-chip microrings, we lock the cavity length to the laser to keep it on resonance by actuating on the PZT. The circuit used for locking the cavity transmission to the peak of the resonance is shown in Fig. 5.8 [272]. The PZT is modulated by the oscillator output of a lock-in amplifier at frequencies $\Omega_{\mathrm{mod}}/2\pi = 1 - 20$ kHz. Initial experiments used a Signal Recovery 7265 lock-in amplifier, but recent experiments using the Zurich Instruments MFLI have shown better robustness and stability of the lock. Further improvement in stability could be achieved with a Pound-Drever-Hall lock using the MFLI or the HF2LI as it would tremendously increase the servo bandwidth. The reflected beam

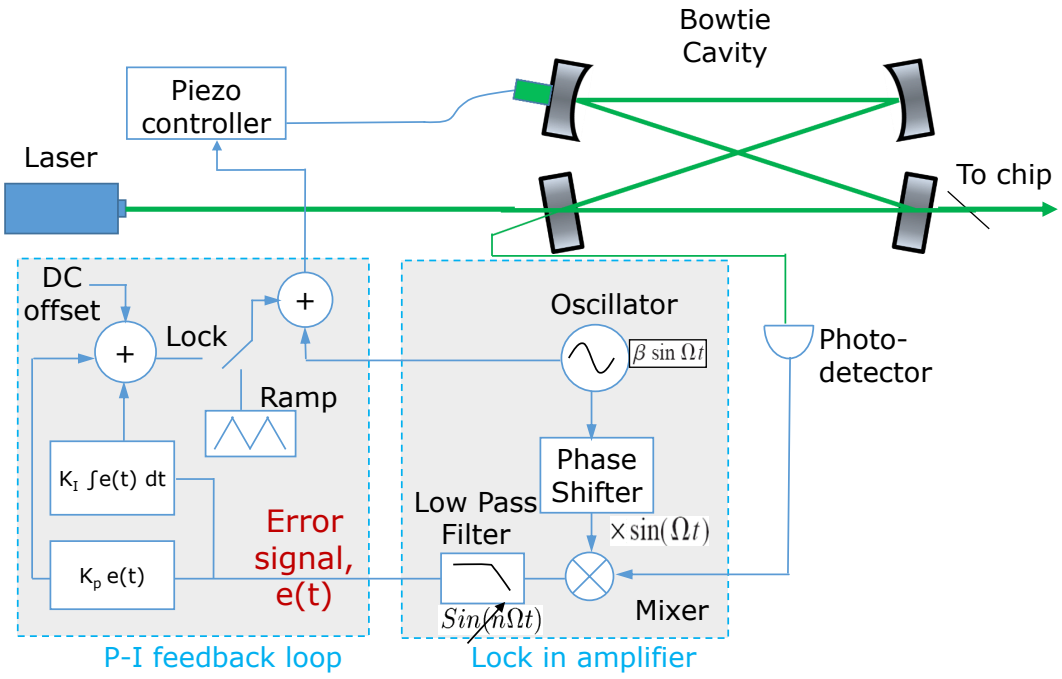

Figure 5.8: Circuit used for dither locking the filter cavity to the laser, consisting of a lock-in amplifier and a proportional-integral (P-I) feedback loop. Initial experiments used the New Focus velocity tunable laser and a Signal Recovery 7265 lock-in amplifier. Improved and more stable locking was achieved by switching to a RIO Orion laser and a Zurich instruments MFLI lock-in amplifier. Green lines: optical paths. Blue lines: electrical signal paths.

from the cavity is monitored on a photodiode. The photocurrent is sent to the lock-in amplifier, where it is demodulated by mixing with a phase shifted version of the modulation signal and low pass filtering to generate the error signal $e(t)$. Initially, a voltage ramp is sent to the PZT in addition to the modulation signal to observe resonances in the reflected optical power. The phase shift of the modulation is controlled to maximize the slope of the error signal as the cavity is scanned across the resonance peak. A typical optimized error signal observed on the oscilloscope is shown in Fig. 5.9. Once the phase shift is optimized, the voltage ramp is switched

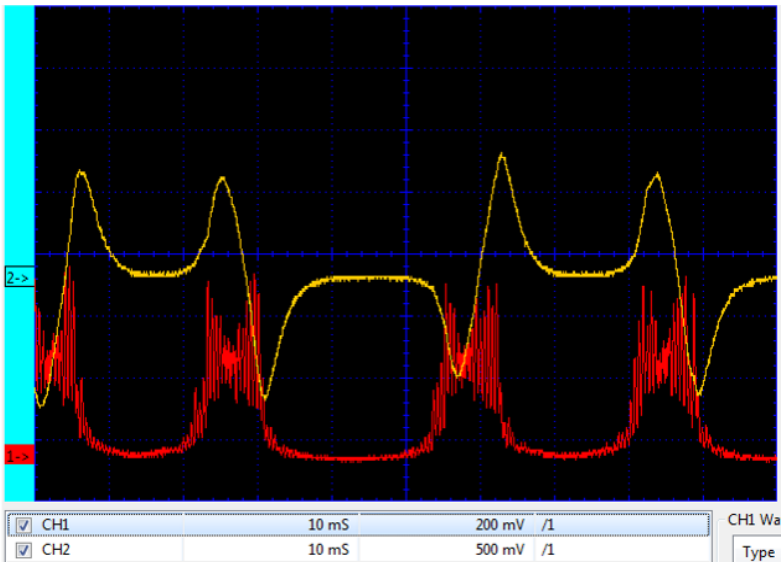

Figure 5.9: Typical error signal observed on an oscilloscope, depicted by the yellow trace. The modulated optical power transmitted through the cavity is shown in red. Modulation frequency: 1.824 kHz. The piezo scanning voltage is not displayed here.

off and the error signal is sent to a proportional-integral (P-I) feedback loop. In our experiments, we used the Newport servo LB1005 to implement the P-I controller. The P-I signal is fed back to the piezo controller to maintain the error signal close to zero and hence keep the cavity resonance locked to the laser frequency. The method used here is termed as dither top-of-fringe locking, since the bandwidth of the feedback system is well below the linewidth of the cavity.

This method of modulation (of the cavity length) and demodulation (of the photodiode signal) is necessary to general an error signal that can discriminate between the two sides of the resonance [272–275]. The transmission or reflection signal is a symmetric Lorentzian about the resonance frequency. When the cavity drifts off resonance, these symmetric signals are not able to discriminate between the two sides since they have the same sign. However, the derivative of the Lorentzian has opposite signs on the two sides of the resonance, and hence it can be used

as a discriminating signal to tell the feedback system in which direction the cavity length should be changed. A small dithering of the cavity length produced by the modulation signal followed by the demodulation of the resulting photocurrent provides us with the required derivative. Mathematically, the modulation produces sidebands at Fourier components Ω about the resonance frequency ω_0. Expanding the photodiode voltage about the resonance frequency,

$$V(\omega_0 + \alpha\cos(\Omega t)) \approx V(\omega_0) + \left.\frac{dV}{d\omega}\right|_{\omega_0} \alpha\cos(\Omega t) \tag{5.5}$$

where α denotes the maximum frequency excursion produced by the modulation and is proportional to the modulation amplitude. Lock-in demodulation picks out the coefficient of $\cos(\Omega t)$, i.e. $\alpha\, dV/d\omega|_{\omega_0}$, which has the desired property of being zero at ω_0 and having opposite signs on the two sides of the resonance. Note that $\Omega/2\pi \ll \Delta\nu_{\mathrm{FWHM}}$ in our experiments, which is conventionally called the dither locking regime. A higher bandwidth lock can be achieved by the Pound-Drever-Hall method ($\Omega/2\pi > \Delta\nu_{\mathrm{FWHM}}$), but that requires feeding back on an actuator that responds faster, such as the laser diode current instead of the cavity PZT.

A few empirical points are worth mentioning here to achieve a stable lock and a good error signal. The scan speed of the voltage ramp should be at least 100 times lower than the modulation frequency to observe clean error signals. Additionally, the modulation amplitude of the oscillator signal might need to be large ($\sim$ 0.01 V at the piezo controller input) when optimizing the error signal, but it should be reduced to $\sim$ 0.002–0.004 V to achieve a stable lock. There is some residual modulation visible after the lock is engaged. While the phase of the error signal is optimized before turning the lock on, one might need to change it by 180 °to produce the correct slope of the discriminating signal for the feedback loop to restore any deviations from resonance. The output time constant of the low pass filter of the lock-in should be chosen to be about twice the inverse of the modulation

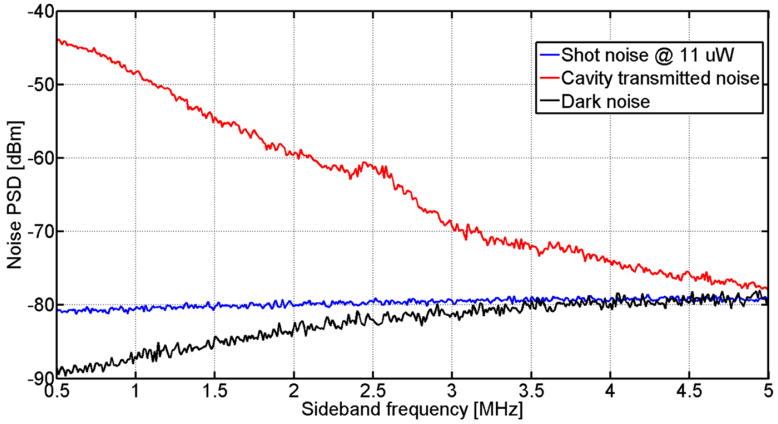

Figure 5.10: Intensity noise characterization of the New Focus velocity laser after transmission through the filter cavity. The large excess noise even after filtering is due to phase to amplitude nosie conversion within the cavity. The phase noise of this tunable external cavity diode laser is bad because of the high frequency jitter.

frequency. A time constant much larger than this results in a low SNR for the error signal along with a phase delay. A small time constant leads to inadequate low pass filtering, and the lock is short lived with residual modulation appearing on the error signal.

5.2.4 Laser amplitude noise after filtering

We next measure the laser amplitude noise after filtering through the narrowband cavity implemented above. First, we lock the cavity to the New Focus velocity laser used in Chapter 3 and record the noise in the transmitted beam using the same method as in the beginning of 5.2. The noise observed on an RF spectrum analyzer is depicted in Fig. 5.10. Surprisingly, we still see significant excess noise in the transmitted beam after the cavity. A word of caution is in order here. We were unable to lock the cavity in a stable and robust fashion to the Velocity laser

due to the frequency jitter. The Velocity laser jitters by approximately 3 MHz over a timescale of 5 ms. Being a tunable external cavity diode laser, the phase noise performance is much worse than, say, single-frequency non-tunable lasers. The large phase noise is converted into amplitude noise by the cavity – we will discuss this phase to amplitude noise conversion in detail later in this chapter.

To overcome the issue of large excess noise, we look for lasers which have inherently a lower noise. Single-frequency non-tunable (or very narrowly tunable) lasers are a natural choice for this purpose. We measured the intensity noise of one such laser, the NP Photonics Rock fiber laser, and observed significant improvement of noise after filtering through the narrowband cavity [Fig. 5.11]. This laser is specified to have an intensity noise peak around 1 MHz. In the bottom panel of Fig. 5.11, we plot the intensity noise before and after the cavity as a function of the optical power incident on the detection system. We see that a noise reduction of more than 25 dB is seen at a sideband frequency of 3 MHz, for an optical power of 50 µW. The black line in this plot is not a fit to the measured data points but an independently calibrated shot noise level. Thus we see that the single frequency fiber laser, after passing through the filter cavity, is shot noise limited to within the precision of our measurement. The shot noise level does not look visibly linear because of the logarithmic scale on the y-axis. The stark difference in the noise performance of widely tunable lasers and non-tunable lasers was observed to be a recurring theme in the work presented in this thesis, both in the quantum optics experiments as well as in frequency comb generation setups. Alternatives to the Velocity such as the widely tunable Tunics Reference laser also suffered from the high noise and jitter issues. In other words, if we have access to electrical or mechanical knobs to change the frequency of the laser, then thermal fluctuations, acoustic vibrations and mechanical disturbances can also perturb the

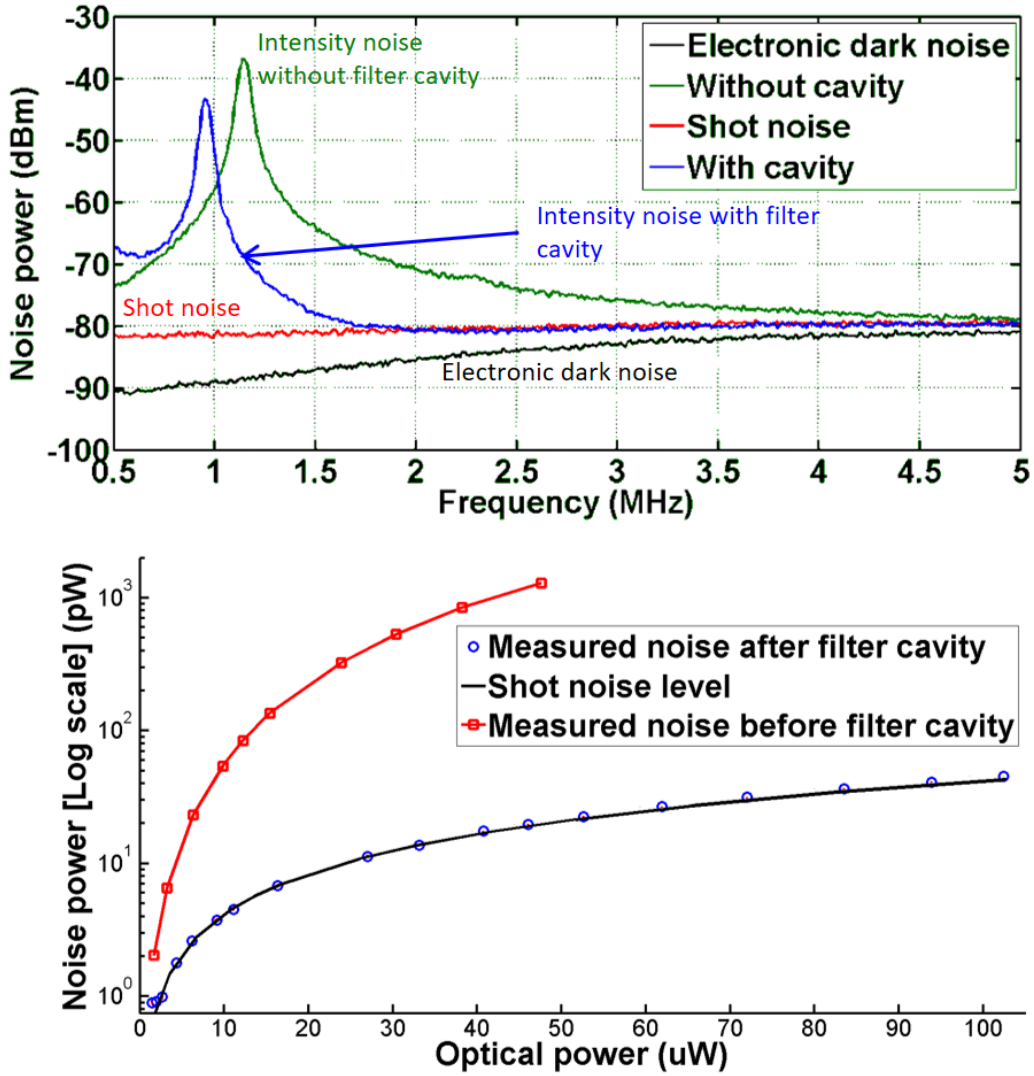

Figure 5.11: Top: The intensity noise level of a single-frequency narrow linewidth laser (NP Photonics Rock @ 1550 nm) before (green) and after (blue) the filter cavity. The intensity noise above 2 MHz drops down to the shot noise level due to the narrowband filtering effect of the cavity. The low frequency noise is higher than that without the cavity due to phase-to-amplitude noise conversion close to the linewidth of the cavity. Bottom: Intensity noise at 3 MHz as a function of the optical power incident on the detection system. The black line is not a fit to the measured blue circles, but an independently calibrated shot noise level. We see a more than 25 dB reduction in excess noise at optical powers of 50 µW, and larger reductions are expected for higher powers. The transmitted beam is shot noise limited for all the powers measured here.

laser through the same knobs, sometimes on much faster timescales, resulting in a higher amplitude and phase noise.

From the experiments of this section, the combination of a single frequency narrow linewidth laser (e.g. the NP Photonics Rock or the RIO Orion) combined with a locked filter cavity is concluded to be a reasonable choice for a pump laser with shot-noise-limited intensity fluctuations.

5.3 Phase noise measurement for phase squeezing and entanglement

Up to this point, we have focused exclusively on intensity noise measurements. To demonstrate entanglement, as well as to further characterize the noise properties of the pump laser, we need a technique that is capable of measuring phase quadrature fluctuations.

The typical method to measure phase noise is homodyne detection, a schematic of which is illustrated in Fig. 5.12. A strong local oscillator beam (LO) is interfered with the weak signal beam to be measured on a 50:50 beam splitter. The LO beam has significantly more power than the signal beam, and can be treated classically. By varying the phase of the LO beam, one can access the fluctuations in any desired quadrature.

A critical aspect of homodyne detection is that the weak beam to be measured and the LO need to be phase coherent with each other. In our FWM source of squeezed light, the signal and and idler modes are separated by 10–40 nm away from the pump. This precludes the possibility of using a part of the pump beam

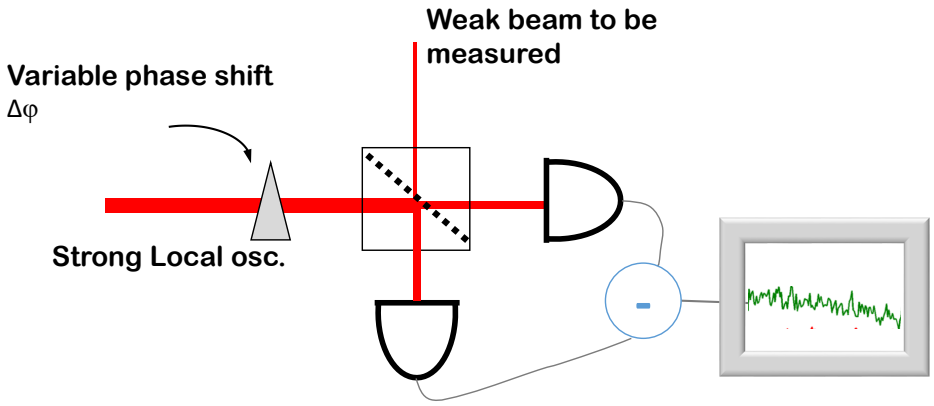

Figure 5.12: Homodyne detection technique for phase-sensitive noise measurement. A strong local oscillator (LO) is mixed with the weak beam to be measured on a 50:50 beam splitter. The two outputs are detected on a balanced detection system. By varying the phase of the LO beam, one can measure any desired quadrature of the weak field. The strong LO can be treated classically here.

or its modulated sidebands as local oscillators.

Since homodyne detection is not an option for quadrature characterization in our scheme, we have to explore other possibilities, some of which include:

1. The use of independent lasers at the signal and idler wavelengths as LOs for homodyne detection at those wavelengths. They would need to be phase locked to the pump beam [276], which is a nontrivial task.
2. An unbalanced Mach-Zehnder interferometer [277]. While this method works very well for bright signal and idler beams, it provides access to the amplitude or phase quadrature, and not to an arbitrary quadrature.
3. Analysis cavities with linewidths less than the measurement frequency [177,

269, 278]. This scheme can provide access to arbitrary quadratures provided that certain conditions on the cavity linewidth are satisfied. Hence, we choose this scheme in our experiments.

The last two methods are in some sense a self-homodyne technique, in that the mean field or the carrier of the signal field itself is used as a LO to measure the quadrature fluctuations at the sideband frequencies, a few MHz away from the carrier. These methods are valid for bright signal and idler field, i.e. those with a nonzero mean field, $a_s \neq 0$.

Method 3 above, which we henceforth refer to as the method of using analysis cavities, uses the core aspect of an interferometer/cavity. An interferometer's primary use is the conversion of phase information into intensity information that can be detected directly by a photodetector. A cavity is an interferometer folded upon itself to enable resonant buildup of power through multiple passes of light, but it still fulfills the purpose of phase-to-amplitude conversion. This finds applications in interferometric phase sensing and cavity enhanced phase detection.

Not surprisingly, an interferometer or a cavity not only transduces the phase of the mean field into intensity information, but also converts the phase *fluctuations* into amplitude fluctuations. An accessible but excellently detailed treatment of this has been provided by Villar [278], and had previously been explored by Galatola *et al.* [279] in the context of squeezed light. Mathematically, let us consider an electric field with the annihilation operator $a(t) = \alpha + \delta a(t)$, where $\langle a(t) \rangle = \alpha = |\alpha| \exp(i\varphi)$, and $\delta a(t)$ represents the small signal fluctuations about the mean value α. For bright beams, $|\alpha| >> |\delta a(t)|$. Using the mean field's phase ϕ as the reference to define the amplitude and phase quadrature fluctuation operators $\delta p(t)$

and $\delta q(t)$ respectively, we have,

$$\delta p(t) = e^{-i\varphi}\delta a(t) + e^{i\varphi}\delta a^*(t), \tag{5.6}$$

$$\delta q(t) = -i[e^{-i\varphi}\delta a(t) - e^{i\varphi}\delta a^*(t)], \tag{5.7}$$

The corresponding frequency components at a sideband frequency ν are then defined by,

$$\delta p(\nu) = \mathrm{e}^{-i\varphi}\delta a(\nu) + \mathrm{e}^{i\varphi}\delta a^*(-\nu), \tag{5.8}$$

$$\delta q(\nu) = -i[\mathrm{e}^{-i\varphi}\delta a(\nu) - \mathrm{e}^{i\varphi}\delta a^*(-\nu)]. \tag{5.9}$$

where we have used the relation that the Fourier transformed component of $\delta a^*(t)$ is $\delta a^*(-\nu)$. These expressions show that the quadrature operators in the frequency domain are linear combinations of the upper and lower sideband frequency components of the field. It is also seen that the amplitude fluctuation operator is in phase with the field whereas the phase fluctuation operator is in quadrature (out of phase by $\pi/2$) with the field. The phase of the mean field or the carrier, φ, determines the phase of the "LO" in this scheme. For instance, if we change $\varphi \to \varphi + \theta$, we end up with,

$$\delta p'(\nu) = \mathrm{e}^{-i(\varphi+\theta)}\delta a(\nu) + \mathrm{e}^{i(\varphi+\theta)}\delta a^*(-\nu), \tag{5.10}$$

$$\delta q'(\nu) = -i[\mathrm{e}^{-i(\varphi+\theta)}\delta a(\nu) - \mathrm{e}^{i(\varphi+\theta)}\delta a^*(-\nu)]. \tag{5.11}$$

In other words, if we change the phase of the carrier φ with respect to the phase of the sidebands, we can access any arbitrary quadrature in the detected "amplitude" quadrature δp, which can be directly measured If $\theta = \pi/2$, $\delta p'$ corresponds to the phase quadrature and $\delta q'$ corresponds to the amplitude quadrature, reversing their initially defined roles. A similar effect happens when the phase of one of the sidebands is changed with respect to the carrier and the other sideband.

The important thing to note is that δp and $\delta p'$ are proportional to the intensity fluctuations which can be obtained from the photocurrent's RF component at a sideband frequency ν.

How do we impart a phase shift to the carrier or to one sideband without affecting the other sideband? We do this with the help of an optical cavity near resonance, whose linewidth is comparable to the RF sideband frequency we are interested in. We call this cavity an "analysis cavity", to distinguish it from the previously discussed filter cavity. In fact, as long as the linewidth is less than $\nu_{\mathrm{RF}}/\sqrt{2}$, one can observe complete conversion of phase to amplitude quadrature fluctuations when the analysis cavity is detuned by $\Delta\nu_{\mathrm{FWHM}}/2$. Following the algebraic treatment in [269, 278], it can be shown that the power spectrum of fluctuations of the reflected beam is related to the input fluctuations by:

$$S_R(\Delta, \nu') = |g_p|^2 \, S_p(\nu') + |g_q|^2 \, S_q(\nu') + |g_{vp}|^2 + |g_{vq}|^2, \tag{5.12}$$

where ν' and Δ are the RF sideband frequency and the analysis cavity detuning normalized to the cavity bandwidth, S_p and S_q are the amplitude and phase quadrature fluctuations of the input beam, and g_p, g_q are coefficients dependent on the cavity detuning whose full expressions can be found in appendix E. g_{vp} and g_{vq} are contributions from vacuum fluctuations entering through spurious losses or nonunity reflectivity of mirrors (except for the input mirror). It turns out that for $\Delta = \pm 0.5$, complete conversion of phase to amplitude fluctuations is observed because $g_p \approx 0$ and $g_q \approx 1$.

The designed cavity is shown in Fig. 5.13. It comprises a flat mirror and a concave mirror (radius of curvature = 60 cm), each mirrors with reflectivities $>$ 99.8% and a flat input coupling mirror with a reflectivity of 98% for s-polarization. The total cavity length is 90 cm, resulting in an FSR of 330 MHz. The finesse is

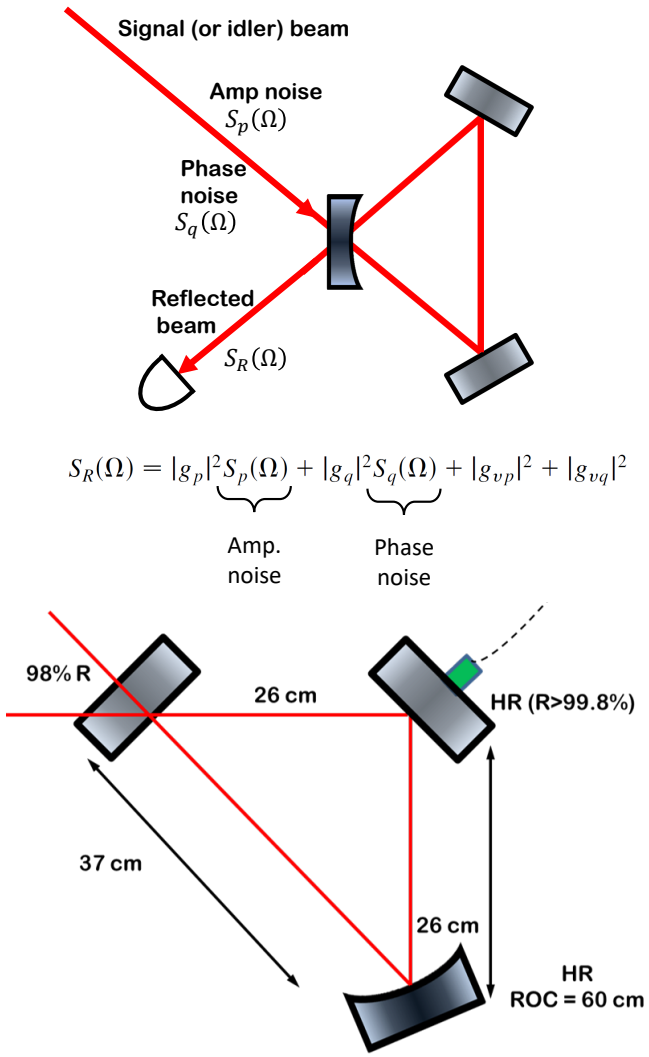

Figure 5.13: Schematic of an analysis cavity that rotates the noise ellipse. The output amplitude fluctuations reflected from the cavity are linear combinations of the input amplitude and phase fluctuations depending on the cavity detuning, and can be used to detect phase quadratures.

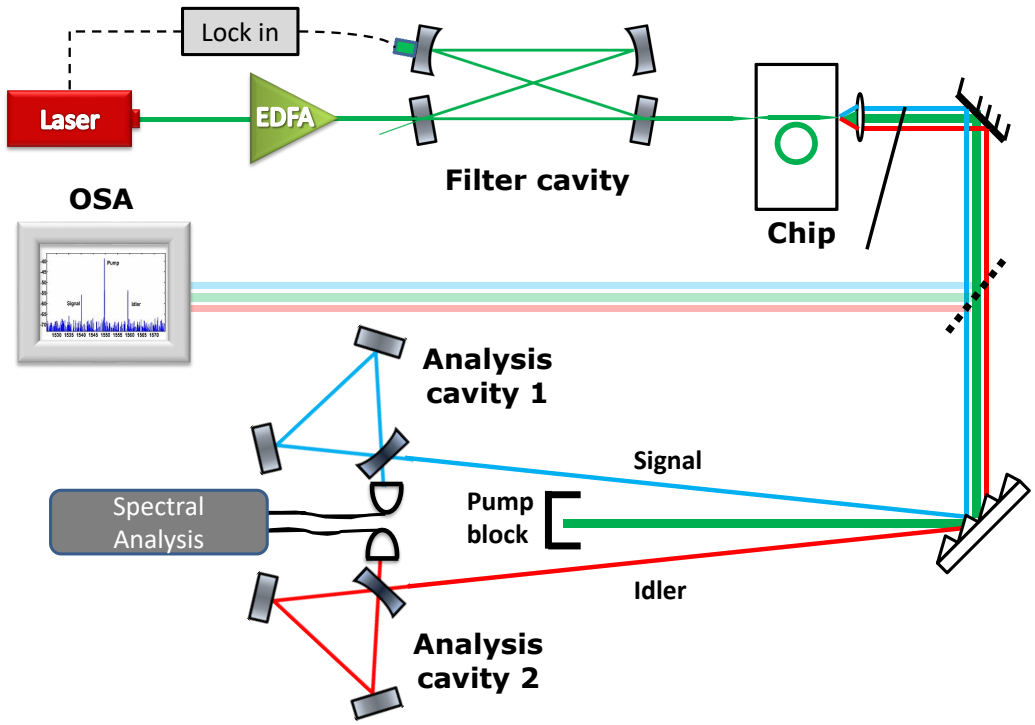

Figure 5.14: Full experimental setup for phase sensitive detection of quadratures of the signal and idler fields. The PZT on the analysis cavities, and the mode-matching and polarization optics are not shown.

230, and the linewidth of the analysis cavity is measured to be 1.4 MHz.

The entire experimental setup including the filter cavity and the analysis cavities is shown in Fig. 5.14.

We have seen evidence of phase noise reduction in the pump beam transmitted through the filter cavity, down to the shot noise level. The quality of lock between the filter cavity and the laser is not sufficiently stable and robust to make reliable measurements. Phase sensitive detection is currently hindered by thermal fluctuations, mechanical vibrations and air currents in the laboratory.

Preliminary experimental data show that the sum of the phase quadratures of the two beams exhibits lower noise than the difference of their phase quadratures, when the microring OPO was pumped with a filtered pump beam. On the other hand, an unfiltered pump beam produced much higher noise for the sum of phase quadratures than the difference, indicating the presence of classically correlated phase noise in the unfiltered beams. Nonetheless, we observe excess noise above the shot noise level for the sum of phase quadratures even for the filtered beam. This can be attributed to multiple reasons. First, the stability of the filtered pump beam in terms of its time-varying amplitude was low, and hence the OPO had to be operated much further above threshold ($> 20\%$) than for intensity-difference measurements. The degree of phase-sum squeezing decreases above the oscillation threshold, unlike intensity-difference squeezing which stays locked to its maximum value above threshold [269]. A more stable operation of the filter cavity would enable phase quadrature measurements closer to threshold, and possibly show evidence of squeezing and consequent entanglement. A second essential factor for the absence of phase-sum squeezing was realized through theoretical calculations performed after the experimental data were acquired – the FWM process causes rotation of quadratures due to self- and cross-phase modulation. The squeezed quadratures are not the sum and difference of the pure amplitude and phase quadratures, but their rotated versions [215]. What this implies is that the unrotated quadratures have excess noise, in accordance with our experimental observations. Careful choice of the relative detunings of the analysis cavities should enable us to access these optimally squeezed quadratures.

5.4 Summary and outlook

We have demonstrated strong shot-noise-limited intensity correlations of 22 dB between asymmetric signal and idler modes produced by nondegenerate FWM. This chapter discussed in detail the characterization of the pump laser noise, which affects measurements of the squeezing level. To mitigate the effects of excess noise in the pump, a filter cavity was designed and inserted between the laser and the chip. A reduction of intensity and phase noise greater than 25 dB was observed in the pump beam after being transmitted through the cavity. A reduction in pump noise paves the way for phase-sum squeezing measurements and a demonstration of on-chip entanglement.

CHAPTER 6

DUAL COMB SPECTROSCOPY

Breaking away from the nonclassical theme of the previous chapters, we will investigate a classical application of nonlinear microresonators in this chapter - that of generating frequency combs. The application of nonlinear microresonators for comb generation has arguably been investigated much more extensively than their quantum applications. With the aim of realizing a promising novel technique that has gained momentum over the last 15 years – dual comb spectroscopy (DCS), we will describe the production of single frequency combs, and then move on to the generation of two frequency combs on the same chip from a single laser. We also show a proof-of-principle demonstration of real-time broadband spectroscopy using the realized dual comb source. Additionally, we study comb formation dynamics using the same technique. Note that the devices used to generate frequency combs are very similar to the ones we used for generating squeezed light, but they are pumped at much higher powers (7-10 dB) above the oscillation threshold. [1]

6.1 Introduction

6.1.1 Frequency combs

Optical frequency combs [260] are a revolutionary technology with widespread applications in precision spectroscopy [280], microwave signal synthesis [281, 282], frequency metrology [283], optical clocks [284], communications [285–287] and astronomical spectrograph calibration [288–292]. A frequency comb consists of a

[1] This chapter has been submitted for peer review

sequence of hundreds or thousands of narrow, discrete spectral lines equidistant in frequency, separated by the repetition rate f_{rep}. First demonstrated around the turn of the century using femtosecond mode-locked lasers [293–295], combs have been miniaturized to the chip scale based on the Kerr nonlinearity using high quality factor (Q) microresonators [35, 53]. The past decade has seen the development of numerous platforms for generating such microresonator-based frequency combs, including silica[47, 296], silicon nitride (Si_3N_4) [208, 254], crystalline fluorides [297–299], Hydex glass [49], aluminum nitride [50], diamond [36], silicon [51] and AlGaAs [52]. These microresonators, when pumped by a monochromatic continuous wave (cw) laser, generate frequency sidebands through four-wave mixing (FWM) parametric oscillation and undergo nonlinear dynamics to produce a comb of frequencies that can span an octave of bandwidth [255, 300].

6.1.2 The technique of dual-comb spectroscopy (DCS)

Dual comb spectroscopy (DCS) is a novel technique that was introduced by Schiller in 2002 [301]. It enables broadband optical sampling of molecular absorption spectra with high signal-to-noise ratio (SNR) and tens-of-µs acquisition times, without any moving parts, through use of the high coherence of the comb lines [301–307]. This technique utilizes two frequency combs with slightly different repetition rates, f_{rep1} and $f_{\text{rep2}} = f_{\text{rep1}} + \Delta f_{\text{rep}}$. The heterodyne beating between these two combs generates a sequence of beat notes in the radio-frequency (RF) domain, spaced by the difference in repetition rates Δf_{rep} , ensuring a one-to-one mapping of the optical comb lines to the RF beat notes. This beating down-converts the spectral information spanning tens to hundreds of THz in the optical domain to a few GHz in the RF domain [Fig. 1]. DCS has been traditionally implemented using

stabilized [304, 305] as well as free running [307, 308] mode-locked Ti:sapphire or fibre lasers and therefore often requires bulky tabletop setups.

6.1.3 Chip-based dual combs

Chip-based frequency combs have the potential to implement DCS in a compact and robust integrated platform. Such combs typically have larger line spacings ($f_{\mathrm{rep}} > 10$ GHz) than their counterparts based on mode-locked lasers. Since $\Delta f_{\mathrm{rep}} \ll f_{\mathrm{rep}}$ to prevent aliasing, a larger repetition rate permits a larger Δf_{rep} , which corresponds to a smaller minimum acquisition time to resolve the beat notes. This enables faster measurements than those possible with laser-based dual combs, especially for spectroscopy in the solid or liquid phase, where materials exhibit broad spectral features. The improvement in speed is in addition to the usual benefits of conventional dual-comb spectrometers, namely, the absence of moving mechanical parts, and the ability to perform absorptive and dispersive measurements with a single photodetector [301]. The dual comb heterodyning technique in microresonators has also been used for massively parallel coherent detection for communications [55].

The challenge in performing DCS using an integrated platform lies in the requirement for mode-locking each of the combs generated in both microcavities and aligning their resonance wavelengths to a single external pump laser wavelength (in order to ensure high relative coherence between the two spectral combs). Two experiments have demonstrated on-chip integration of dual combs using semiconductor disk lasers [309] and quantum cascade lasers [310], with narrow optical bandwidths of 0.08 THz and 0.96 THz, respectively. The development of a dual-comb source based on Kerr nonlinear microresonators, used in combination with

dispersion engineered waveguides, has the potential to increase the bandwidth by orders of magnitude without compromising the device footprint or the on-chip integration capability. Recently, Suh *et al.*[311] demonstrated dual combs based on wedge resonators using two separate chips pumped by two independent lasers, but these combs are limited in their optical bandwidth due to dispersion, and in their achievable relative coherence time without using active locking of the two lasers. Similarly, Yu *et al.* [312] reported mid-infrared DCS using two separate chips pumped by an optical parametric oscillator.

In this chapter, we present for the first time the generation of dual Kerr frequency combs on a single chip, using a single pump laser and dispersion-engineered Si_3N_4 microrings to produce wide optical bandwidths and long coherence times. We demonstrate soliton modelocking of both combs using integrated thermal tuning, leading to narrow microwave beat notes with linewidths < 10 kHz and sech^2 shaped optical spectra spanning 51 THz with minimal mode crossings. Thermal tuning based on platinum microheaters also allows us to use a low-noise non-tunable laser as the pump, resulting in a long mutual coherence time of 100 µs even without active feedback and stabilization. Furthermore, we use one of the soliton mode-locked combs as a reference and investigate the generation dynamics of the second comb as the latter is tuned into the mode-locked state by measuring the intercomb beat note, thus illustrating the power of the dual-comb heterodyne technique to study the formation dynamics of frequency combs. Finally, we perform absorption spectroscopy of dichloromethane in the near-infrared spanning a 170 nm wavelength range, over a fast acquisition time of 20 µs without any averaging, using the demonstrated dual-comb source.

6.2 Generation and characterization of dual combs

6.2.1 Device design

The dual comb is generated using cascaded Si_3N_4 microring resonators pumped with a single cw laser. The cascaded rings (R1 and R2) have slightly different nominal radii of 50.04 µm and 49.98 µm respectively [Fig. 6.1(a)], and are coupled to the same bus waveguide. The waveguides have a height of 730 nm and a width of 1500 nm to ensure low anomalous GVD around the pump wavelength of 1561 nm, which allows for broadband comb generation [53, 255, 300]. The coupling gap between the waveguide and the resonator is 350 nm.

We overcome the challenge of aligning the resonances of both high Q rings (loaded Q > 600,000) to the pump wavelength by fabricating integrated platinum microheaters on top of the Si_3N_4 rings to tune the resonance wavelength of the rings using the thermo-optic effect. This is in contrast to what has been done in most previous experiments with Kerr combs, where the laser wavelength is tuned to a cavity mode of the microresonator [265]. The microheaters have highly localized heat flow, reduced thermal crosstalk [87] and fast response times, and enable us to stably and repeatedly tune the rings into resonance with the pump in tandem [62, 239, 240, 313]. Importantly, the heaters can tune the resonance by more than one full free spectral range (FSR), and hence compensate for fabrication variations in the rings' radius. The rise and fall times of the microheaters are 24 µs and 22 µs respectively, as shown in Chapter 2, which allow us to tune into resonance at speeds of $\sim$ 50 MHz/µs [313]; this is significantly faster than using Peltier elements to tune the temperature of the entire chip.

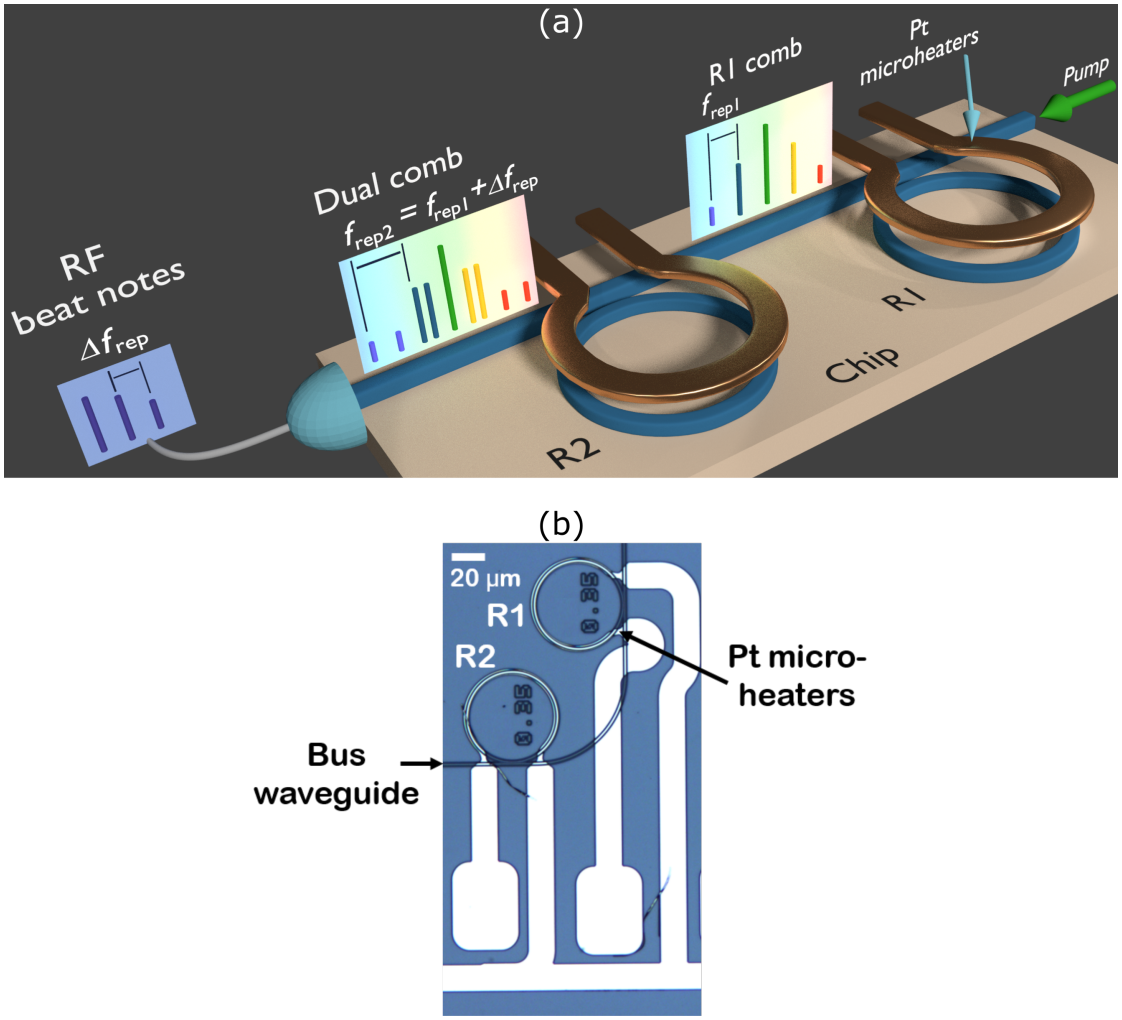

Figure 6.1: **Cascaded microring resonators for dual comb generation.** (a) Schematic of the device. A cw laser pumps the silicon nitride waveguide, which is coupled to two silicon nitride rings, R1 and R2. Through parametric oscillation and cascaded four-wave mixing, rings R1 and R2 generate frequency combs with repetition rates f_{rep1} and f_{rep2} respectively. The insets show schematic optical spectra after the first and second rings. The spectrum detected at the output of the chip using a fast photodiode shows a series of beat notes in the RF domain. Note that while the optical spectrum insets span several tens of THz, the RF spectrum spans only a few GHz enabling ease of detection in the electronic domain. (b) Optical microscope image of the fabricated device showing the silicon nitride rings with integrated platinum microheaters.

6.2.2 Experimental setup

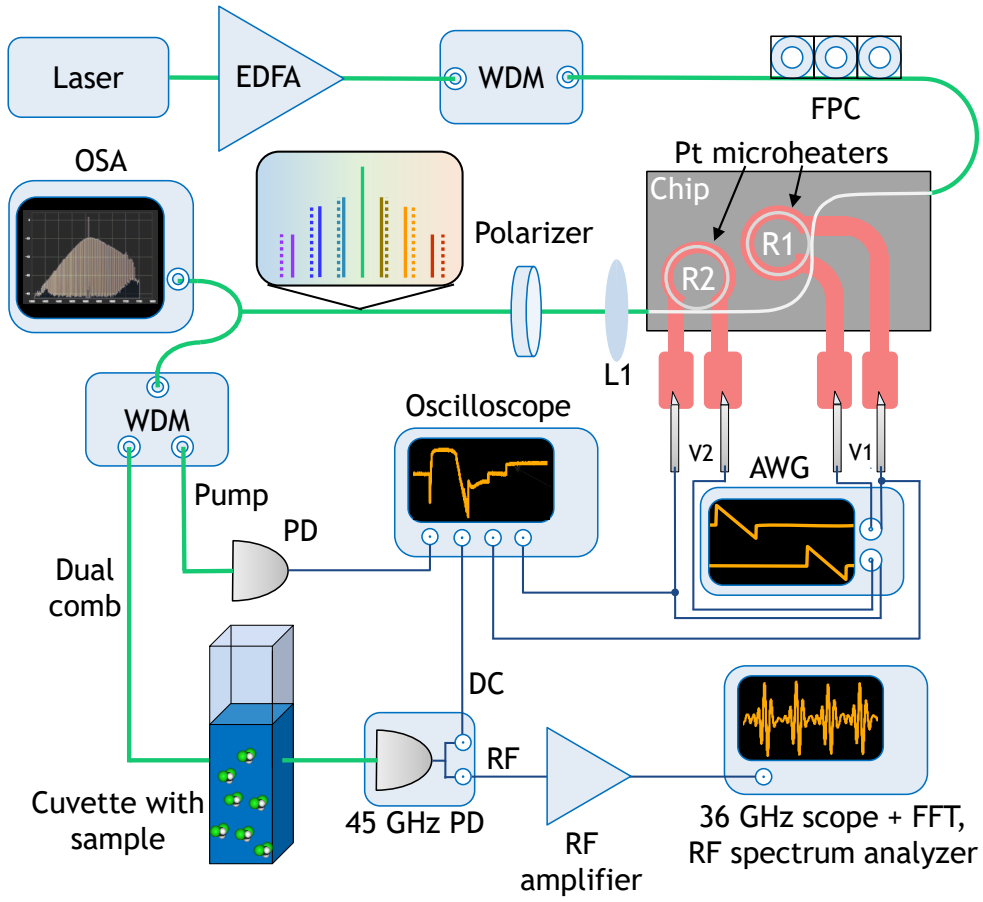

Figure 6.2: **Detailed experimental setup.** EDFA: erbium doped fibre amplifier. WDM: Wavelength division multiplexing filter @ 1561.4 nm, 27.5 GHz 3-dB bandwidth. L1: 40x aspheric lens. FPC: fibre polarization controller. OSA: Optical spectrum analyzer. PD: photodiode. AWG: arbitrary waveform generator. V1 and V2 are voltages applied to the microheaters on rings R1 and R2.

A continuous wave (cw) RIO Orion laser at 1561.4 nm with a narrow linewidth of < 3 kHz is used as the pump. It is amplified by an erbium doped fibre amplifier (EDFA) and filtered by a 27.5 GHz bandwidth DWDM add-drop filter centered at 1561.42 nm to mitigate the amplified spontaneous emission noise generated by the EDFA. The phase noise is specified at 50 µrad $\mathrm{Hz}^{-1/2}$ m^{-1} at 10 Hz offset and 1.5 µrad $\mathrm{Hz}^{-1/2}$ m^{-1} at 10 kHz offset, normalized to a 1-m path

difference. The output power was 21 mW. We attenuated the laser output by 10 dB before sending it to the EDFA. The EDFA had a noise figure of 4.8 dB (@-6 dBm input power) and was operated to output $\sim$ 300 mW. A fiber polarization controller (FPC) before the chip and a polarizer after the chip are used to couple to the fundamental transverse electric (TE) mode of the bus waveguide using a lensed fibre. The waveguide is coupled to rings R1 and R2, which have platinum microheaters on them to enable thermal tuning of the rings' resonance wavelength using the thermo-optic effect. Light is coupled out of the chip using a 40x aspheric lens. The microheaters are driven using tungsten probes by an arbitrary waveform generator (AWG) in burst mode, with a staggered delay of 0.85 ms between the burst triggers of the two voltages V1 and V2 applied to the heaters on rings R1 and R2 respectively. On coupling 110 mW of power into the bus waveguide and applying the requisite voltages to the rings (shown in Fig. 6.3(e)), soliton mode-locked dual combs are generated. A part of the output of the chip is sent to an optical spectrum analyzer (OSA) to monitor comb formation. The rest is sent to another DWDM add-drop filter to separate the pump and the dual comb. The pump and the generated dual comb are both sent to separate photodiodes and the DC component is monitored on an oscilloscope. The dual comb is also sent to a 45 GHz fast photodiode (Newport 1014) which had a rise time of 9 ps, a responsivity of 0.45 A/W and a noise-equivalent power of 45 pW $\mathrm{Hz}^{-1/2}$. For dual-comb spectroscopy, a cuvette with a path length of 10 mm, containing the sample to be measured (dichloromethane in our experiment) is placed in the path of the dual comb. The RF output of the fast photodiode is amplified using a three stage broadband amplifier (Centellax OA4MVM3) with a bandwidth of 40 GHz and sent to a 36 GHz oscilloscope (LeCroy LabMaster 10 Zi-A, 8-bit resolution, 80 GSa/s). The amplifier had a gain of $\sim$ 27 dB and an rms timing jitter of 0.5 ps. A time

domain trace of the dual-comb multiheterodyne beating is acquired, followed by a fast Fourier transform (FFT) to obtain the RF beat notes. The fast oscilloscope can also be used as an RF spectrum analyzer for measuring the linewidth of the beat notes.

6.2.3 Single and dual comb generation

The heaters enable tuning of either one or both rings into resonance to generate frequency comb spectra spanning 51 THz (400 nm) near the pump wavelength of 1561.4 nm, as shown in Fig. 6.3(a)-(c). We excite ring R1 with $\sim$ 105 mW of power in the bus waveguide and tune its heater without tuning the heater on R2 to generate the spectrum shown in Fig. 6.3(a). Similarly, Fig. 6.3(b) shows the spectrum obtained by tuning the heater on R2 without tuning the heater on R1. These individual comb spectra allow us to characterize the mode spacings of the combs to within the 0.01 nm resolution of the optical spectrum analyzer (OSA). Both rings generate a spectrum spanning 400 nm (51 THz). We infer a mode spacing $f_{\mathrm{rep1}} = 451.4 \pm 0.4$ GHz for the R1 comb and $f_{\mathrm{rep2}} = 452.8 \pm 0.4$ GHz for the R2 comb. The difference between the mode spacings of the combs is $\Delta f_{\mathrm{rep}} = 1.4 \pm 0.8$ GHz, which is well within the bandwidth of commercially available fast photodiodes, whereas the repetition rate frequency of each individual comb is much larger than what can be directly detected with fast photodiodes. This is true in general for microresonator combs, which have repetition rates from tens to hundreds of GHz. Thus, the dual comb technique frequency downconverts the repetition rate of microresonator combs making it amenable to study the repetition rate beat note using fast photodiodes. Note that the large error bar in Δf_{rep} is limited by the resolution of the OSA, and RF heterodyne beating measurements

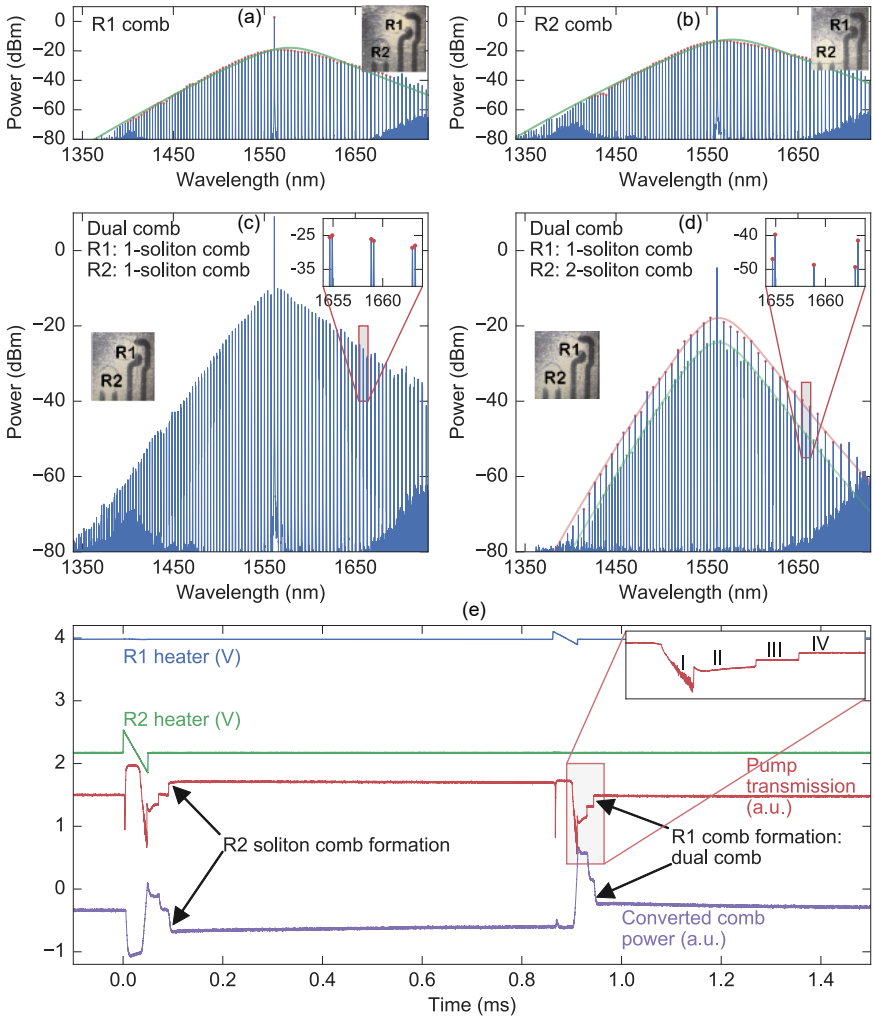

Figure 6.3: **Optical spectra of the generated combs. (a)-(c)** Generated spectrum when the heaters on (a) R1, (b) R2 and (c) both rings are tuned to resonance with the laser. The OSA resolution was set to 0.01 nm. The insets show top-view infrared CCD camera images showing which of the two rings are on resonance with the laser. The waveguide has been false colored for clarity. The generated combs are in the single-soliton mode-locked state. The solid red and green lines are fits to a sech^2 spectral envelope. The zoom-in inset in (c) and (d) also reveals the dual comb with pairs of lines closely spaced in wavelength. **(d)** A dual-comb state with a single soliton in R1 and two solitons in R2. By changing the magnitude of the final upward voltage ramp shown in (e), one can choose the number of solitons in the final mode-locked state. As an example, the state shown here has a single soliton in R1 and two solitons half a roundtrip apart in R2 (harmonic mode-locking). **(e)** Time domain traces of the voltage ramp used to access the mode-locked states of both the rings. The blue (green) line represents the voltage applied to the heater on R1 (R2). The purple line represents the converted comb power (excluding the pump), vertically offset for clarity. The inset shows the distinct stages of comb formation in R1, including the high-noise state (I), multi-soliton states (II and III) and the single soliton state (IV).

shown later determine Δf_{rep} to a much higher accuracy. Fig. 6.3(c) shows the spectrum of the dual comb generated when both R1 and R2 are on resonance with the laser. As can be seen from the inset of Fig. 6.3(c), pairs of closely spaced modes are clearly distinguishable, indicating a dual comb spectrum. It is worth noting that Δf_{rep} is much larger than the linewidth of each cavity mode (230 MHz for R1, 310 MHz for R2), so that the comb lines generated in R1 are not resonant with the cavity modes of R2, except for the pump. This ensures that the comb lines from R1 do not couple into the R2 resonances and interact with the comb lines in R2, despite the cascaded geometry.

6.2.4 Beat note spacing

The beat note spacing between the combs generated in rings R1 and R2 is theoretically determined by the difference in the radius of the two rings as well as the electrical power delivered to the microheaters. The rings were designed to have radii of 49.98 µm and 50.04 µm, which corresponds to an inherent nominal difference in their free spectral range (FSR) of 540 MHz. The heaters on R1 and R2 were driven with average powers of 94 mW and 30 mW respectively to make them resonant with the pump in tandem, which is responsible for a larger $\Delta f_{\text{rep}} = 1.12$ GHz, as we will see later.

It is important to note that $\Delta f_{\text{rep}} = 1.12$ GHz is larger than the cavity linewidth ($\sim$230 MHz for R1, 310 MHz for R2, see Fig. 6.4), hence the comb lines generated in R1 do not resonantly couple into the longitudinal cavity modes of R2. Avoiding this coupling is essential to generate two separate combs with slightly different repetition rates, and prevent feeding of the second ring by the first comb. The rings are tuned such that the pump is the only wavelength that resonantly couples

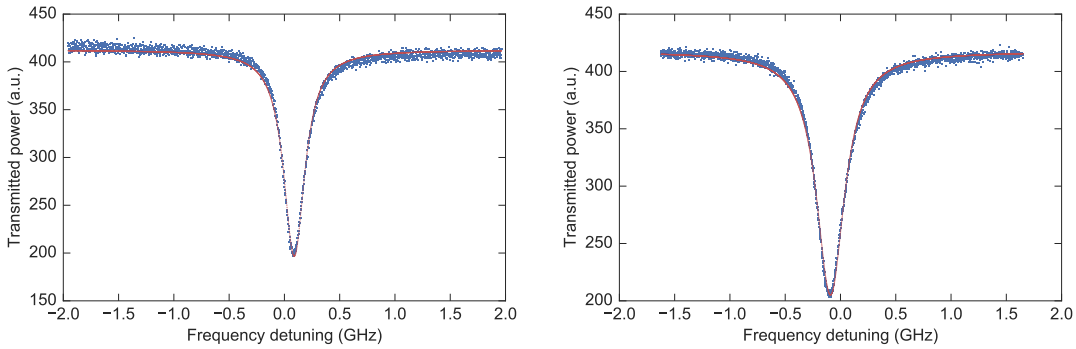

Figure 6.4: **Quality factor of microrings.** The full width at half maximum (FWHM) of the resonance estimated from the Lorentzian fit to the transmitted optical power is 230 MHz for R1 (left) and 310 MHz for R2 (right). This corresponds to loaded quality factors of 830,000 and 620,000 respectively. The power in the bus waveguide off resonance was approximately 20 µW for this measurement. Note that the FWHM is smaller than the beat note spacing of 1.12 GHz.

to both rings. Smaller beat note spacings $\Delta f_{\mathrm{rep}} < 100$ MHz should be achievable using a parallel geometry instead of the cascaded or series geometry for the rings. In other words, the rings could be coupled to two separated bus waveguides, thus eliminating the possibility of the lines of the first comb feeding into the second ring. The loaded Q of the rings is 830,000 for R1 and 620,000 for R2. The rings are overcoupled, and the corresponding intrinsic Q is estimated to be $Q_{\mathrm{i,R1}} \sim 5.7 \times 10^6$ and $Q_{\mathrm{i,R2}} \sim 4.2 \times 10^6$ respectively. Significantly higher Q's up to 3.6×10^7 have recently been reported using improved fabrication techniques such as chemical mechanical planarisation, etching with reduced sidewall roughness, and multipass lithography [77]. Silicon nitride microrings fabricated with these improved techniques would enable a smaller beat note spacing even with a cascaded geometry since they would have an order of magnitude reduction in the resonance linewidths over the devices used in this work.

6.2.5 Soliton modelocking

The difficulty in experimentally accessing the mode-locked regime of Kerr combs lies in the thermal shift of the resonance, which occurs on much slower timescales than the Kerr-nonlinear response. Tuning the rings into resonance with the pump at a slow speed typically leads to the formation of high-noise combs with multiple broad RF beat notes [212, 264, 300]. This can be explained by the fact that the high noise state exists on the blue-detuned side of the resonance, where thermal shifts make the comb self-stable [314]. In the blue-detuned regime, when a random increase in the intracavity power causes the ring resonance to thermo-optically redshift, the detuning increases, leading to a decrease in the intracavity power. This in turn reduces the intracavity power. Such a negative thermal feedback mechanism ensures that the ring always remains blue detuned on resonance. Low-noise mode-locked states exist on the red-detuned side of the resonance, which by itself is thermally unstable. These mode-locked states, which correspond to temporal dissipative Kerr cavity solitons propagating in the microresonator, can be stably accessed by tuning into the red-detuned side of the resonance at an appropriate speed, so that the soliton state is reached when the cavity is close to its equilibrium temperature [265, 313].

By engineering the thermal tuning of the heaters with respect to the comb, we independently tune the two rings at sufficiently fast timescales and achieve modelocking of the two spectral combs using a fixed-frequency pump laser. The combs generated in R1 and R2 exhibit single-soliton modelocking with sech^2-spectral envelopes without significant mode crossings. We tune into the low-noise mode-locked states of both the combs by applying a voltage ramp to the microheaters of rings R1 and R2 over a period of 50 µs using an arbitrary waveform generator, corre-

sponding to a scan speed of 20 kHz as shown in Fig. 6.3(e), and as detailed in Ref. [313]. The corresponding rate of change of the ring's resonance frequency is estimated to be $\sim$ 50 MHz per µs. The downward voltage ramp is applied on a ring when the pump laser is initially on the blue-detuned side of the ring resonance which blueshifts the ring resonance towards the pump laser. A final increase in voltage redshifts the resonance, providing us deterministic access to the soliton states. When the pump wavelength is on the red-detuned side of the resonance, we observe a series of abrupt steps in the pump transmission concomitant to the formation of multi-soliton states with different numbers of solitons propagating per roundtrip around the microring, similar to what has been routinely observed in recent work on soliton modelocking [206, 265, 313]. Optimization of the voltage ramp parameters permits us to reach the same mode-locked state for single frequency combs on each microheater scan. Dual comb generation, while successful on each scan, occasionally requires multiple scans to reach a desired soliton state due to the influence of R1's transmitted pump on R2. By controlling the magnitude of the final upward voltage ramp, one can control the number of solitons present in the comb. For example, Fig. 6.3(d) depicts a spectrum with a single soliton state in R1 and a two-soliton harmonic mode-locked state in R2. Note that recent experiments have demonstrated soliton modelocking in fibre ring resonators [315], as well as in single microresonators using pump wavelength tuning [265], two-step pump power control [206, 316] and integrated thermal tuning[313]. Here we choose thermal tuning since it allows us to use a fixed-frequency non-tunable low-noise laser[249] (RIO Orion, linewidth $<$ 3 kHz) as the pump and enables independent tuning of the two rings at sufficiently high speeds. Tunable external cavity diode lasers, conventionally used for Kerr frequency comb generation, have a broader linewidth ($>$ 100 kHz), have higher phase noise and frequency jitter,

and are typically not amenable to tuning at the required speeds. It is important to note that the soliton states, once generated, stably exist for hours without any active feedback, in spite of the drifts in fiber-to-chip coupling and pump power.

6.2.6 Multiheterodyne RF beat notes

We observe multi-heterodyne beat notes between the combs when both rings are tuned into resonance with the pump laser to generate dual combs. For this measurement, the output of the chip is sent to a wavelength-division multiplexing (WDM) filter to remove the pump. Since the comb lines are symmetric in frequency relative to the pump, the beat notes of the comb lines on the red side of the pump are downmixed to the same RF frequency as the beat notes from the blue detuned side. To avoid this and hence enable one-to-one mapping of the RF beat notes to the optical wavelength, we use short and long pass filters to characterize the beat notes on the shorter and longer wavelength sides of the dual comb. In principle, an acousto-optic modulator (AOM) can be used to frequency shift a portion of the pump [305, 317–321] and make the two resonators align to the two different wavelengths, which would alleviate the need for filtering the comb. It is worth noting that optical filtering is routinely used to improve the SNR and prevent aliasing in dual comb spectroscopy [306, 317].. The filtered comb is sent to a 45 GHz photodiode followed by a 40 GHz RF amplifier, and the resulting RF signal is monitored on a 36 GHz real-time oscilloscope. In Fig. 6.5(a) we plot the time-domain interferogram over 20 µs. Fig. 6.5(b) shows the same interferogram expanded 2000 times, and a periodic signal is clearly visible repeating every 900 ps ($=1/\Delta f_{\mathrm{rep}}$). To further elucidate the details of the time domain interferogram, we amplify the filtered dual comb using an L-band EDFA and plot the amplified

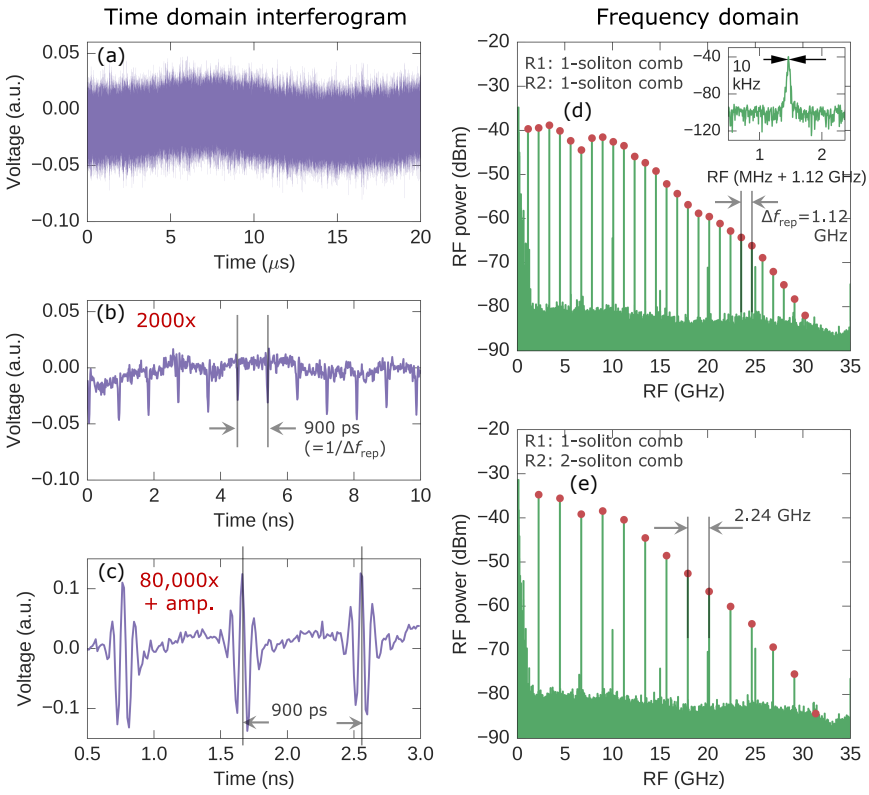

Figure 6.5: **Time domain interferogram and RF heterodyne beat notes. (a)** 20 µs interferogram of the mode-locked dual comb acquired with a fast photodiode and a 36 GHz oscilloscope. **(b)** The same interferogram expanded 2000 times shows periodic pulses at the inverse of the beat note frequency ($1/\Delta f_{\text{rep}}$). Note the different scale on the x-axis compared to (a). **(c)** The dual comb is amplified by an L-band EDFA and detected to highlight features of the interferogram. This trace is zoomed in by a factor of 80,000 compared to (a). **(d)** RF multi-heterodyne beat notes obtained by a fast Fourier transform (FFT) on the interferogram in (a). The data reported here was taken with a long pass filter and represents the dual comb lines on the red side of the pump. The beat notes correspond to the dual comb shown in Fig. 6.3(c). A beat note spacing of 1.12 GHz is observed. The inset shows the linewidth of the first beat note, measured with an RF spectrum analyzer with a resolution bandwidth of 2 kHz. We measure a high SNR (60 dB) with a linewidth of 10 kHz, which corresponds to a relative coherence time of 100 µs. **(e)** RF beat notes of the comb shown in Fig. 6.3(d). The beat notes are spaced by 2.24 GHz as the R2 comb is missing a line in every alternate mode of the ring. In both (d) and (e), the beat notes close to the pump have a high SNR (> 40 dB). The spurious peaks at 5, 10, 15, 20 and 25 GHz are artefacts of the FFT analyzer.

and expanded version of the interferogram in Fig. 6.5(c). A fast Fourier transform (FFT) of the time domain signal yields 27 RF beat notes spaced by 1.12 GHz, which corresponds to the difference in mode spacings of the two combs [Fig. 6.5(d)]. The number of beat notes detected is limited by the noise floor of the FFT and the decreasing power in the comb lines away from the pump. The beat notes below 10 GHz have very high SNR in excess of 40 dB. The center frequency of the first beat note is 1.12 GHz, which is commensurate with the difference in mode spacings estimated from the OSA scans within the uncertainty of the OSA measurement. It also matches reasonably well with the difference in mode spacings calculated based on the radii of R1 and R2 (see Supplementary Information section II).

The soliton mode-locked dual comb exhibits low-noise RF beat notes with a narrow 3-dB linewidth of 10 kHz [Fig. 6.5(d)], which ensures a long relative coherence time [$\tau_{\text{rel}} = (10\text{kHz})^{-1} = 100$ µs]. The first beat note has an SNR exceeding 60 dB over a span of 2 MHz with a sweep time of 500 µs. Our high SNR over fast acquisition times is enabled by (i) a short single-shot acquisition time (limited by $\tau_{\text{acq,min}} = 2/\Delta f_{\text{rep}} = 1.79$ ns to resolve individual beat notes), and (ii) our ability to perform complete spectral acquisitions well within the relative coherence time $\tau_{\text{rel}} = 100$ µs. We choose an acquisition time $\tau_{\text{rel}} = 20$ µs to satisfy the condition $\tau_{\text{acq,min}} < \tau_{\text{acq}} < \tau_{\text{rel}}$. Note that the relative coherence between the two mode-locked combs is high even though the combs are in the free-running state (i.e. there is no active feedback and stabilization) since both the combs are generated from the same low-noise pump laser. The observed beat note linewidth of 10 kHz is not fundamental but is limited by the noise in the arbitrary waveform generator used to control the heaters on the rings. Shorter linewidths (< 1 kHz) at the repetition rate beat note have been reported for single combs without active feedback[57,

204, 265], and hence it should be possible to reach even longer coherence times using a lower noise voltage source to control the heaters.

6.3 Applications of dual combs

6.3.1 Comb formation dynamics

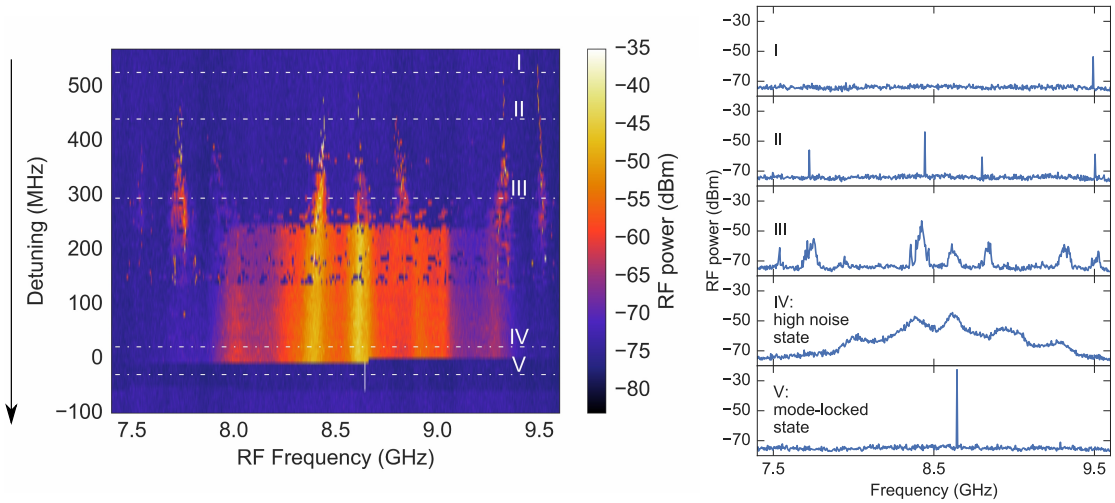

Figure 6.6: **Dual-comb heterodyne technique to study beat note evolution.** The device used in this measurement had a beat note spacing of 8.6 GHz. Keeping the comb generated in R1 in the mode-locked state, the resonance of R2 is tuned with respect to the pump laser and the RF spectrum is recorded. The left panel shows the spectrum of the first beat note as the heater power on R2 is varied starting from a far-blue-detuned state to the mode-locked state on the red detuned side. The spectra on the right show the formation of beat notes (Stage I and II), which broaden to form a wide beat note in the high noise state (Stage III and IV). On tuning further to the red-detuned side, we observe an abrupt transition to a narrow and high-SNR beat note as shown in Fig. 6.5.

We show that the integrated dual comb source enables one to directly observe

the comb formation dynamics without the need for a secondary laser or microwave oscillator. A microresonator frequency comb starts as primary sidebands which develop into minicombs, which further evolve into a high-noise state and finally undergoes a transition to a mode-locked state through higher-order FWM interactions[57, 204, 265, 322]. Such dynamics have been studied experimentally by characterizing the repetition rate beat note, but that often requires auxiliary lasers or RF local oscillators for heterodyne downmixing [204, 212]. Here we use the dual comb heterodyne technique for the same purpose, obviating the need for an auxiliary laser.

We monitor the evolution of the RF noise of the comb from R2 as it is tuned into the soliton mode-locked state, by beating it with a mode-locked comb from R1. Specifically, here we study the beat note around the radiofrequency Δf_{rep} , formed by the mixing of the first R2 comb line on the red side of the pump and the corresponding comb line in R1, the latter acting as the local oscillator. We can choose a different radiofrequency ($= n\Delta f_{\mathrm{rep}}$) to study the evolution of a comb line n FSRs away from the pump. The rings used in this measurement have a difference in radius of 1 µm, corresponding to an 8.6 GHz beat note spacing. The larger beat note spacing allows us to study the noise characteristics of combs, which typically span up to several GHz in the high noise state. We used a long pass filter to observe the comb on the red side of the pump. A voltage ramp is applied initially to the heater on R1, as described in the previous section, to generate a soliton mode-locked comb, which is then used as a reference to probe the different stages of comb formation in R2. The voltage applied to the heater on R2 is changed and the RF spectrum around the first heterodyne beat note at 8.6 GHz is simultaneously recorded. Fig. 6.6 shows the evolution of the beat note as R2 goes through several stages of comb formation, finally culminating in the

narrow, high-SNR beat note characteristic of dual mode-locked combs described in the previous section. On the blue-detuned side, a single (state I) or multiple (state II) low-SNR beat notes are observed. With further tuning, the number of beat notes as well as the width of each beat note increases, eventually leading to the broad RF beat note characteristic of the high-noise state (stage III and IV). By continuing the scan, we access the red-detuned side of the resonance, resulting in the formation of a high-SNR narrow beat note. Further continuous scanning in the same direction leads to the ring falling out of resonance with the laser. The RF spectra in Fig. 6.6 do not include the dynamics of the primary comb lines, as they are formed several FSRs away from the pump at larger blue detunings than what is shown here. Note that since there is a one-to-one mapping between each pair of closely spaced lines of the dual comb and the corresponding beat note in the downmixed RF spectrum, one can in principle study the dynamics of the comb line-by-line by experimentally analyzing the desired RF heterodyne beat note.

To underscore the importance of modelocking for the generation of narrow beat notes, we also study the dual comb in the high-noise state which exhibits a much broader beat note 3-dB linewidth. The linewidth of the dual comb beat note in this state is $\sim$ 300 MHz, which is rather broad for precision spectroscopy or microwave signal generation. This is because in the high RF-amplitude noise state, the frequencies and the relative phases of the comb lines randomly fluctuate in time.

We show the optical and RF spectra of non-modelocked combs in this section. Fig. 6.7 depicts the mesa-shaped optical spectrum typically seen in combs in the high-noise state, as has been reported earlier[265, 313].

In Fig. 6.8 we show the evolution of the first RF beat note at 8.6 GHz, using

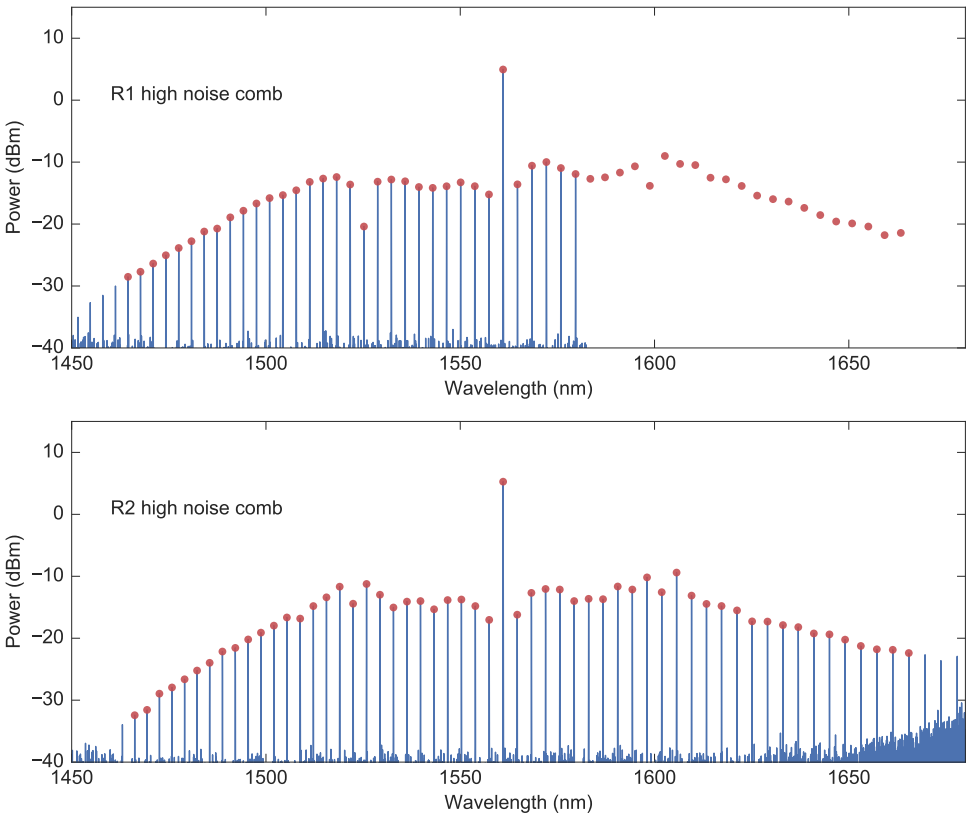

Figure 6.7: **Optical spectra of combs in the high noise state.** The combs generated in R1 and R2 show a mesa-shaped spectrum. The device used here is the same as in Fig. 4, and had a $\Delta f_{\text{rep}} =$ 8.6 GHz.

the same device studied in Fig. 6.6. The difference is that the comb generated in R1 is not mode-locked, but in the high-noise state, while R2 is tuned into a resonance. The features observed on the blue-detuned side of the resonance are qualitatively similar to those observed when the R1 comb is mode-locked. On the other hand, the narrow high-SNR beat note is not observed on the red-detuned side of the comb. This proves that the narrow intercomb beat note is only observed when both the combs are in the mode-locked state.

The linewidth of the beat note not only determines the relative coherence time of the two combs, but also limits the minimum beat note spacing that is permitted

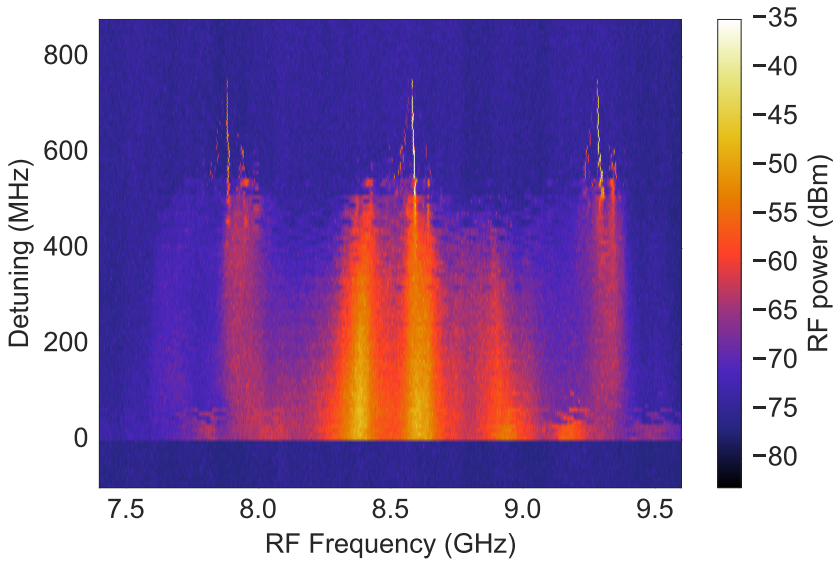

Figure 6.8: **Evolution of dual-comb beat note when the R1 comb is in the high-noise state.** Comparing with Fig. 6.6, we notice that the narrow high SNR beat note is absent on the red detuned side of the resonance. Hence, mode-locking both the combs is essential to observe the high SNR narrow beat note between the two combs of the dual comb. The device used here is the same as in Fig. 4, and had a $\Delta f_{\mathrm{rep}} = 8.6$ GHz.

for them to be individually resolvable. The narrower the linewidth of the beat note, the higher the permissible compression ratio from the optical to the RF domain ($f_{\mathrm{rep}}/\Delta f_{\mathrm{rep}}$). It is thus important to operate both the combs in the mode-locked state.

6.3.2 Spectroscopy

We perform liquid phase absorption spectroscopy of dichloromethane near the pump wavelength of 1561 nm using the dual comb source and show that the recorded spectrum using DCS agrees very well with the corresponding spectrum obtai-

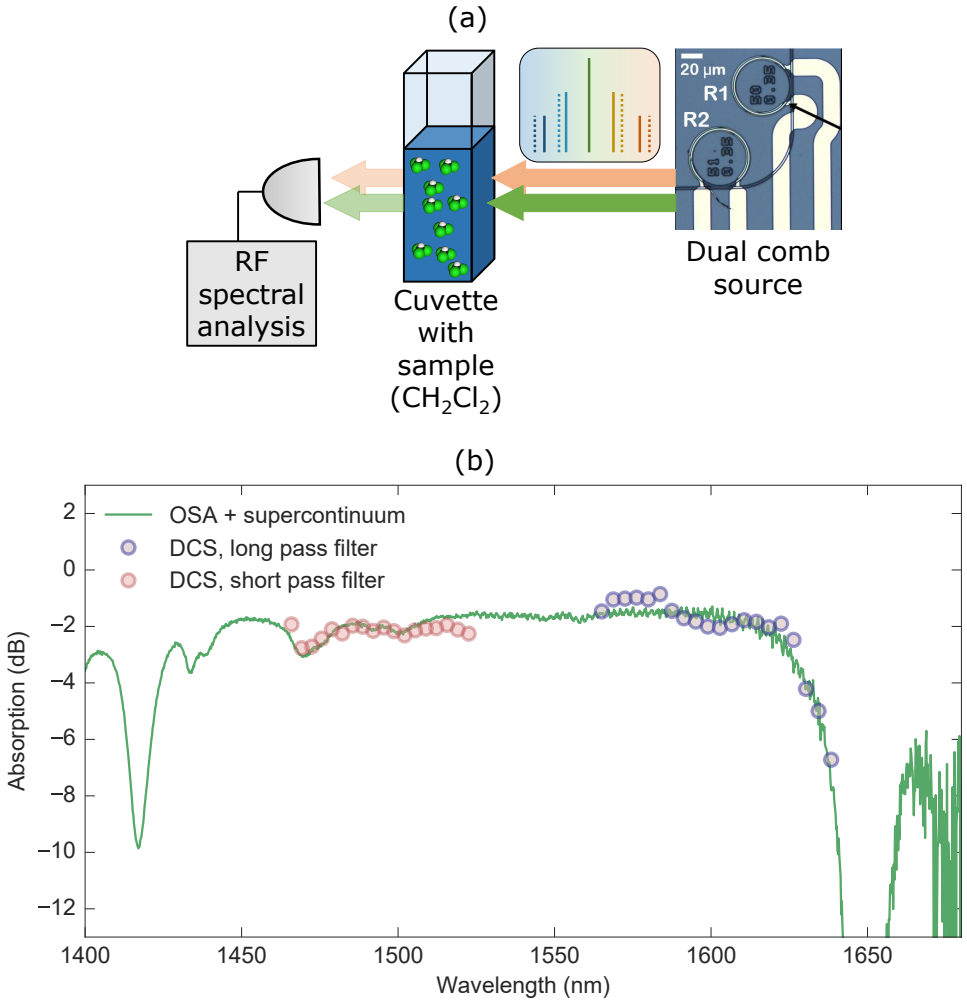

Figure 6.9: **Dual comb spectroscopy of dichloromethane. (a)** Schematic of the setup. The output of the chip generating a dual comb is sent to a 10 mm cuvette containing dichloromethane, and the transmitted light is sent to a 45 GHz photodiode and analyzed with an RF spectrum analyzer or with a fast oscilloscope. **(b)** Spectrum of dichloromethane acquired using DCS and corroborated with the same spectrum measured with a broadband supercontinuum source and an OSA. The solid line represents the absorption spectrum measured with a supercontinuum source (Fianium SC-450-4) and an OSA. The red (blue) circles represent the absorption spectrum acquired using the RF beat notes and a short pass (long pass) filter. All spectra are normalized by the corresponding spectrum without dichloromethane.

ned using an OSA and a broadband supercontinuum (Fianium SC-450-4) as a light source. Dichloromethane is a widely used organic solvent with broad absorption features in the near-IR. For spectroscopy, the output of the chip is collected with an aspheric lens and sent directly through a cuvette containing dichloromethane [Fig. 6.9(a)]. The absorption spectrum is obtained by recording the RF heterodyne beating of the dual combs with and without the sample of dichloromethane, and it is then corroborated with the corresponding optical spectrum (see fig. 6.9(b)). As stated earlier, we acquire a time domain interferogram over 20 µs at 80 GSa/s, and perform an FFT to extract the beat note information in the RF domain. We achieved a high SNR without averaging multiple spectra, thus indicating the real-time nature of the acquisition system. The quartz cuvette showed no significant absorption in this wavelength range.

Note that the optical bandwidth of 170 nm accessible by the dual comb is narrower in our experiment than the full extent of the dual comb spectrum (400 nm) due to the photodiode's sharp roll-off in responsivity beyond 1640 nm and the decreasing power of the comb lines in accordance with the sech^2-shape which restricts the SNR of wavelengths shorter than 1460 nm. The gap in the detection around 1550 nm is due to the finite roll-off of the shortpass OD2 filter used in the experiment. By using a shortpass filter with a higher extinction, say OD4, this gap can be eliminated. As an example, we show the filtered comb in Fig. 6.10.

6.4 Conclusions and outlook

We have demonstrated the generation of two frequency combs based on Si_3N_4 microresonators with slightly different repetition rates on the same chip. The

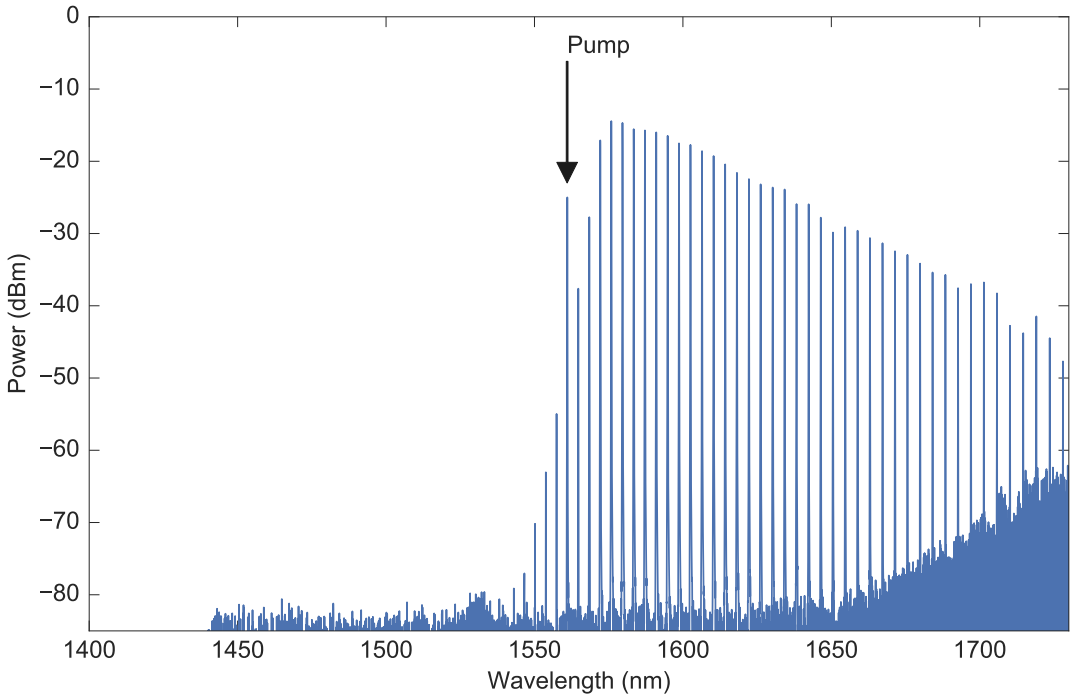

Figure 6.10: **Frequency comb filtered with a long pass filter.** An example of a comb filtered by an OD4 long pass filter with a cutoff wavelength at $\sim$ 1560 nm.

generated combs have a broadband spectrum spanning 400 nm (51 THz), high repetition rates of 450 GHz with a repetition rate difference of 1.12 GHz. Dispersion engineering by tailoring the waveguide dimensions should allow us to further broaden the bandwidth of the combs up to an octave [57, 255, 300]. The combs possess a high degree of relative coherence since they are generated from the same fixed-frequency low-noise cw pump laser, as evidenced by narrow RF heterodyne beat notes with a linewidth of 10 kHz. Both the combs are operated in the single-soliton mode-locked state with the help of integrated heaters to tune the resonance wavelengths of the microresonators.

The approach we have developed can be extended to other wavelength ranges,

such as the mid-IR "molecular fingerprint" region, where several molecules have their strongest fundamental rovibrational resonances, as shown by the recent experiments by Yu *et al.* [312]. The repetition rate of our dual comb (450 GHz) provides sufficient resolution for spectroscopy of liquids and solids, which typically have broad absorption features of a few THz or more, as demonstrated in the real-time DCS measurement of dichloromethane reported here. Higher resolution spectroscopy, as required typically for gases, is possible by tuning the laser and the resonator synchronously once the comb is generated. High-repetition-rate combs such as the ones shown here are desirable for fast acquisition timescales, as the speed of acquisition scales with an increase of the comb tooth spacing f_{rep} [306]. Such combs are promising for investigating rapid dynamical processes such as chemical reactions [323] or single-shot measurements in turbulent environments [306].

In the present work, the dual-comb source is coupled out of the chip using a single waveguide, which is adequate for absorption spectroscopy as it requires detecting only the amplitude information. Dispersive measurements which require phase sensitive detection [301, 305] could be enabled by designing two separate outputs for the two combs, one used as the reference arm and the other sent to the sample to be measured. This would require incorporating either drop ports on both the rings or splitting the pump laser before sending them to two waveguide-coupled rings in a non-cascaded geometry. The latter configuration also permits combs with smaller difference in repetition rates ($f_{\mathrm{rep}} < 10$ MHz, see Supplementary Information section II), making time-domain measurements more feasible, at the cost of increasing the minimum time needed for acquiring a single-shot spectrum. Combined with such improvements, a chip-scale microresonator based dual-comb source opens the door to realizing a compact portable spectrometer for stand-off

molecular sensing in the field.

CHAPTER 7

FUTURE WORK

This dissertation summarized an attempt towards advancing the state-of-the-art in the field of FWM-based parametric oscillators and their applications in squeezed light generation and dual comb spectroscopy. Quantum and nonlinear photonics is a rapidly evolving field, and several improvements to the demonstrations in the present work as well as new research directions can be identified.

7.1 Improvements in two-mode squeezing

Perhaps an immediate improvement of the current work could involve the quest for larger squeezing levels over broader bandwidths. Using the higher intrinsic quality factors recently demonstrated [77], it should be possible to improve the escape efficiency η_c without significantly increasing the power threshold, i.e. keeping the loaded Q the same. An increase in the escape efficiency in principle leads to a higher squeezing factor. Attempting larger squeezing levels would not just be a technical issue, but could also unravel new physics in the form of limiting noise mechanisms such as Brillouin and Raman scattering, which have not been hitherto observed in Si_3N_4 conclusively.

The dearth of commercially available balanced detectors at 1550 nm with RF bandwidths up to a GHz or more precluded our observation of squeezing at higher radiofrequencies. Broadband quantum noise reduction should in principle already exist in the microrings we have investigated because their cavity linewidth is ~ 1 GHz. Custom homemade detectors might be required for such an experiment, as has been reported by Ast *et al.* [210, 324] and Vahlbruch *et al.* [125].

7.2 Alternative material platforms

We have exclusively dealt with Si_3N_4 as the nonlinear photonic material in our work. New platforms such as aluminum nitride and AlGaAs, though not standard CMOS materials, have benefits in their own ways. AlGaAs, for example, has a nonlinearity that is two orders of magnitude larger than silicon nitride [52]. Currently, AlGaAs lags behind Si_3N_4 in terms of quality factor, and has comparable threshold powers for parametric oscillation. Continuous progress in the fabrication techniques and material quality for AlGaAs could lead to much lower threshold powers and stronger squeezing. Both these materials have a nonvanishing second order nonlinearity, and the interplay between $\chi^{(2)}$ and $\chi^{(3)}$ has the potential to produce rich dynamics. Additionally, the Pockel's effect arising from the second-order nonlinearity enables efficient electrical tuning on much faster timescales than what is possible with microheaters [252].

Lithium niobate has always been a strong contender for quantum photonics, but its low index contrast configuration produced by proton exchange or titanium indiffusion [195] has hindered the fabrication of compact devices. Several groups are currently working on high-confinement lithium niobate waveguides and resonators that can be integrated on chip, and further advancements could make it an attractive material in the future [325–328].

7.3 Phase-sum squeezing and entanglement

The residual intensity noise and issues with the stability of the setup kept us from observing phase-sum squeezing in the silicon nitride microrings. Theoretical

calculations also predict a large rotation of the optimal quadratures where phase-sum squeezing is expected. By choosing the proper detuning of the analysis cavities as described in Chapter 5, it should be possible to simultaneously observe phase sum squeezing and intensity difference squeezing, which in tandem contributes to continuous variable entanglement. A Pound-Drever-Hall [276] technique could be implemented to provide a more stable locking of the laser to the filter cavity, by increasing the servo bandwidth for feedback control. Other possible routes to building a passively stable filter cavity include better temperature control of the cavity environment and the use of a low-thermal-expansion coefficient metal (e.g. stainless steel or invar) as the cavity base platform. The initial design of the filter cavity used a long roundtrip length so that multiple resonances of the cavity fit within one linewidth of the on-chip microring. The incorporation of platinum microheaters obviates this need, and a much smaller filter cavity could improve the stability, albeit at the cost of sacrificing some of the transmission efficiency.

7.4 Multimode phase correlations

We have only looked at intensity correlations between the higher order signal and idler modes in Chapter 5. The study of phase correlations beyond the first pair of signal and idler modes has the potential to provide a better understanding of the quantum dynamics of this system. Such an investigation is highly promising from the purview of generating cluster states on chip in a compact and scalable platform. A full multimode characterization could reveal unexpected behavior in the quantum properties of the frequency comb which cannot be seen in two-mode correlations (à la P. W Anderson, "more is different" [329]).

In the long run, it would be ideal to have the pump laser and the filter and analysis cavities all integrated on the same chip. This would require challenging design considerations as the microring OPO, the filter cavity and the analysis cavities have very different linewidths. Using higher bandwidth RF detection might relax or altogether obviate the need for filter cavities, as the excess intensity and phase noise drop drastically with increasing frequencies away from the carrier. We are currently limited to the 3–5 MHz range by the balanced detectors at our disposal. Demultiplexing of the pump and the squeezed beams on an integrated platform has been previously shown in lithium niobate [148]. Rings with a different cross-sectional dimension and different radius than the microring OPO are perfect candidates for separating the pump, signal and idler modes on chip, and hence reducing the inefficiencies in detection introduced by the diffraction grating.

7.5 Improvements to dual frequency combs

Finally, the field of microresonator based dual frequency combs is in its inception. Numerous directions could be taken, both in terms of improving the dual comb source as well as the in terms of spectroscopic applications.

A non-cascaded geometry, where the two comb generation rings are coupled to distinct bus waveguides, would enable the difference in repetition rates to be driven to much smaller values, all the way to the MHz regime. Such a design would enable easier data acquisition in the time domain, without requiring high speed oscilloscopes.

An acousto-optic modulator could be incorporated to frequency shift the pump for one of the rings and prevent the interference of beat notes from the red side

of the comb with those from the blue side. Using better dispersion engineering techniques, the optical bandwidth of the generated comb could be broadened to an octave. Larger rings would significantly bring down the FSR and therefore result in a higher resolution for spectroscopy. One could even envision the integration of an electro-optic modulator followed by a long waveguide for producing frequency agile combs, as demonstrated recently in fibers [317, 319, 320]. Similarly, in table-top comb systems, two counterpropagating soltion pulse trains have been realized within a single cavity to generate dual combs with a slight difference in repetition rate [330]. This configuration, when realized on chip-scale Si_3N_4 resonators [331], has the promise of producing a compact and stable dual comb. Counterpropagating soliton pulse trains could provide valuable insight into the interplay between the thermal and Kerr-nonlinear dynamics of comb formation.

The resolution of the current dual comb source is limited by the FSR of the rings. Preliminary experiments have shown the ability to tune the resonance over several tens of GHz while keeping the comb in the mode-locked state. Increasing this tuning range and combining it with smaller repetition rate combs (100–200 GHz) should enable us to scan across one full FSR, which would reduce the resolution to the much narrower comb linewidth. From a fundamental point of view, detailed characterization of the RF domain properties of the dual comb, e.g. the phase noise of the beat notes and the long term drifts over timescales of several hours, would determine ultimate stability limits of the system.

There has been active research on the integration of laser gain media with silicon photonics to develop fully integrated sources of frequency combs. Two popular avenues being pursued currently are the hybrid integration of III-V materials and the use of rare-earth doping to provide gain [332–335]. Specifically, Hosseini *et*

al. have demonstrated a 75 mW laser on a silicon nitride platform using erbium doped aluminum oxide layers in a CMOS compatible process, which places full integration within reach in the near future.

Our proof-of-principle demonstration of spectroscopy was only a first in the series of many possible single-chip DCS experiments. For miniature dual comb spectometers, we could open up a window in the cladding after the comb generation stage to permit evanescent interaction of the sample with the waveguide mode. This would be a very powerful method for sensing and molecular fingerprinting of extremely small amounts of liquids and gases. Besides spectroscopy, in-situ ellipsometry appears to be a very useful application of dual combs [336], with the possibility to reduce ellipsometric data acquisition times and footprints by orders of magnitude.

I believe that the work presented in this dissertation has opened up new approaches to experimental quantum optics and has stimulated compact sources for applications of nonlinear optics such as dual comb spectroscopy. With further development of the techniques reported here, integrated photonics is poised to have a major contribution in realizing Feynman's vision of a universal quantum computer [337], and, in parallel, bring compact, ultraprecise and fast sensing and spectroscopic methods to a platform amenable to real-world applications.

APPENDIX A

MICRORESONATOR PLATFORMS FOR NONLINEAR AND QUANTUM PHOTONICS

This appendix summarizes the various nonlinear microresonator platforms that have been investigated for parametric oscillation around 1550 nm till date. We focus on materials based on the third-order Kerr nonlinearity. Note that parametric oscillation in silicon is inhibited by nonlinear losses such as two-photon absorption and free-carrier absorption around 1550 nm, but has been reported in the mid infrared [51, 198, 338]. For consistency the quality factors and parametric oscillation thresholds have been obtained from the papers where both are explicitly mentioned. Higher Q's have been reported in some of these platforms such as silica than mentioned in this table, but we restricted the numbers to papers where the threshold is also mentioned.

Platform	n	n_2 (m^2/W)	Q_{int} ($\times 10^6$)	Min P_{th} (mW)	CMOS compatible	Planar
Crystalline fluorides	1.44	3.2×10^{-20}	10^4	0.30	No	No
Silica microtoroid	1.45	2.2×10^{-20}	125	0.34	Yes	No
Silica wedge	1.45	2.2×10^{-20}	875	10	Yes	Yes
Si	3.45	5×10^{-18}	0.76	3	Yes	Yes
Diamond	2.4	8.2×10^{-20}	1	20	Yes	Yes
$Al_{0.17}Ga_{0.83}As$	3.30	2.6×10^{-17}	0.10	3	No	Yes
Hydex	1.7	1.2×10^{-19}	1	50	Yes	Yes
AlN	2.1	2.3×10^{-19}	0.80	200	Yes, non-standard	Yes
Si_3N_4	2.0	2.5×10^{-19}	36	0.33	Yes	Yes

Table A.1: Summary of nonlinear microresonator platforms

APPENDIX B

DEVICE FABRICATION

The devices were fabricated using a process similar to that described in Refs. [69, 71] and Ref. [77]. We start with a 4-inch diameter virgin Si wafer and thermally oxidize it to obtain a 4 µm buried oxide layer to be used as the undercladding. Trenches are defined before nitride deposition on the oxide to mitigate stress-induced crack propagation in the film. A 730 - 950 nm thick layer of stoichiometric silicon nitride is grown (depending on the desired thickness for the relevant design) using low-pressure chemical vapour deposition (LPCVD) in two steps. The waveguides and resonators are patterned with electron beam lithography on a JEOL 9500FS system using ma-N 2403 resist. An alternative procedure uses an oxide hard mask to better transfer patterns to the nitride layer from the resist. This oxide is deposited using plasma-enhanced chemical vapor deposition (PECVD). The pattern is etched using inductively-coupled plasma reactive-ion etching (ICP RIE) with CHF_3, N_2 and O_2 gases. The devices are annealed in an argon atmosphere at 1200 °C after stripping the resist to remove residual N-H bonds which introduce optical loss in the nitride film. The devices are clad with 500 nm of high temperature oxide (HTO) at 800 °C followed by a 2.5 µm thick overcladding of PECVD oxide. We sputter 100 nm of platinum on top of the oxide cladding and define the heaters using photolithography and lift-off. The heaters have a width of 6 µm, and are sufficiently far from the waveguide layer so as not to introduce any optical loss due to interaction with the metal [77, 239, 240].

APPENDIX C

MIRROR COATING DESIGN AND FABRICATION

We designed the flat input and output coupling mirrors of the filter cavity in Section 5.2 using a distributed Bragg reflector (DBR) scheme, consisting of alternating stacks of silicon nitride and silicon dioxide. The thickness of each layer is chosen to be a quarter of the wavelength in the material. For the targeted reflectivity of 99% per layer, we use 12 pairs of layers. The high index contrast between nitride and oxide enables us to have a broad bandwidth. The low angle of incidence (< 1.5 °) makes the design constraints less polarization sensitive. A transfer matrix method was used to numerically simulate the reflectivity of the DBR stack over the desired wavelength range [271]. The simulated reflectivity was higher than 98.5% between $\lambda = 1.5$ - 1.65 µm.

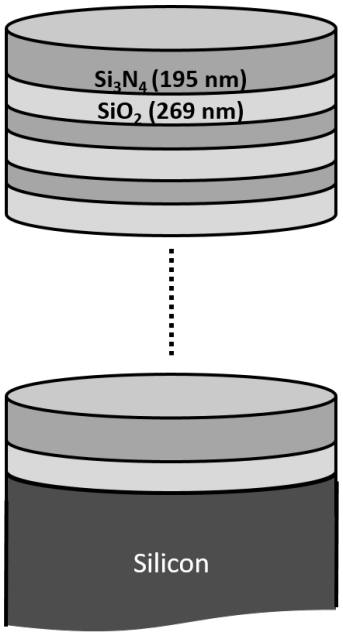

Figure C.1: Design of the distributed Bragg reflector stack. Each layer is quarter wavelength thick $\lambda/2n$, where n is the index of the corresponding layer.

The mirrors were fabricated in the Cornell Nanoscale Facility using plasma enhanced chemical vapor deposition on a crystalline silicon wafer. Importantly, the silicon wafer must be double-side polished to allow transmission through the mirror. The nitride layer was 195 nm thick and the oxide layer was 269 nm thick. We used a low stress silicon nitride recipe because the total accumulated thickness of the layers was around 4 µm, which is thick enough for stress-induced cracks to damage the films. The measured loss through the DBR stack was lower than what could be detected in the Filmetrics thin-film characterization tool. An anti-reflection coating can be deposited on the other side of the wafer to improve transmission efficiency through the cavity.

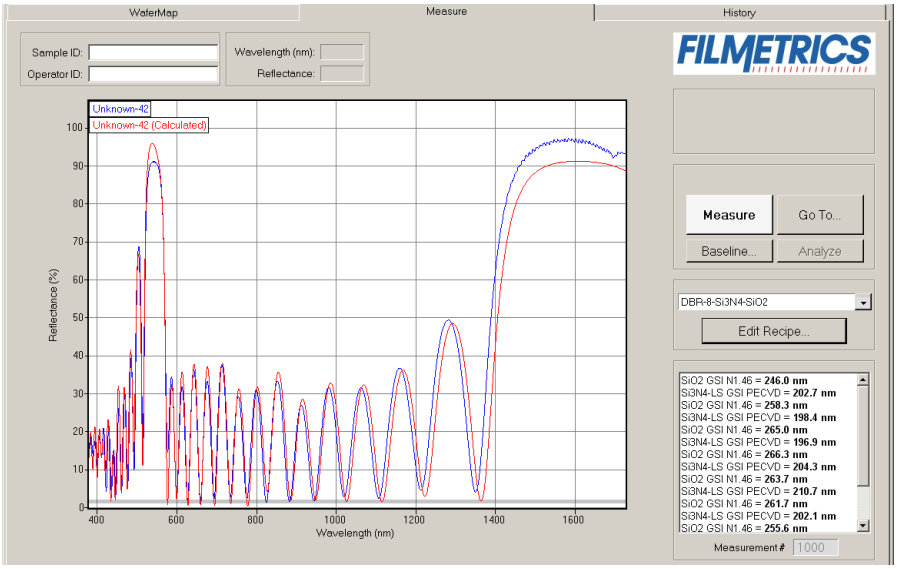

Figure C.2: Design of the distributed Bragg reflector stack. Each layer is quarter wavelength thick $\lambda/2n$, where n is the index of the corresponding layer.

A sample measurement of the reflectivity of the mirror after 8 pairs of alternating quarter wave layers have been deposited is shown in Fig. C.2. A reasonably good fit is obtained over a wide wavelength range. The Filmetrics tool used for this characterization saturated at higher reflectivities obtained with a larger num-

ber of layers, and hence direct transmission based measurements or cavity based measurements were used for $R > 99\%$.

APPENDIX D

CMRR MEASUREMENT OF DETECTORS

The common-mode rejection ratio is an important figure of merit of any balanced detection system. We measured it using a function generator to artificially inject an RF signal on the current modulation input of the laser as shown in Fig. D.1. The individual beam noises were measured using a setup similar to the shot noise calibration experiment. We measure a CMRR greater than 35 dB below 2 MHz [Fig. D.2].

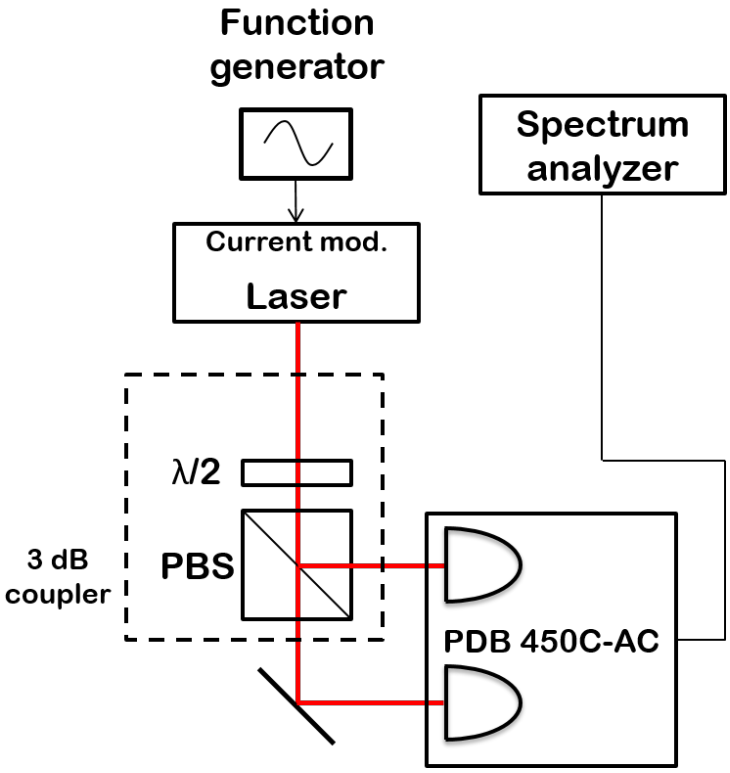

Figure D.1: Setup to measure CMRR.

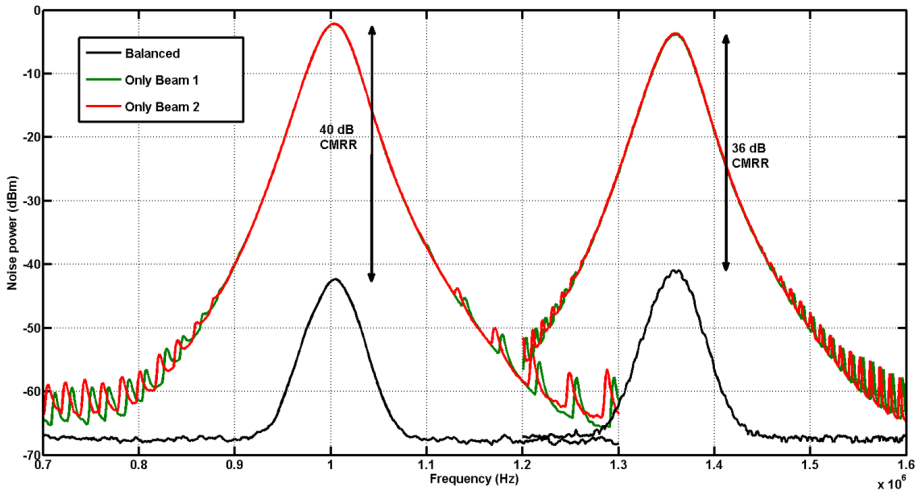

Figure D.2: The measured CMRR is higher than 35 dB around the relevant frequency range.

APPENDIX E

ANALYSIS CAVITY EQUATIONS FOR PHASE QUADRATURE MEASUREMENTS

Here we provide detailed expressions for the coefficients for an analysis cavity for Section 5.3, following the treatment of Villar [278]. All frequencies in these expressions, such as the cavity detuning Δ and the analysis frequency ν' are normalized to the cavity FWHM bandwidth $\delta\nu_c = c/LF$, where c is the speed of light, L is the roundtrip length and F is the finesse.

$$2g_p = e^{-i\theta_R(\Delta)} r(\Delta + \nu') + e^{i\theta_R(\Delta)} r^*(\Delta - \nu') \tag{E.1}$$

$$2g_q = e^{-i\theta_R(\Delta)} r(\Delta + \nu') - e^{i\theta_R(\Delta)} r^*(\Delta - \nu') \tag{E.2}$$

$$2g_{vp} = e^{-i\theta_T(\Delta)} t(\Delta + \nu') - e^{i\theta_T(\Delta)} t^*(\Delta - \nu') \tag{E.3}$$

$$2g_{vq} = e^{-i\theta_T(\Delta)} t(\Delta + \nu' - e^{i\theta_T(\Delta)} t^*(\Delta - \nu') \tag{E.4}$$

where $r(\Delta) = |r(\Delta)| \exp(i\theta_R(\Delta))$, and $t(\Delta) = |t(\Delta)| \exp(i\theta_T(\Delta))$

$$r(\Delta) = \frac{r_1 - r_2 \exp(i2\pi\Delta/F)}{1 - r_1 r_2 \exp(i2\pi\Delta/F)} \tag{E.5}$$

$$t\Delta) = \frac{t_1 t_2 \exp(i\pi\Delta/F)}{1 - r_1 r_2 \exp(i2\pi\Delta/F)} \tag{E.6}$$

Here r_1, t_1 are the amplitude reflection and transmission coefficients of the input coupling mirror of the cavity, and $t_2 = \sqrt{1 - r_2^2}$ represents the losses due to the other mirrors and the spurious losses in the cavity. For a good (overcoupled) analysis cavity, we want $r_2^2 \approx 1$ and $t_2 \ll t_1$.

BIBLIOGRAPHY

[1]R. Soref, "The past, present, and future of silicon photonics", IEEE Journal of Selected Topics in Quantum Electronics **12**, 1678–1687 (2006).

[2]B. Jalali and S. Fathpour, "Silicon photonics", Lightwave Technology, Journal of **24**, 4600–4615 (2006).

[3]T. E. Northup and R. Blatt, "Quantum information transfer using photons", Nature Photonics **8**, 356–363 (2014).

[4]A. Aspuru-Guzik and P. Walther, "Photonic quantum simulators", Nature Physics **8**, 285–291 (2012).

[5]I. Bloch, J. Dalibard, and S. Nascimbne, "Quantum simulations with ultracold quantum gases", Nature Physics **8**, 267–276 (2012).

[6]R. Blatt and C. F. Roos, "Quantum simulations with trapped ions", Nature Physics **8**, 277–284 (2012).

[7]J. I. Cirac and P. Zoller, "Goals and opportunities in quantum simulation", Nature Physics **8**, 264–266 (2012).

[8]A. Trabesinger, "Quantum simulation", Nature Physics **8**, 263–263 (2012).

[9]A. A. Houck, H. E. Treci, and J. Koch, "On-chip quantum simulation with superconducting circuits", Nature Physics **8**, 292–299 (2012).

[10]P. W. Shor, "Algorithms for quantum computation: discrete logarithms and factoring", in Proceedings 35th annual symposium on foundations of computer science (Nov. 1994), pp. 124–134.

[11]P. Shor, "Polynomial-time algorithms for prime factorization and discrete logarithms on a quantum computer", SIAM Rev. **41**, 303–332 (1999).

[12]C. H. BENNETT, "Quantum cryptography : public key distribution and coin tossing", International Conference on Computer System and Signal Processing, IEEE, 1984, 175–179 (1984).

[13]C. H. Bennett, G. Brassard, C. Crpeau, R. Jozsa, A. Peres, and W. K. Wootters, "Teleporting an unknown quantum state via dual classical and einstein-podolsky-rosen channels", Phys. Rev. Lett. **70**, 1895–1899 (1993).

[14]J. L. O'Brien, A. Furusawa, and J. Vukovi, "Photonic quantum technologies", Nature Photonics **3**, 687–695 (2009).

[15]C. Schriever, C. Bohley, J. Schilling, and R. B. Wehrspohn, "Strained silicon photonics", Materials **5**, 889–908 (2012).

[16]R. W. Boyd, *Nonlinear optics*, 3rd ed (Academic Press, Amsterdam ; Boston, 2008), 613 pp.

[17]G. P. Agrawal, *Nonlinear fiber optics*, Fifth edition (Elsevier/Academic Press, Amsterdam, 2013), 629 pp.

[18]J. E. Sharping, M. Fiorentino, A. Coker, P. Kumar, and R. S. Windeler, "Four-wave mixing in microstructure fiber", Opt. Lett., OL **26**, 1048–1050 (2001).

[19]J. Hansryd, P. A. Andrekson, M. Westlund, J. Li, and P. O. Hedekvist, "Fiber-based optical parametric amplifiers and their applications", IEEE Journal of Selected Topics in Quantum Electronics **8**, 506–520 (2002).

[20]R. K. W. Lau, M. Mnard, Y. Okawachi, M. A. Foster, A. C. Turner-Foster, R. Salem, M. Lipson, and A. L. Gaeta, "Continuous-wave mid-infrared frequency conversion in silicon nanowaveguides", Opt. Lett., OL **36**, 1263–1265 (2011).

[21]J. Levy, "Integrated nonlinear optics in silicon nitride waveguides and resonators", PhD thesis (Aug. 31, 2011).

[22]X. Xue, Y. Xuan, Y. Liu, P.-H. Wang, S. Chen, J. Wang, D. E. Leaird, M. Qi, and A. M. Weiner, "Mode-locked dark pulse kerr combs in normal-dispersion microresonators", Nat Photon **9**, 594–600 (2015).

[23]X. Xue, Y. Xuan, P.-H. Wang, Y. Liu, D. E. Leaird, M. Qi, and A. M. Weiner, "Normal-dispersion microcombs enabled by controllable mode interactions", Laser & Photonics Reviews **9**, L23–L28 (2015).

[24]V. E. Lobanov, G. Lihachev, and M. L. Gorodetsky, "Generation of platicons and frequency combs in optical microresonators with normal GVD by modulated pump", EPL **112**, 54008 (2015).

[25]Y. Liu, Y. Xuan, X. Xue, P.-H. Wang, S. Chen, A. J. Metcalf, J. Wang, D. E. Leaird, M. Qi, and A. M. Weiner, "Investigation of mode coupling in normal-dispersion silicon nitride microresonators for kerr frequency comb generation", Optica, OPTICA **1**, 137–144 (2014).

[26]S.-W. Huang, H. Zhou, J. Yang, J. McMillan, A. Matsko, M. Yu, D.-L. Kwong, L. Maleki, and C. Wong, "Mode-locked ultrashort pulse generation from on-chip normal dispersion microresonators", Phys. Rev. Lett. **114**, 053901 (2015).

[27]M. Soltani, A. B. Matsko, and L. Maleki, "Enabling arbitrary wavelength optical frequency combs on chip", arXiv:1509.07902 [physics] (2015).

[28]J. K. Jang, Y. Okawachi, M. Yu, K. Luke, X. Ji, M. Lipson, and A. L. Gaeta, "Dynamics of mode-coupling-induced microresonator frequency combs in normal dispersion", Opt. Express, OE **24**, 28794–28803 (2016).

[29]T. J. A. Kippenberg, "Nonlinear optics in ultra-high-q whispering-gallery optical microcavities", PhD thesis (California Institute of Technology, 2004).

[30]R. Stolen and J. Bjorkholm, "Parametric amplification and frequency conversion in optical fibers", IEEE Journal of Quantum Electronics **18**, 1062–1072 (1982).

[31]J. A. Giordmaine and R. C. Miller, "Tunable coherent parametric oscillation in LiNbO3 at optical frequencies", Phys. Rev. Lett. **14**, 973–976 (1965).

[32]L.-A. Wu, H. J. Kimble, J. L. Hall, and H. Wu, "Generation of squeezed states by parametric down conversion", Phys. Rev. Lett. **57**, 2520–2523 (1986).

[33]L.-A. Wu, M. Xiao, and H. J. Kimble, "Squeezed states of light from an optical parametric oscillator", J. Opt. Soc. Am. B **4**, 1465–1475 (1987).

[34]A. Heidmann, R. Horowicz, S. Reynaud, E. Giacobino, C. Fabre, and G. Camy, "Observation of quantum noise reduction on twin laser beams", Physical Review Letters **59**, 2555–2557 (1987).

[35]A. Matsko, A. Savchenkov, D. Strekalov, V. Ilchenko, and L. Maleki, "Optical hyperparametric oscillations in a whispering-gallery-mode resonator: threshold and phase diffusion", Physical Review A **71**, 033804 (2005).

[36]B. J. M. Hausmann, I. Bulu, V. Venkataraman, P. Deotare, and M. Lonar, "Diamond nonlinear photonics", Nat Photon **8**, 369–374 (2014).

[37]M. J. Werner, "Quantum soliton generation using an interferometer", Phys. Rev. Lett. **81**, 4132–4135 (1998).

[38]P. D. Drummond, R. M. Shelby, S. R. Friberg, and Y. Yamamoto, "Quantum solitons in optical fibres", Nature **365**, 307–313 (1993).

[39]K. Bergman, H. A. Haus, and M. Shirasaki, "Analysis and measurement of GAWBS spectrum in a nonlinear fiber ring", Appl. Phys. B **55**, 242–249 (1992).

[40]K. Bergman, H. A. Haus, E. P. Ippen, and M. Shirasaki, "Squeezing in a fiber interferometer with a gigahertz pump", Opt. Lett., OL **19**, 290–292 (1994).

[41]Y. Lai and S.-S. Yu, "General quantum theory of nonlinear optical-pulse propagation", Phys. Rev. A **51**, 817–829 (1995).

[42]R. Dong, J. Heersink, J. F. Corney, P. D. Drummond, U. L. Andersen, and G. Leuchs, "Experimental evidence for raman-induced limits to efficient squeezing in optical fibers", Optics Letters **33**, 116 (2008).

[43]S. J. Carter and P. D. Drummond, "Squeezed quantum solitons and raman noise", Phys. Rev. Lett. **67**, 3757–3760 (1991).

[44]F. X. Krtner, D. J. Dougherty, H. A. Haus, and E. P. Ippen, "Raman noise and soliton squeezing", J. Opt. Soc. Am. B, JOSAB **11**, 1267–1276 (1994).

[45]M. Karpov, H. Guo, A. Kordts, V. Brasch, M. H. Pfeiffer, M. Zervas, M. Geiselmann, and T. J. Kippenberg, "Raman self-frequency shift of dissipative kerr solitons in an optical microresonator", Phys. Rev. Lett. **116**, 103902 (2016).

[46]L. Zhang, Q. Lin, L. C. Kimerling, and J. Michel, "Self-frequency shift of cavity soliton in kerr frequency comb", arXiv:1404.1137 [nlin, physics:physics] (2014).

[47]P. DelHaye, A. Schliesser, O. Arcizet, T. Wilken, R. Holzwarth, and T. J. Kippenberg, "Optical frequency comb generation from a monolithic microresonator", Nature **450**, 1214–1217 (2007).

[48]A. A. Savchenkov, A. B. Matsko, D. Strekalov, M. Mohageg, V. S. Ilchenko, and L. Maleki, "Low threshold optical oscillations in a whispering gallery mode ${\mathrm{c}\mathrm{a}\mathrm{f}}_{2}$ resonator", Phys. Rev. Lett. **93**, 243905 (2004).

[49]L. Razzari, D. Duchesne, M. Ferrera, R. Morandotti, S. Chu, B. E. Little, and D. J. Moss, "CMOS-compatible integrated optical hyper-parametric oscillator", Nat Photon **4**, 41–45 (2010).

[50]H. Jung, C. Xiong, K. Y. Fong, X. Zhang, and H. X. Tang, "Optical frequency comb generation from aluminum nitride microring resonator", Opt. Lett. **38**, 2810–2813 (2013).

[51]A. G. Griffith, R. K. W. Lau, J. Cardenas, Y. Okawachi, A. Mohanty, R. Fain, Y. H. D. Lee, M. Yu, C. T. Phare, C. B. Poitras, A. L. Gaeta, and M. Lipson, "Silicon-chip mid-infrared frequency comb generation", Nat Commun **6**, 6299 (2015).

[52]M. Pu, L. Ottaviano, E. Semenova, and K. Yvind, "Efficient frequency comb generation in AlGaAs-on-insulator", Optica, OPTICA **3**, 823–826 (2016).

[53]T. J. Kippenberg, R. Holzwarth, and S. A. Diddams, "Microresonator-based optical frequency combs", Science **332**, 555–559 (2011).

[54]D. J. Moss, R. Morandotti, A. L. Gaeta, and M. Lipson, "New CMOS-compatible platforms based on silicon nitride and hydex for nonlinear optics", Nat Photon **7**, 597–607 (2013).

[55]P. Marin-Palomo, J. N. Kemal, M. Karpov, A. Kordts, J. Pfeifle, M. H. P. Pfeiffer, P. Trocha, S. Wolf, V. Brasch, R. Rosenberger, K. Vijayan, W. Freude, T. J. Kippenberg, and C. Koos, "Microresonator solitons for massively parallel coherent optical communications", arXiv:1610.01484 [nlin, physics:physics] (2016).

[56]P. Marin, J. Pfeifle, M. Karpov, P. Trocha, R. Rosenberger, K. Vijayan, S. Wolf, J. N. Kemal, A. Kordts, M. Pfeiffer, V. Brasch, W. Freude, T. Kippenberg, and C. Koos, "50 tbit/s massively parallel WDM transmission in c and l band using interleaved cavity-soliton kerr combs", in Conference on lasers and electro-optics (2016), paper STu1g.1 (June 5, 2016), STu1G.1.

[57]V. Brasch, M. Geiselmann, T. Herr, G. Lihachev, M. H. P. Pfeiffer, M. L. Gorodetsky, and T. J. Kippenberg, "Photonic chip-based optical frequency comb using soliton cherenkov radiation", Science **351**, 357–360 (2016).

[58]M. H. P. Pfeiffer, A. Kordts, V. Brasch, M. Zervas, M. Geiselmann, J. D. Jost, and T. J. Kippenberg, "Photonic damascene process for integrated high-q microresonator based nonlinear photonics", Optica, OPTICA **3**, 20–25 (2016).

[59]M. Karpov, H. Guo, E. Lucas, A. Kordts, M. H. P. Pfeiffer, G. Lichachev, V. E. Lobanov, M. L. Gorodetsky, and T. J. Kippenberg, "Universal dynamics and controlled switching of dissipative kerr solitons in optical microresonators", arXiv preprint arXiv:1601.05036 (2016).

[60]Y. Xuan, Y. Liu, L. T. Varghese, A. J. Metcalf, X. Xue, P.-H. Wang, K. Han, J. A. Jaramillo-Villegas, A. A. Noman, C. Wang, S. Kim, M. Teng, Y. J. Lee, B. Niu, L. Fan, J. Wang, D. E. Leaird, A. M. Weiner, and M. Qi, "High-q silicon nitride microresonators exhibiting low-power frequency comb initiation", Optica, OPTICA **3**, 1171–1180 (2016).

[61]P.-H. Wang, J. A. Jaramillo-Villegas, Y. Xuan, X. Xue, C. Bao, D. E. Leaird, M. Qi, and A. M. Weiner, "Intracavity characterization of micro-comb generation in the single-soliton regime", arXiv preprint arXiv:1603.03154 (2016).

[62]X. Xue, Y. Xuan, C. Wang, P.-H. Wang, Y. Liu, B. Niu, D. E. Leaird, M. Qi, and A. M. Weiner, "Thermal tuning of kerr frequency combs in silicon nitride microring resonators", Optics Express **24**, 687 (2016).

[63]Q. Li, T. C. Briles, D. A. Westly, T. E. Drake, J. R. Stone, B. R. Ilic, S. A. Diddams, S. B. Papp, and K. Srinivasan, "Stably accessing octave-spanning microresonator frequency combs in the soliton regime", Optica **4**, 193 (2017).

[64]S.-W. Huang, J. Yang, M. Yu, B. H. McGuyer, D.-L. Kwong, T. Zelevinsky, and C. W. Wong, "A broadband chip-scale optical frequency synthesizer at 2.7 10^{16} relative uncertainty", Science Advances **2**, e1501489 (2016).

[65]S.-W. Huang, A. Kumar, J. Yang, M. Yu, D.-L. Kwong, and C. W. Wong, "Phase stabilization of kerr frequency comb internally without nonlinear optical interferometry", arXiv:1611.02858 [physics] (2016).

[66]S.-W. Huang, H. Liu, J. Yang, M. Yu, D.-L. Kwong, and C. W. Wong, "Smooth coherent kerr frequency combs generation with broadly tunable pump by higher order mode suppression", arXiv preprint arXiv:1602.00824 (2016).

[67]*Integrated photonics | clifford pollock | springer* ().

[68]K. Luke, Y. Okawachi, M. R. E. Lamont, A. L. Gaeta, and M. Lipson, "Broadband mid-infrared frequency comb generation in a si_3n_4 microresonator", Opt. Lett., OL **40**, 4823–4826 (2015).

[69]K. Luke, "Parametric frequency comb generation in visible and mid-infrared wavelengths with integrated silicon nitride ring resonators", PhD thesis (Feb. 1, 2016).

[70]A. Griffith, J. Cardenas, C. B. Poitras, and M. Lipson, "High quality factor and high confinement silicon resonators using etchless process", Opt. Express, OE **20**, 21341–21345 (2012).

[71]K. Luke, A. Dutt, C. B. Poitras, and M. Lipson, "Overcoming si3n4 film stress limitations for high quality factor ring resonators", Opt. Express **21**, 22829–22833 (2013).

[72]J. Cardenas, C. B. Poitras, J. T. Robinson, K. Preston, L. Chen, and M. Lipson, "Low loss etchless silicon photonic waveguides", Opt. Express, OE **17**, 4752–4757 (2009).

[73]L.-W. Luo, G. S. Wiederhecker, J. Cardenas, C. Poitras, and M. Lipson, "High quality factor etchless silicon photonic ring resonators", Opt. Express, OE **19**, 6284–6289 (2011).

[74]M.-C. Tien, J. F. Bauters, M. J. R. Heck, D. T. Spencer, D. J. Blumenthal, and J. E. Bowers, "Ultra-high quality factor planar si_3n_4 ring resonators on si substrates", Optics Express **19**, 13551 (2011).

[75]J. F. Bauters, M. J. R. Heck, D. John, D. Dai, M.-C. Tien, J. S. Barton, A. Leinse, R. G. Heideman, D. J. Blumenthal, and J. E. Bowers, "Ultra-low-loss high-aspect-ratio si_3n_4 waveguides", Opt. Express, OE **19**, 3163–3174 (2011).

[76]P. Dong, W. Qian, S. Liao, H. Liang, C.-C. Kung, N.-N. Feng, R. Shafiiha, J. Fong, D. Feng, A. V. Krishnamoorthy, and M. Asghari, "Low loss shallow-ridge silicon waveguides", Opt. Express, OE **18**, 14474–14479 (2010).

[77]X. Ji, F. A. S. Barbosa, S. P. Roberts, A. Dutt, J. Cardenas, Y. Okawachi, A. Bryant, A. L. Gaeta, and M. Lipson, "Ultra-low-loss on-chip resonators with sub-milliwatt parametric oscillation threshold", Optica, OPTICA **4**, 619–624 (2017).

[78]D. T. Spencer, J. F. Bauters, M. J. R. Heck, and J. E. Bowers, "Integrated waveguide coupled si_3n_4 resonators in the ultrahigh-q regime", Optica **1**, 153 (2014).

[79]D. K. Armani, T. J. Kippenberg, S. M. Spillane, and K. J. Vahala, "Ultra-high-q toroid microcavity on a chip", Nature **421**, 925–928 (2003).

[80]V. B. Braginsky, M. L. Gorodetsky, and V. S. Ilchenko, "Quality-factor and nonlinear properties of optical whispering-gallery modes", Physics Letters A **137**, 393–397 (1989).

[81]L. Collot, V. Lefvre-Seguin, M. Brune, J. M. Raimond, and S. Haroche, "Very high- q whispering-gallery mode resonances observed on fused silica microspheres", EPL **23**, 327 (1993).

[82]V. S. Ilchenko, A. A. Savchenkov, A. B. Matsko, and L. Maleki, "Nonlinear optics and crystalline whispering gallery mode cavities", Phys. Rev. Lett. **92**, 043903 (2004).

[83]A. A. Savchenkov, A. B. Matsko, V. S. Ilchenko, and L. Maleki, "Optical resonators with ten million finesse", Opt. Express, OE **15**, 6768–6773 (2007).

[84]M. Soltani, S. Yegnanarayanan, and A. Adibi, "Ultra-high q planar silicon microdisk resonators for chip-scale silicon photonics", Opt. Express, OE **15**, 4694–4704 (2007).

[85]A. Yariv, "Critical coupling and its control in optical waveguide-ring resonator systems", IEEE Photonics Technology Letters **14**, 483–485 (2002).

[86]A. Yariv, "Universal relations for coupling of optical power between microresonators and dielectric waveguides", Electronics Letters **36**, 321–322 (2000).

[87]N. Sherwood-Droz, H. Wang, L. Chen, B. G. Lee, A. Biberman, K. Bergman, and M. Lipson, "Optical 4x4 hitless slicon router for optical networks-on-chip (NoC)", Optics Express **16**, 15915 (2008).

[88]A. Dutt, K. Luke, S. Manipatruni, A. L. Gaeta, P. Nussenzveig, and M. Lipson, "On-chip optical squeezing", Physical Review Applied **3**, 044005 (2015).

[89]A. Lvovsky, "Squeezed light", arXiv preprint arXiv:1401.4118 (2014).

[90]R. J. Glauber, "Photon correlations", Physical Review Letters **10**, 84 (1963).

[91]R. J. Glauber, "Coherent and incoherent states of the radiation field", Phys. Rev. **131**, 2766–2788 (1963).

[92]E. C. G. Sudarshan, "Equivalence of semiclassical and quantum mechanical descriptions of statistical light beams", Phys. Rev. Lett. **10**, 277–279 (1963).

[93]F. Rana, *Lecture notes on quantum optics for photonics and optoelectronics*, https://courses.cit.cornell.edu/ece531/Lectures/Lectures.htm (visited on 02/26/2017).

[94]G. Breitenbach, S. Schiller, and J. Mlynek, "Measurement of the quantum states of squeezed light", Nature **387**, 471–475 (1997).

[95]Y. K. Chembo, "Quantum dynamics of kerr optical frequency combs below and above threshold: spontaneous four-wave mixing, entanglement, and squeezed states of light", Phys. Rev. A **93**, 033820 (2016).

[96]R. G. Hulet, E. S. Hilfer, and D. Kleppner, "Inhibited spontaneous emission by a rydberg atom", Phys. Rev. Lett. **55**, 2137–2140 (1985).

[97]E. Yablonovitch, "Inhibited spontaneous emission in solid-state physics and electronics", Phys. Rev. Lett. **58**, 2059–2062 (1987).

[98]D. F. Walls, "Squeezed states of light", Nature **306**, 141–146 (1983).

[99]C. M. Caves, "Quantum-mechanical noise in an interferometer", Phys. Rev. D **23**, 1693–1708 (1981).

[100]R. S. Bondurant and J. H. Shapiro, "Squeezed states in phase-sensing interferometers", Phys. Rev. D **30**, 2548–2556 (1984).

[101]L. Mita, J. Peina, and V. Peinov, "Quantum-statistical properties of optical parametric processes", Sov. J. Quantum Electron. **7**, 1458 (1977).

[102]L Mista, V Perinova, J perina, and Z. Braunerova, "Quantum statistical properties of degenerate parametric amplification process", Acta physica Polonica, A **51** (1977).

[103]M. T. Raiford, "Statistical dynamics of quantum oscillators and parametric amplification in a single mode", Phys. Rev. A **2**, 1541–1558 (1970).

[104]M. T. Raiford, "Degenerate parametric amplification with time-dependent pump amplitude and phase", Phys. Rev. A **9**, 2060–2069 (1974).

[105]B. R. Mollow and R. J. Glauber, "Quantum theory of parametric amplification. i", Phys. Rev. **160**, 1076–1096 (1967).

[106]B. R. Mollow and R. J. Glauber, "Quantum theory of parametric amplification. II", Phys. Rev. **160**, 1097–1108 (1967).

[107]D. F. Walls and P. Zoller, "Reduced quantum fluctuations in resonance fluorescence", Phys. Rev. Lett. **47**, 709–711 (1981).

[108]L. A. Lugiato, G. Strini, and F. D. Martini, "Squeezed states in second-harmonic generation", Optics Letters **8**, 256 (1983).

[109]M. D. Levenson, R. M. Shelby, A. Aspect, M. Reid, and D. F. Walls, "Generation and detection of squeezed states of light by nondegenerate four-wave mixing in an optical fiber", Phys. Rev. A **32**, 1550–1562 (1985).

[110]R. M. Shelby, M. D. Levenson, D. F. Walls, A. Aspect, and G. J. Milburn, "Generation of squeezed states of light with a fiber-optic ring interferometer", Phys. Rev. A **33**, 4008–4025 (1986).

[111]R. Slusher, L. Hollberg, B. Yurke, J. Mertz, and J. Valley, "Observation of squeezed states generated by four-wave mixing in an optical cavity", Physical Review Letters **55**, 2409–2412 (1985).

[112]C. F. McCormick, V. Boyer, E. Arimondo, and P. D. Lett, "Strong relative intensity squeezing by four-wave mixing in rubidium vapor", Opt. Lett., OL **32**, 178–180 (2007).

[113]C. F. McCormick, A. M. Marino, V. Boyer, and P. D. Lett, "Strong low-frequency quantum correlations from a four-wave-mixing amplifier", Physical Review A **78** (2008) 10.1103/PhysRevA.78.043816.

[114]Q. Glorieux, L. Guidoni, S. Guibal, J.-P. Likforman, and T. Coudreau, "Quantum correlations by four-wave mixing in an atomic vapor in a nonamplifying regime: quantum beam splitter for photons", Phys. Rev. A **84**, 053826 (2011).

[115]C. Liu, J. Jing, Z. Zhou, R. C. Pooser, F. Hudelist, L. Zhou, and W. Zhang, "Realization of low frequency and controllable bandwidth squeezing based on a four-wave-mixing amplifier in rubidium vapor", Opt. Lett., OL **36**, 2979–2981 (2011).

[116]Z. Qin, J. Jing, J. Zhou, C. Liu, R. C. Pooser, Z. Zhou, and W. Zhang, "Compact diode-laser-pumped quantum light source based on four-wave mixing in hot rubidium vapor", Opt. Lett., OL **37**, 3141–3143 (2012).

[117]U. L. Andersen, T. Gehring, C. Marquardt, and G. Leuchs, "30 years of squeezed light generation", Phys. Scr. **91**, 053001 (2016).

[118]E. S. Polzik, J. Carri, and H. J. Kimble, "Atomic spectroscopy with squeezed light for sensitivity beyond the vacuum-state limit", Appl. Phys. B **55**, 279–290 (1992).

[119]P. K. Lam, T. C. Ralph, B. C. Buchler, D. E. McClelland, H.-A. Bachor, and J. Gao, "Optimization and transfer of vacuum squeezing from an optical parametric oscillator", J. Opt. B: Quantum Semiclass. Opt. **1**, 469 (1999).

[120]S. Suzuki, H. Yonezawa, F. Kannari, M. Sasaki, and A. Furusawa, "7db quadrature squeezing at 860nm with periodically poled KTiOPO4", Applied Physics Letters **89**, 061116 (2006).

[121]Y. Takeno, M. Yukawa, H. Yonezawa, and A. Furusawa, "Observation of -9 dB quadrature squeezing with improvement of phase stability in homodyne measurement", Opt. Express, OE **15**, 4321–4327 (2007).

[122]H. Vahlbruch, M. Mehmet, S. Chelkowski, B. Hage, A. Franzen, N. Lastzka, S. Goler, K. Danzmann, and R. Schnabel, "Observation of squeezed light with 10-dB quantum-noise reduction", Phys. Rev. Lett. **100**, 033602 (2008).

[123]M. Mehmet, S. Ast, T. Eberle, S. Steinlechner, H. Vahlbruch, and R. Schnabel, "Squeezed light at 1550 nm with a quantum noise reduction of 12.3 dB", Opt. Express, OE **19**, 25763–25772 (2011).

[124]T. Eberle, S. Steinlechner, J. Bauchrowitz, V. Hndchen, H. Vahlbruch, M. Mehmet, H. Mller-Ebhardt, and R. Schnabel, "Quantum enhancement of the zero-area sagnac interferometer topology for gravitational wave detection", Phys. Rev. Lett. **104**, 251102 (2010).

[125]H. Vahlbruch, M. Mehmet, K. Danzmann, and R. Schnabel, "Detection of 15 dB squeezed states of light and their application for the absolute calibration of photoelectric quantum efficiency", Phys. Rev. Lett. **117**, 110801 (2016).

[126]A. Sizmann, R. J. Horowicz, G. Wagner, and G. Leuchs, "Observation of amplitude squeezing of the up-converted mode in second harmonic generation", Optics communications **80**, 138–142 (1990).

[127]P. Krz, R. Paschotta, K. Fiedler, and J. Mlynek, "Bright squeezed light by second-harmonic generation in a monolithic resonator", EPL **24**, 449 (1993).

[128]R. Paschotta, M. Collett, P. Krz, K. Fiedler, H. A. Bachor, and J. Mlynek, "Bright squeezed light from a singly resonant frequency doubler", Phys. Rev. Lett. **72**, 3807–3810 (1994).

[129]Y. Li, S. Zhang, J. Liu, and K. Zhang, "Quantum correlation between fundamental and second-harmonic fields via second-harmonic generation", J. Opt. Soc. Am. B **24**, 660–663 (2007).

[130]R. J Horowicz, "Quantum correlation between fundamental and second harmonic in SHG", Europhysics Letters (EPL) **10**, 537–542 (1989).

[131]T. C. Ralph, M. S. Taubman, A. G. White, D. E. McClelland, and H.-A. Bachor, "Squeezed light from second-harmonic generation: experiment versus theory", Opt. Lett. **20**, 1316–1318 (1995).

[132]M. J. Lawrence, R. L. Byer, M. M. Fejer, W. Bowen, P. K. Lam, and H.-A. Bachor, "Squeezed singly resonant second-harmonic generation in periodically poled lithium niobate", J. Opt. Soc. Am. B **19**, 1592–1598 (2002).

[133]M. K. Olsen and R. J. Horowicz, "Squeezing in the sum and difference fields in second harmonic generation", Optics Communications **168**, 135–143 (1999).

[134]T. Suhara, M. Fujimura, K. Kintaka, H. Nishihara, P. Kurz, and T. Mukai, "Theoretical analysis of squeezed-light generation by second-harmonic generation", IEEE Journal of Quantum Electronics **32**, 690–700 (1996).

[135]R. M. Shelby, M. D. Levenson, S. H. Perlmutter, R. G. DeVoe, and D. F. Walls, "Broad-band parametric deamplification of quantum noise in an optical fiber", Phys. Rev. Lett. **57**, 691–694 (1986).

[136]M. Rosenbluh and R. M. Shelby, "Squeezed optical solitons", Phys. Rev. Lett. **66**, 153–156 (1991).

[137]M. Shirasaki and H. A. Haus, "Squeezing of pulses in a nonlinear interferometer", J. Opt. Soc. Am. B, JOSAB **7**, 30–34 (1990).

[138]K. Bergman and H. A. Haus, "Squeezing in fibers with optical pulses", Opt. Lett., OL **16**, 663–665 (1991).

[139]J. E. Sharping, M. Fiorentino, and P. Kumar, "Observation of twin-beam-type quantum correlation in optical fiber", Opt. Lett. **26**, 367–369 (2001).

[140]J. Higuchi, N. Nishizawa, M. Mori, K. Yamane, and T. Goto, "Nonlinear polarization interferometer for photon-number squeezed light generation", Jpn. J. Appl. Phys. **40**, L1220 (2001).

[141]N. Nishizawa, K. Sone, J. Higuchi, M. Mori, K. Yamane, and T. Goto, "Squeezed vacuum generation using symmetric nonlinear polarization interferometer", Jpn. J. Appl. Phys. **41**, L130 (2002).

[142]A. Hosaka, K. Hirosawa, R. Sawada, and F. Kannari, "Generation of photon-number squeezed states with a fiber-optic symmetric interferometer", Opt. Express, OE **23**, 18850–18863 (2015).

[143]S. R. Friberg, S. Machida, M. J. Werner, A. Levanon, and T. Mukai, "Observation of optical soliton photon-number squeezing", Phys. Rev. Lett. **77**, 3775–3778 (1996).

[144]S. Splter, M. Burk, U. Strner, A. Sizmann, and G. Leuchs, "Propagation of quantum properties of sub-picosecond solitons in a fiber", Opt. Express, OE **2**, 77–83 (1998).

[145]D. Krylov and K. Bergman, "Amplitude-squeezed solitons from an asymmetric fiber interferometer", Opt. Lett., OL **23**, 1390–1392 (1998).

[146]S. Schmitt, J. Ficker, M. Wolff, F. Knig, A. Sizmann, and G. Leuchs, "Photon-number squeezed solitons from an asymmetric fiber-optic sagnac interferometer", Phys. Rev. Lett. **81**, 2446–2449 (1998).

[147]D. K. Serkland, M. M. Fejer, R. L. Byer, and Y. Yamamoto, "Squeezing in a quasi-phase-matched LiNbO_3 waveguide", Optics Letters **20**, 1649 (1995).

[148]G. Kanter, P. Kumar, R. Roussev, J. Kurz, K. Parameswaran, and M. Fejer, "Squeezing in a LiNbO3 integrated optical waveguide circuit", Optics Express **10**, 177 (2002).

[149]M. E. Anderson, M. Beck, M. G. Raymer, and J. D. Bierlein, "Quadrature squeezing with ultrashort pulses in nonlinear-optical waveguides", Optics Letters **20**, 620 (1995).

[150]M. Pysher, R. Bloomer, C. M. Kaleva, T. D. Roberts, P. Battle, and O. Pfister, "Broadband amplitude squeezing in a periodically poled $KTiOPO_4$ waveguide", Opt. Lett., OL **34**, 256–258 (2009).

[151]A. H. Safavi-Naeini, S. Grblacher, J. T. Hill, J. Chan, M. Aspelmeyer, and O. Painter, "Squeezed light from a silicon micromechanical resonator", Nature **500**, 185–189 (2013).

[152]M. Brambilla, F. Castelli, L. Lugiato, F. Prati, and G. Strini, "Nondegenerate four-wave mixing in a cavity: instabilities and quantum noise reduction", Optics Communications **83**, 367–389 (1991).

[153]L. A. Lugiato and F. Castelli, "Quantum noise reduction in a spatial dissipative structure", Phys. Rev. Lett. **68**, 3284–3286 (1992).

[154]C. Fabre, E. Giacobino, A. Heidmann, and S. Reynaud, "Noise characteristics of a non-degenerate optical parametric oscillator - application to quantum noise reduction", Journal de Physique **50**, 1209–1225 (1989).

[155]V. Giovannetti, S. Lloyd, and L. Maccone, "Quantum-enhanced measurements: beating the standard quantum limit", Science **306**, 1330–1336 (2004).

[156]S. L. Braunstein and P. van Loock, "Quantum information with continuous variables", Rev. Mod. Phys. **77**, 513–577 (2005).

[157]E. S. Polzik, J. Carri, and H. J. Kimble, "Spectroscopy with squeezed light", Phys. Rev. Lett. **68**, 3020–3023 (1992).

[158]P. H. S. Ribeiro, C. Schwob, A. Matre, and C. Fabre, "Sub-shot-noise high-sensitivity spectroscopy with optical parametric oscillator twin beams", Optics Letters **22**, 1893 (1997).

[159]N. Treps, U. Andersen, B. Buchler, P. K. Lam, A. Ma{\textasciicircum}tre, H.-A. Bachor, and C. Fabre, "Surpassing the standard quantum limit for optical imaging using nonclassical multimode light", Phys. Rev. Lett. **88**, 203601 (2002).

[160]M. A. Taylor, J. Janousek, V. Daria, J. Knittel, B. Hage, H.-A. Bachor, and W. P. Bowen, "Subdiffraction-limited quantum imaging within a living cell", Phys. Rev. X **4**, 011017 (2014).

[161]T. L. S. Collaboration, "A gravitational wave observatory operating beyond the quantum shot-noise limit", Nat Phys **7**, 962–965 (2011).

[162]J Aasi, J Abadie, B. Abbott, R Abbott, T. Abbott, M. Abernathy, C Adams, T Adams, P Addesso, R. Adhikari, et al., "Enhanced sensitivity of the LIGO gravitational wave detector by using squeezed states of light", Nature Photonics **7**, 613–619 (2013).

[163]K. Goda, O. Miyakawa, E. E. Mikhailov, S. Saraf, R. Adhikari, K. McKenzie, R. Ward, S. Vass, A. J. Weinstein, and N. Mavalvala, "A quantum-enhanced prototype gravitational-wave detector", Nature Physics **4**, 472–476 (2008).

[164]A. M. Marino and P. D. Lett, "Absolute calibration of photodiodes with bright twin beams", Journal of Modern Optics **58**, 328–336 (2011).

[165]F. Wolfgramm, A. Cer, F. A. Beduini, A. Predojevi, M. Koschorreck, and M. W. Mitchell, "Squeezed-light optical magnetometry", Phys. Rev. Lett. **105**, 053601 (2010).

[166]N. Otterstrom, R. C. Pooser, and B. J. Lawrie, "Nonlinear optical magnetometry with accessible in situ optical squeezing", Optics Letters **39**, 6533 (2014).

[167]M. A. Taylor, J. Janousek, V. Daria, J. Knittel, B. Hage, H.-A. Bachor, and W. P. Bowen, "Biological measurement beyond the quantum limit", Nat Photon **7**, 229–233 (2013).

[168]M. A. Taylor and W. P. Bowen, "Quantum metrology and its application in biology", arXiv:1409.0950 [quant-ph] (2014).

[169]R. C. Pooser and B. Lawrie, "Ultrasensitive measurement of microcantilever displacement below the shot-noise limit", Optica **2**, 393 (2015).

[170]A. A. Berni, T. Gehring, B. M. Nielsen, V. Hndchen, M. G. A. Paris, and U. L. Andersen, "Ab initio quantum-enhanced optical phase estimation using real-time feedback control", Nat Photon **9**, 577–581 (2015).

[171]V. Giovannetti, S. Lloyd, and L. Maccone, "Quantum-enhanced positioning and clock synchronization", Nature **412**, 417–419 (2001).

[172]N. C. Menicucci, "Fault-tolerant measurement-based quantum computing with continuous-variable cluster states", Phys. Rev. Lett. **112**, 120504 (2014).

[173]Z. Y. Ou, S. F. Pereira, H. J. Kimble, and K. C. Peng, "Realization of the einstein-podolsky-rosen paradox for continuous variables", Phys. Rev. Lett. **68**, 3663–3666 (1992).

[174]C. Silberhorn, P. K. Lam, O. Wei, F. Knig, N. Korolkova, and G. Leuchs, "Generation of continuous variable einstein-podolsky-rosen entanglement via the kerr nonlinearity in an optical fiber", Phys. Rev. Lett. **86**, 4267–4270 (2001).

[175]M. D. Reid, P. D. Drummond, W. P. Bowen, E. G. Cavalcanti, P. K. Lam, H. A. Bachor, U. L. Andersen, and G. Leuchs, "Colloquium: the einstein-podolsky-rosen paradox: from concepts to applications", Rev. Mod. Phys. **81**, 1727–1751 (2009).

[176]A. S. Villar, K. N. Cassemiro, K. Dechoum, A. Z. Khoury, M. Martinelli, and P. Nussenzveig, "Entanglement in the above-threshold optical parametric oscillator", J. Opt. Soc. Am. B **24**, 249–256 (2007).

[177]A. S. Villar, L. S. Cruz, K. N. Cassemiro, M. Martinelli, and P. Nussenzveig, "Generation of bright two-color continuous variable entanglement", Phys. Rev. Lett. **95**, 243603 (2005).

[178]J. Jing, J. Zhang, Y. Yan, F. Zhao, C. Xie, and K. Peng, "Experimental demonstration of tripartite entanglement and controlled dense coding for continuous variables", Phys. Rev. Lett. **90**, 167903 (2003).

[179]J. Jing, S. Feng, R. Bloomer, and O. Pfister, "Experimental continuous-variable entanglement from a phase-difference-locked optical parametric oscillator", Phys. Rev. A **74**, 041804 (2006).

[180]X. Su, A. Tan, X. Jia, Q. Pan, C. Xie, and K. Peng, "Experimental demonstration of quantum entanglement between frequency-nondegenerate optical twin beams", Optics Letters **31**, 1133 (2006).

[181]K.-i. Yoshino, T. Aoki, and A. Furusawa, "Generation of continuous-wave broadband entangled beams using periodically poled lithium niobate waveguides", Applied Physics Letters **90**, 041111 (2007).

[182]K. N. Cassemiro and A. S. Villar, "Scalable continuous-variable entanglement of light beams produced by optical parametric oscillators", Phys. Rev. A **77**, 022311 (2008).

[183]T. Eberle, V. Hndchen, J. Duhme, T. Franz, R. F. Werner, and R. Schnabel, "Strong einstein-podolsky-rosen entanglement from a single squeezed light source", Physical Review A **83** (2011) 10.1103/PhysRevA.83.052329.

[184]A. Furusawa, J. L. Srensen, S. L. Braunstein, C. A. Fuchs, H. J. Kimble, and E. S. Polzik, "Unconditional quantum teleportation", Science **282**, 706–709 (1998).

[185]S. L. Braunstein and H. J. Kimble, "Teleportation of continuous quantum variables", Phys. Rev. Lett. **80**, 869–872 (1998).

[186]N. C. Menicucci, P. van Loock, M. Gu, C. Weedbrook, T. C. Ralph, and M. A. Nielsen, "Universal quantum computation with continuous-variable cluster states", Phys. Rev. Lett. **97**, 110501 (2006).

[187]S. T. Flammia, N. C. Menicucci, and O. Pfister, "The optical frequency comb as a one-way quantum computer", J. Phys. B: At. Mol. Opt. Phys. **42**, 114009 (2009).

[188]M. Gu, C. Weedbrook, N. C. Menicucci, T. C. Ralph, and P. van Loock, "Quantum computing with continuous-variable clusters", Phys. Rev. A **79**, 062318 (2009).

[189]S. Yokoyama, R. Ukai, S. C. Armstrong, C. Sornphiphatphong, T. Kaji, S. Suzuki, J.-i. Yoshikawa, H. Yonezawa, N. C. Menicucci, and A. Furusawa, "Ultra-large-scale continuous-variable cluster states multiplexed in the time domain", Nat Photon **7**, 982–986 (2013).

[190]J. Roslund, R. M. de Arajo, S. Jiang, C. Fabre, and N. Treps, "Wavelength-multiplexed quantum networks with ultrafast frequency combs", Nat Photon **8**, 109–112 (2014).

[191]O. Pinel, P. Jian, R. M. de Arajo, J. Feng, B. Chalopin, C. Fabre, and N. Treps, "Generation and characterization of multimode quantum frequency combs", Phys. Rev. Lett. **108**, 083601 (2012).

[192]M. Pysher, Y. Miwa, R. Shahrokhshahi, R. Bloomer, and O. Pfister, "Parallel generation of quadripartite cluster entanglement in the optical frequency comb", Phys. Rev. Lett. **107**, 030505 (2011).

[193]S. Clemmen, K. P. Huy, W. Bogaerts, R. G. Baets, P. Emplit, and S. Massar, "Continuous wave photon pair generation in silicon-on-insulator waveguides and ring resonators", Optics Express **17**, 16558 (2009).

[194]J. E. Sharping, K. F. Lee, M. A. Foster, A. C. Turner, B. S. Schmidt, M. Lipson, A. L. Gaeta, and P. Kumar, "Generation of correlated photons in nanoscale silicon waveguides", Optics Express **14**, 12388 (2006).

[195]T. Suhara, "Generation of quantum-entangled twin photons by waveguide nonlinear-optic devices", Laser & Photon. Rev. **3**, 370–393 (2009).

[196]R. Horn, P. Abolghasem, B. J. Bijlani, D. Kang, A. S. Helmy, and G. Weihs, "Monolithic source of photon pairs", Physical Review Letters **108**, 153605 (2012).

[197]F. Najafi, J. Mower, N. C. Harris, F. Bellei, A. Dane, C. Lee, X. Hu, P. Kharel, F. Marsili, S. Assefa, K. K. Berggren, and D. Englund, "On-chip detection of non-classical light by scalable integration of single-photon detectors", Nat Commun **6**, 5873 (2015).

[198]R. K. W. Lau, M. R. E. Lamont, Y. Okawachi, and A. L. Gaeta, "Effects of multiphoton absorption on parametric comb generation in silicon microresonators", Opt. Lett., OL **40**, 2778–2781 (2015).

[199]G.-L. Lan, P. K. Banerjee, and S. S. Mitra, "Raman scattering in optical fibers", J. Raman Spectrosc. **11**, 416–423 (1981).

[200]E. Ippen and R. Stolen, "Stimulated scattering in optical fibers", IEEE Journal of Quantum Electronics **8**, 549–549 (1972).

[201]G. E. Walrafen and J. Stone, "Raman spectral characterization of pure and doped fused silica optical fibers", Applied Spectroscopy **29**, 337–344 (1975).

[202]S. M. Spillane, T. J. Kippenberg, and K. J. Vahala, "Ultralow-threshold raman laser using a spherical dielectric microcavity", Nature **415**, 621–623 (2002).

[203]H. Lee, T. Chen, J. Li, K. Y. Yang, S. Jeon, O. Painter, and K. J. Vahala, "Chemically etched ultrahigh-q wedge-resonator on a silicon chip", Nat Photon **6**, 369–373 (2012).

[204]J. Li, H. Lee, T. Chen, and K. J. Vahala, "Low-pump-power, low-phase-noise, and microwave to millimeter-wave repetition rate operation in microcombs", Phys. Rev. Lett. **109**, 233901 (2012).

[205]P. Del'Haye, A. Coillet, T. Fortier, K. Beha, D. C. Cole, K. Y. Yang, H. Lee, K. J. Vahala, S. B. Papp, and S. A. Diddams, "Phase-coherent microwave-to-optical link with a self-referenced microcomb", Nat Photon **10**, 516–520 (2016).

[206]X. Yi, Q.-F. Yang, K. Y. Yang, M.-G. Suh, and K. Vahala, "Soliton frequency comb at microwave rates in a high-q silica microresonator", Optica **2**, 1078 (2015).

[207]A. C. Turner, C. Manolatou, B. S. Schmidt, M. Lipson, M. A. Foster, J. E. Sharping, and A. L. Gaeta, "Tailored anomalous group-velocity dispersion in silicon channel waveguides", Opt Express **14**, 4357–4362 (2006).

[208]J. S. Levy, A. Gondarenko, M. A. Foster, A. C. Turner-Foster, A. L. Gaeta, and M. Lipson, "CMOS-compatible multiple-wavelength oscillator for on-chip optical interconnects", Nat Photon **4**, 37–40 (2010).

[209]F. Castelli and P. Dotti, "Quantum noise reduction in non-degenerate four-wave-mixing oscillators", Optics Communications **113**, 237–248 (1994).

[210]S. Ast, M. Mehmet, and R. Schnabel, "High-bandwidth squeezed light at 1550 nm from a compact monolithic PPKTP cavity", Opt. Express **21**, 13572–13579 (2013).

[211]M. R. E. Lamont, Y. Okawachi, and A. L. Gaeta, "Route to stabilized ultrabroadband microresonator-based frequency combs", Optics Letters **38**, 3478 (2013).

[212]T. Herr, K. Hartinger, J. Riemensberger, C. Y. Wang, E. Gavartin, R. Holzwarth, M. L. Gorodetsky, and T. J. Kippenberg, "Universal formation dynamics and noise of kerr-frequency combs in microresonators", Nat Photon **6**, 480–487 (2012).

[213]V. R. Almeida, R. R. Panepucci, and M. Lipson, "Nanotaper for compact mode conversion", Opt. Lett. **28**, 1302–1304 (2003).

[214]A. S. Coelho, F. A. S. Barbosa, K. N. Cassemiro, A. S. Villar, M. Martinelli, and P. Nussenzveig, "Three-color entanglement", Science **326**, 823–826 (2009).

[215]C. J. McKinstrie and M. Karlsson, "Schmidt decompositions of parametric processes i: basic theory and simple examples", Optics Express **21**, 1374 (2013).

[216]N. V. Corzo, Q. Glorieux, A. M. Marino, J. B. Clark, R. T. Glasser, and P. D. Lett, "Rotation of the noise ellipse for squeezed vacuum light generated via four-wave mixing", Phys. Rev. A **88**, 043836 (2013).

[217]L.-M. Duan, G. Giedke, J. I. Cirac, and P. Zoller, "Inseparability criterion for continuous variable systems", Phys. Rev. Lett. **84**, 2722–2725 (2000).

[218]R. Simon, "Peres-horodecki separability criterion for continuous variable systems", Phys. Rev. Lett. **84**, 2726–2729 (2000).

[219]T. Barwicz, M. A. Popovic, P. T. Rakich, M. R. Watts, H. A. Haus, E. P. Ippen, and H. I. Smith, "Microring-resonator-based add-drop filters in SiN: fabrication and analysis", Optics Express **12**, 1437 (2004).

[220]A. Dutt, S. Miller, K. Luke, J. Cardenas, A. L. Gaeta, P. Nussenzveig, and M. Lipson, "Tunable squeezing using coupled ring resonators on a silicon nitride chip", Optics Letters **41**, 223 (2016).

[221]H. Yonezawa, D. Nakane, T. A. Wheatley, K. Iwasawa, S. Takeda, H. Arao, K. Ohki, K. Tsumura, D. W. Berry, T. C. Ralph, H. M. Wiseman, E. H. Huntington, and A. Furusawa, "Quantum-enhanced optical-phase tracking", Science **337**, 1514–1517 (2012).

[222]A. Ourjoumtsev, R. Tualle-Brouri, J. Laurat, and P. Grangier, "Generating optical schrdinger kittens for quantum information processing", Science **312**, 83–86 (2006).

[223]R. Schnabel, N. Mavalvala, D. E. McClelland, and P. K. Lam, "Quantum metrology for gravitational wave astronomy", Nature Communications **1**, 121 (2010).

[224]G. Y. Xiang, B. L. Higgins, D. W. Berry, H. M. Wiseman, and G. J. Pryde, "Entanglement-enhanced measurement of a completely unknown optical phase", Nat Photon **5**, 43–47 (2011).

[225]D. W. Berry, B. L. Higgins, S. D. Bartlett, M. W. Mitchell, G. J. Pryde, and H. M. Wiseman, "How to perform the most accurate possible phase measurements", Phys. Rev. A **80**, 052114 (2009).

[226]G. A. Durkin and J. P. Dowling, "Local and global distinguishability in quantum interferometry", Phys. Rev. Lett. **99**, 070801 (2007).

[227]B. L. Higgins, D. W. Berry, S. D. Bartlett, H. M. Wiseman, and G. J. Pryde, "Entanglement-free heisenberg-limited phase estimation", Nature **450**, 393–396 (2007).

[228]K. Wakui, H. Takahashi, A. Furusawa, and M. Sasaki, "Photon subtracted squeezed states generated with periodically poled KTiOPO_4", Optics Express **15**, 3568 (2007).

[229]A. Laghaout, J. S. Neergaard-Nielsen, I. Rigas, C. Kragh, A. Tipsmark, and U. L. Andersen, "Amplification of realistic schrodinger-cat-state-like states by homodyne heralding", Phys. Rev. A **87**, 043826 (2013).

[230]A. Ourjoumtsev, H. Jeong, R. Tualle-Brouri, and P. Grangier, "Generation of optical schrdinger cats from photon number states", Nature **448**, 784–786 (2007).

[231]H. Jeong, M. S. Kim, and J. Lee, "Quantum-information processing for a coherent superposition state via a mixedentangled coherent channel", Phys. Rev. A **64**, 052308 (2001).

[232]T. C. Ralph, A. Gilchrist, G. J. Milburn, W. J. Munro, and S. Glancy, "Quantum computation with optical coherent states", Phys. Rev. A **68**, 042319 (2003).

[233]M. Cai, O. Painter, and K. J. Vahala, "Observation of critical coupling in a fiber taper to a silica-microsphere whispering-gallery mode system", Phys. Rev. Lett. **85**, 74–77 (2000).

[234]J. U. Frst, D. V. Strekalov, D. Elser, A. Aiello, U. L. Andersen, C. Marquardt, and G. Leuchs, "Quantum light from a whispering-gallery-mode disk resonator", Phys. Rev. Lett. **106**, 113901 (2011).

[235]M. Frtsch, J. U. Frst, C. Wittmann, D. Strekalov, A. Aiello, M. V. Chekhova, C. Silberhorn, G. Leuchs, and C. Marquardt, "A versatile source of single photons for quantum information processing", Nat Commun **4**, 1818 (2013).

[236]S. Reynaud, C. Fabre, and E. Giacobino, "Quantum fluctuations in a two-mode parametric oscillator", Journal of the Optical Society of America B **4**, 1520 (1987).

[237]C. M. Savage and D. F. Walls, "Squeezing by parametric oscillation and intracavity four-wave mixing", Journal of the Optical Society of America B **4**, 1514 (1987).

[238]Y. K. Chembo, "Quantum correlations, entanglement, and squeezed states of light in kerr optical frequency combs", arXiv:1412.5700 [physics, physics:quant-ph] (2014).

[239]S. A. Miller, Y. Okawachi, S. Ramelow, K. Luke, A. Dutt, A. Farsi, A. L. Gaeta, and M. Lipson, "Tunable frequency combs based on dual microring resonators", Optics Express **23**, 21527 (2015).

[240]S. A. Miller, "Nonlinear silicon photonics: extending platforms, control, and applications", (2017) `http://doi.org/10.7298/X49G5JXH`.

[241]M. Davanco, J. R. Ong, A. B. Shehata, A. Tosi, I. Agha, S. Assefa, F. Xia, W. M. J. Green, S. Mookherjea, and K. Srinivasan, "Telecommunications-band heralded single photons from a silicon nanophotonic chip", Applied Physics Letters **100**, 261104 (2012).

[242]R. Kumar, J. R. Ong, J. Recchio, K. Srinivasan, and S. Mookherjea, "Spectrally multiplexed and tunable-wavelength photon pairs at 155 m from a silicon coupled-resonator optical waveguide", Optics Letters **38**, 2969 (2013).

[243]D. D. Smith, H. Chang, K. A. Fuller, A. T. Rosenberger, and R. W. Boyd, "Coupled-resonator-induced transparency", Phys. Rev. A **69**, 063804 (2004).

[244]A. B. Matsko, A. A. Savchenkov, D. Strekalov, V. S. Ilchenko, and L. Maleki, "Interference effects in lossy resonator chains", Journal of Modern Optics **51**, 2515–2522 (2004).

[245]C. M. Gentry, X. Zeng, and M. A. Popovic, "Tunable coupled-mode dispersion compensation and its application to on-chip resonant four-wave mixing", Opt. Lett. **39**, 5689–5692 (2014).

[246]M. T. Wade, X. Zeng, and M. A. Popovi, "Wavelength conversion in modulated coupled-resonator systems and their design via an equivalent linear filter representation", Optics Letters **40**, 107 (2015).

[247]X. Zeng and M. A. Popovic, "Design of triply-resonant microphotonic parametric oscillators based on kerr nonlinearity", Opt. Express **22**, 15837–15867 (2014).

[248]S. Ramelow, A. Farsi, S. Clemmen, J. S. Levy, A. R. Johnson, Y. Okawachi, M. R. E. Lamont, M. Lipson, and A. L. Gaeta, "Strong polarization mode coupling in microresonators", Optics Letters **39**, 5134 (2014).

[249]K. Numata, J. Camp, M. A. Krainak, and L. Stolpner, "Performance of planar-waveguide external cavity laser for precision measurements", Optics Express **18**, 22781 (2010).

[250]J. Cardenas, C. B. Poitras, K. Luke, L.-W. Luo, P. A. Morton, and M. Lipson, "High coupling efficiency etched facet tapers in silicon waveguides", IEEE Photonics Technology Letters **26**, 2380–2382 (2014).

[251]T. J. Kippenberg, S. M. Spillane, and K. J. Vahala, "Kerr-nonlinearity optical parametric oscillation in an ultrahigh- q toroid microcavity", Physical Review Letters **93**, 083904 (2004).

[252]H. Jung, K. Y. Fong, C. Xiong, and H. X. Tang, "Electrical tuning and switching of an optical frequency comb generated in aluminum nitride microring resonators", Opt. Lett. **39**, 84–87 (2014).

[253]Y. Okawachi, M. R. E. Lamont, K. Luke, D. O. Carvalho, M. Yu, M. Lipson, and A. L. Gaeta, "Bandwidth shaping of microresonator-based frequency combs via dispersion engineering", Optics Letters **39**, 3535 (2014).

[254]M. A. Foster, J. S. Levy, O. Kuzucu, K. Saha, M. Lipson, and A. L. Gaeta, "Silicon-based monolithic optical frequency comb source", Optics Express **19**, 14233 (2011).

[255]Y. Okawachi, K. Saha, J. S. Levy, Y. H. Wen, M. Lipson, and A. L. Gaeta, "Octave-spanning frequency comb generation in a silicon nitride chip", Optics Letters **36**, 3398 (2011).

[256]R. Raussendorf and H. J. Briegel, "A one-way quantum computer", Phys. Rev. Lett. **86**, 5188–5191 (2001).

[257]J. Zhang and S. L. Braunstein, "Continuous-variable gaussian analog of cluster states", Phys. Rev. A **73**, 032318 (2006).

[258]N. C. Menicucci, S. T. Flammia, and O. Pfister, "One-way quantum computing in the optical frequency comb", Phys. Rev. Lett. **101**, 130501 (2008).

[259]N. C. Menicucci, S. T. Flammia, H. Zaidi, and O. Pfister, "Ultracompact generation of continuous-variable cluster states", Phys. Rev. A **76**, 010302 (2007).

[260]S. T. Cundiff and J. Ye, "Colloquium : femtosecond optical frequency combs", Rev. Mod. Phys. **75**, 325–342 (2003).

[261]R. Medeiros de Arajo, J. Roslund, Y. Cai, G. Ferrini, C. Fabre, and N. Treps, "Full characterization of a highly multimode entangled state embedded in an optical frequency comb using pulse shaping", Phys. Rev. A **89**, 053828 (2014).

[262]M. Chen, N. C. Menicucci, and O. Pfister, "Experimental realization of multipartite entanglement of 60 modes of a quantum optical frequency comb", Phys. Rev. Lett. **112**, 120505 (2014).

[263]R. N. Alexander, P. Wang, N. Sridhar, M. Chen, O. Pfister, and N. C. Menicucci, "One-way quantum computing with arbitrarily large time-frequency continuous-variable cluster states from a single optical parametric oscillator", Phys. Rev. A **94**, 032327 (2016).

[264]K. Saha, Y. Okawachi, B. Shim, J. S. Levy, R. Salem, A. R. Johnson, M. A. Foster, M. R. E. Lamont, M. Lipson, and A. L. Gaeta, "Modelocking and femtosecond pulse generation in chip-based frequency combs", Optics Express **21**, 1335 (2013).

[265]T. Herr, V. Brasch, J. D. Jost, C. Y. Wang, N. M. Kondratiev, M. L. Gorodetsky, and T. J. Kippenberg, "Temporal solitons in optical microresonators", Nature Photonics **8**, 145–152 (2013).

[266]S. Coen, H. G. Randle, T. Sylvestre, and M. Erkintalo, "Modeling of octave-spanning kerr frequency combs using a generalized mean-field lugiatolefever model", Optics Letters **38**, 37 (2013).

[267]M. Erkintalo and S. Coen, "Coherence properties of kerr frequency combs", Optics Letters **39**, 283 (2014).

[268]L. S. Cruz, D. Felinto, J. Aguirre Gmez, M. Martinelli, P. Valente, A. Lezama, and P. Nussenzveig, "Laser-noise-induced correlations and anti-correlations in electromagnetically induced transparency", The European Physical Journal D **41**, 531–539 (2006).

[269]A. Villar, M. Martinelli, and P. Nussenzveig, "Testing the entanglement of intense beams produced by a non-degenerate optical parametric oscillator", Optics Communications **242**, 551–563 (2004).

[270]H. Kogelnik and T. Li, "Laser beams and resonators", Appl. Opt., AO **5**, 1550–1567 (1966).

[271]E. Hecht, *Optics*, 4th ed (Addison-Wesley, Reading, Mass, 2002), 698 pp.

[272]R. A. Boyd, J. L. Bliss, and K. G. Libbrecht, "Teaching physics with 670nm diode lasersexperiments with fabryperot cavities", American Journal of Physics **64**, 1109–1116 (1996).

[273]E. D. Black, "An introduction to pounddreverhall laser frequency stabilization", American Journal of Physics **69**, 79–87 (2001).

[274]E. D. Black, *Pdh.pdf*.

[275]R. Neuhaus and T. P. AG, *Diode laser locking and linewidth narrowing*.

[276]R. W. P. Drever, J. L. Hall, F. V. Kowalski, J. Hough, G. M. Ford, A. J. Munley, and H. Ward, "Laser phase and frequency stabilization using an optical resonator", Appl. Phys. B **31**, 97–105 (1983).

[277]O. Glckl, U. L. Andersen, and G. Leuchs, "Verifying continuous-variable entanglement of intense light pulses", Physical Review A **73** (2006) `10.1103/PhysRevA.73.012306`.

[278]A. S. Villar, "The conversion of phase to amplitude fluctuations of a light beam by an optical cavity", American Journal of Physics **76**, 922 (2008).

[279]P. Galatola, L. A. Lugiato, M. G. Porreca, P. Tombesi, and G. Leuchs, "System control by variation of the squeezing phase", Optics Communications **85**, 95–103 (1991).

[280]T. W. Hnsch, "Nobel lecture: passion for precision", Rev. Mod. Phys. **78**, 1297–1309 (2006).

[281]C.-B. Huang, Z. Jiang, D. Leaird, J. Caraquitena, and A. Weiner, "Spectral line-by-line shaping for optical and microwave arbitrary waveform generations", Laser & Photon. Rev. **2**, 227–248 (2008).

[282]T. M. Fortier, M. S. Kirchner, F. Quinlan, J. Taylor, J. C. Bergquist, T. Rosenband, N. Lemke, A. Ludlow, Y. Jiang, C. W. Oates, and S. A. Diddams, "Generation of ultrastable microwaves via optical frequency division", Nat Photon **5**, 425–429 (2011).

[283]J. L. Hall, "Nobel lecture: defining and measuring optical frequencies", Rev. Mod. Phys. **78**, 1279–1295 (2006).

[284]S. B. Papp, K. Beha, P. DelHaye, F. Quinlan, H. Lee, K. J. Vahala, and S. A. Diddams, "Microresonator frequency comb optical clock", Optica, OPTICA **1**, 10–14 (2014).

[285]P.-H. Wang, F. Ferdous, H. Miao, J. Wang, D. E. Leaird, K. Srinivasan, L. Chen, V. Aksyuk, and A. M. Weiner, "Observation of correlation between route to formation, coherence, noise, and communication performance of kerr combs", Optics Express **20**, 29284 (2012).

[286]J. Pfeifle, V. Brasch, M. Lauermann, Y. Yu, D. Wegner, T. Herr, K. Hartinger, P. Schindler, J. Li, D. Hillerkuss, R. Schmogrow, C. Weimann, R. Holzwarth, W. Freude, J. Leuthold, T. J. Kippenberg, and C. Koos, "Coherent terabit communications with microresonator kerr frequency combs", Nature Photonics **8**, 375–380 (2014).

[287]J. Pfeifle, A. Coillet, R. Henriet, K. Saleh, P. Schindler, C. Weimann, W. Freude, I. V. Balakireva, L. Larger, C. Koos, and Y. K. Chembo, "Optimally coherent kerr combs generated with crystalline whispering gallery mode resonators for ultrahigh capacity fiber communications", Physical Review Letters **114** (2015) 10.1103/PhysRevLett.114.093902.

[288]C.-H. Li, A. J. Benedick, P. Fendel, A. G. Glenday, F. X. Krtner, D. F. Phillips, D. Sasselov, A. Szentgyorgyi, and R. L. Walsworth, "A laser frequency comb

that enables radial velocity measurements with a precision of 1cms-1", Nature **452**, 610–612 (2008).

[289]T. Steinmetz, T. Wilken, C. Araujo-Hauck, R. Holzwarth, T. W. Hnsch, L. Pasquini, A. Manescau, S. D'Odorico, M. T. Murphy, T. Kentischer, W. Schmidt, and T. Udem, "Laser frequency combs for astronomical observations", Science **321**, 1335–1337 (2008).

[290]D. F. Phillips, A. G. Glenday, C.-H. Li, C. Cramer, G. Furesz, G. Chang, A. J. Benedick, L.-J. Chen, F. X. Krtner, S. Korzennik, D. Sasselov, A. Szentgyorgyi, and R. L. Walsworth, "Calibration of an astrophysical spectrograph below 1 m/s using a laser frequency comb", Optics Express **20**, 13711 (2012).

[291]G. G. Ycas, F. Quinlan, S. A. Diddams, S. Osterman, S. Mahadevan, S. Redman, R. Terrien, L. Ramsey, C. F. Bender, B. Botzer, and S. Sigurdsson, "Demonstration of on-sky calibration of astronomical spectra using a 25 GHz near-IR laser frequency comb", Optics Express **20**, 6631 (2012).

[292]M. Zajnulina, J. M. C. Boggio, M. Bhm, A. A. Rieznik, T. Fremberg, R. Haynes, and M. M. Roth, "Generation of optical frequency combs via four-wave mixing processes for low- and medium-resolution astronomy", Appl. Phys. B **120**, 171–184 (2015).

[293]S. A. Diddams, D. J. Jones, J. Ye, S. T. Cundiff, J. L. Hall, J. K. Ranka, R. S. Windeler, R. Holzwarth, T. Udem, and T. W. Hnsch, "Direct link between microwave and optical frequencies with a 300 THz femtosecond laser comb", Phys. Rev. Lett. **84**, 5102–5105 (2000).

[294]D. J. Jones, S. A. Diddams, J. K. Ranka, A. Stentz, R. S. Windeler, J. L. Hall, and S. T. Cundiff, "Carrier-envelope phase control of femtosecond mode-locked lasers and direct optical frequency synthesis", Science **288**, 635–639 (2000).

[295]S. A. Diddams, "The evolving optical frequency comb [invited]", Journal of the Optical Society of America B **27**, B51 (2010).

[296]I. H. Agha, Y. Okawachi, M. A. Foster, J. E. Sharping, and A. L. Gaeta, "Four-wave-mixing parametric oscillations in dispersion-compensated high-q silica microspheres", Phys. Rev. A **76**, 043837 (2007).

[297]A. A. Savchenkov, A. B. Matsko, V. S. Ilchenko, I. Solomatine, D. Seidel, and L. Maleki, "Tunable optical frequency comb with a crystalline whispering gallery mode resonator", Phys. Rev. Lett. **101**, 093902 (2008).

[298]R. Henriet, G. Lin, A. Coillet, M. Jacquot, L. Furfaro, L. Larger, and Y. K. Chembo, "Kerr optical frequency comb generation in strontium fluoride whispering-gallery mode resonators with billion quality factor", Optics Letters **40**, 1567 (2015).

[299]C. Y. Wang, T. Herr, P. DelHaye, A. Schliesser, J. Hofer, R. Holzwarth, T. W. Hnsch, N. Picqu, and T. J. Kippenberg, "Mid-infrared optical frequency combs at 2.5 m based on crystalline microresonators", Nat Commun **4**, 1345 (2013).

[300]P. DelHaye, T. Herr, E. Gavartin, M. L. Gorodetsky, R. Holzwarth, and T. J. Kippenberg, "Octave spanning tunable frequency comb from a microresonator", Phys. Rev. Lett. **107**, 063901 (2011).

[301]S. Schiller, "Spectrometry with frequency combs", Optics Letters **27**, 766 (2002).

[302]F. Keilmann, C. Gohle, and R. Holzwarth, "Time-domain mid-infrared frequency-comb spectrometer", Optics Letters **29**, 1542 (2004).

[303]B. Bernhardt, A. Ozawa, P. Jacquet, M. Jacquey, Y. Kobayashi, T. Udem, R. Holzwarth, G. Guelachvili, T. W. Hnsch, and N. Picqu, "Cavity-enhanced dual-comb spectroscopy", Nat Photon **4**, 55–57 (2010).

[304]I. Coddington, W. C. Swann, and N. R. Newbury, "Coherent multiheterodyne spectroscopy using stabilized optical frequency combs", Phys. Rev. Lett. **100**, 013902 (2008).

[305]I. Coddington, W. C. Swann, and N. R. Newbury, "Coherent dual-comb spectroscopy at high signal-to-noise ratio", Phys. Rev. A **82**, 043817 (2010).

[306]I. Coddington, N. Newbury, and W. Swann, "Dual-comb spectroscopy", Optica **3**, 414 (2016).

[307]T. Ideguchi, A. Poisson, G. Guelachvili, N. Picqu, and T. W. Hnsch, "Adaptive real-time dual-comb spectroscopy", Nat Commun **5**, 3375 (2014).

[308]S. Mehravar, R. A. Norwood, N. Peyghambarian, and K. Kieu, "Real-time dual-comb spectroscopy with a free-running bidirectionally mode-locked fiber laser", Applied Physics Letters **108**, 231104 (2016).

[309]S. M. Link, A. Klenner, M. Mangold, C. A. Zaugg, M. Golling, B. W. Tilma, and U. Keller, "Dual-comb modelocked laser", Optics Express **23**, 5521 (2015).

[310]G. Villares, J. Wolf, D. Kazakov, M. J. Sess, A. Hugi, M. Beck, and J. Faist, "On-chip dual-comb based on quantum cascade laser frequency combs", Applied Physics Letters **107**, 251104 (2015).

[311]M.-G. Suh, Q.-F. Yang, K. Y. Yang, X. Yi, and K. Vahala, "Microresonator soliton dual-comb spectroscopy", (2016).

[312]M. Yu, Y. Okawachi, A. G. Griffith, N. Picqu, M. Lipson, and A. L. Gaeta, "Silicon-chip-based mid-infrared dual-comb spectroscopy", arXiv preprint arXiv:1610.01121 (2016).

[313]C. Joshi, J. K. Jang, K. Luke, X. Ji, S. A. Miller, A. Klenner, Y. Okawachi, M. Lipson, and A. L. Gaeta, "Thermally controlled comb generation and soliton modelocking in microresonators", Optics Letters **41**, 2565 (2016).

[314]T. Carmon, L. Yang, and K. J. Vahala, "Dynamical thermal behavior and thermal self-stability of microcavities", Optics Express **12**, 4742 (2004).

[315]F. Leo, S. Coen, P. Kockaert, S.-P. Gorza, P. Emplit, and M. Haelterman, "Temporal cavity solitons in one-dimensional kerr media as bits in an all-optical buffer", Nat Photon **4**, 471–476 (2010).

[316]V. Brasch, M. Geiselmann, M. H. P. Pfeiffer, and T. J. Kippenberg, "Bringing short-lived dissipative kerr soliton states in microresonators into a steady state", arXiv:1607.07477 [physics] (2016).

[317]G. Millot, S. Pitois, M. Yan, T. Hovhannisyan, A. Bendahmane, T. W. Hnsch, and N. Picqu, "Frequency-agile dual-comb spectroscopy", Nat Photon **10**, 27–30 (2016).

[318]Ming Yan, Pei-Ling Luo, Kana Iwakuni, Guy Millot, Theodor W. Hnsch, and Nathalie Picqu, "Midinfrared dualcomb spectroscopy with electrooptic modulators", arXiv preprint arXiv:1608.08013 (2015).

[319]V. Durn, S. Tainta, and V. Torres-Company, "Ultrafast electrooptic dual-comb interferometry", Optics Express **23**, 30557 (2015).

[320]V. Durn, P. A. Andrekson, and V. Torres-Company, "Electro-optic dual-comb interferometry over 40 nm bandwidth", Opt. Lett. **41**, 4190–4193 (2016).

[321]D. A. Long, A. J. Fleisher, K. O. Douglass, S. E. Maxwell, K. Bielska, J. T. Hodges, and D. F. Plusquellic, "Multiheterodyne spectroscopy with optical frequency combs generated from a continuous-wave laser", Opt. Lett., OL **39**, 2688–2690 (2014).

[322]S. Coen and M. Erkintalo, "Universal scaling laws of kerr frequency combs", Optics Letters **38**, 1790 (2013).

[323]A. J. Fleisher, B. J. Bjork, T. Q. Bui, K. C. Cossel, M. Okumura, and J. Ye, "Mid-infrared time-resolved frequency comb spectroscopy of transient free radicals", The Journal of Physical Chemistry Letters **5**, 2241–2246 (2014).

[324]S. Ast, A. Samblowski, M. Mehmet, S. Steinlechner, T. Eberle, and R. Schnabel, "Continuous-wave nonclassical light with gigahertz squeezing bandwidth", Opt. Lett. **37**, 2367–2369 (2012).

[325]J. Lin, Y. Xu, J. Ni, M. Wang, Z. Fang, L. Qiao, W. Fang, and Y. Cheng, "Phase-matched second-harmonic generation in an on-chip ${\mathrm{l}\mathrm{i}\mathrm{NbO}}_{3}$ microresonator", Phys. Rev. Applied **6**, 014002 (2016).

[326]C. Wang, M. J. Burek, Z. Lin, H. A. Atikian, V. Venkataraman, I.-C. Huang, P. Stark, and M. Lonar, "Integrated high quality factor lithium niobate microdisk resonators", Opt. Express, OE **22**, 30924–30933 (2014).

[327]W. C. Jiang and Q. Lin, "Chip-scale cavity optomechanics in lithium niobate", Sci Rep **6** (2016) 10.1038/srep36920.

[328]C. Javerzac-Galy, K. Plekhanov, N. R. Bernier, L. D. Toth, A. K. Feofanov, and T. J. Kippenberg, "On-chip microwave-to-optical quantum coherent converter based on a superconducting resonator coupled to an electro-optic microresonator", Phys. Rev. A **94**, 053815 (2016).

[329]P. W. Anderson, "More is different", Science **177**, 393–396 (1972).

[330]T. Ideguchi, T. Nakamura, Y. Kobayashi, and K. Goda, "A bidirectional dual-comb ring laser for simple and robust dual-comb spectroscopy", arXiv:1512.00979 [physics] (2015).

[331]L. Del Bino, J. M. Silver, S. L. Stebbings, and P. Del'Haye, "Symmetry breaking of counter-propagating light in a nonlinear resonator", Sci Rep **7** (2017) 10.1038/srep43142.

[332]Purnawirman, J. Sun, T. N. Adam, G. Leake, D. Coolbaugh, J. D. B. Bradley, E. S. Hosseini, and M. R. Watts, "C- and l-band erbium-doped waveguide lasers with wafer-scale silicon nitride cavities", Opt. Lett., OL **38**, 1760–1762 (2013).

[333]E. S. Hosseini, Purnawirman, J. D. B. Bradley, J. Sun, G. Leake, T. N. Adam, D. D. Coolbaugh, and M. R. Watts, "CMOS-compatible 75 mW erbium-doped distributed feedback laser", Opt. Lett., OL **39**, 3106–3109 (2014).

[334]H. Park, A. W. Fang, S. Kodama, and J. E. Bowers, "Hybrid silicon evanescent laser fabricated with a silicon waveguide and III-v offset quantum wells", Opt. Express, OE **13**, 9460–9464 (2005).

[335]M. Pollnau, "Rare-earth-ion-doped channel waveguide lasers on silicon", IEEE Journal of Selected Topics in Quantum Electronics **21**, 414–425 (2015).

[336]T. Minamikawa, Y. D. Hsieh, K. Shibuya, Y. Kaneoka, S. Okubo, H. Inaba, Y. Mizutani, T. Yasui, and T. Iwata, "Dual-optical-comb spectroscopic ellipsometry", in 2016 conference on lasers and electro-optics (CLEO) (June 2016), pp. 1–2.

[337]R. P. Feynman, "Simulating physics with computers", Int J Theor Phys **21**, 467–488 (1982).

[338]S. A. Miller, M. Yu, X. Ji, A. G. Griffith, J. Cardenas, A. L. Gaeta, and M. Lipson, "Low-loss silicon platform for broadband mid-infrared photonics", arXiv:1703.03517 [physics] (2017).